Coarse-Graining Electronic Behavior in Condensed Matter Systems: From Electrons to Continuum Elasticity

by

Darren Eric Segall

Submitted to the Department of Physics
in partial fulfillment of the requirements for the degree of
Doctor of Philosophy in Physics
at the
MASSACHUSETTS INSTITUTE OF TECHNOLOGY
September 2002

Author ....Darren Segall..
Department of Physics
August 6, 2002

Certified by...
Tomás A. Arias
Professor
Thesis Supervisor

Certified by...
John D. Joannopoulos
Professor
Thesis Supervisor

Accepted by ....Thomas J. Greytak..........................
Thomas J. Greytak
Professor, Associate Department Head for Education

Coarse-Graining Electronic Behavior in Condensed Matter Systems: From Electrons to Continuum Elasticity

by

Darren Eric Segall

Submitted to the Department of Physics
on August 6, 2002, in partial fulfillment of the
requirements for the degree of
Doctor of Philosophy in Physics

Abstract

In this thesis properties of various condensed matter systems are studied, whose dependency on electronic behavior is incorporated through coarse-grained interactions. Three specific systems are considered.

In the first system of study, high momentum, plane wave states of the electronic wave function are coarse-grained, while the low momentum states are fully resolved. Moreover, the coarse-graining procedure incorporates the response of the high momentum states to environmental changes and its couplings to changes in the low momentum states. Within density functional theory this allows the representation of the electronic wave function, when using a plane wave basis, to be computationally feasible without having to make the pseudopotential approximation. This coarse-graining procedure is beneficial for the study of high pressure systems, where the response of the core region is important. With this method we study a number of solid phases of boron and reveal a number of important structural and electronic properties on its high pressure and superconducting phase.

The second system of study focuses on a slightly coarser scale, where a theory for the elasticity of nanometer sized objects is developed. This theory provides a powerful way of understanding nanoscale elasticity in terms of local group contributions and acts as a bridge between the atomic and the continuum regimes. This theory properly describes elastic fluctuations on length scales on the order of the decay length of the force constant matrix; allowing for straightforward development of new relations between the bending and stretching properties of nanomechanical resonators, which prove to be much more accurate than the continuum-based relations currently employed in experimental analysis. This theory is then used to link features of the underlining electronic structure to the local elastic response in silicon nanoresonators, emphasizing the importance of electronic structure on the local and overall elastic response.

Our final system of study focuses on the longest length scales, the continuum. It is shown that the inclusion of electronic structure is crucial in the study of the role of dislocations on the macroscopic property of slip. This thesis explores the discrepancy between experimental data and theoretical calculations of the lattice resistance in bcc metals. This thesis presents results for the temperature dependence of the Peierls stress and the first *ab initio* calculation of the zero-temperature Peierls stress which employ periodic boundary conditions. The *ab initio* value for the Peierls stress is over five times larger than current extrapolations of experimental lattice resistance to zero-temperature. Although it is found that the common techniques for such extrapolation indeed tend to underestimate the zero-temperature limit, in this work it is shown that other mechanisms other than the simple Peierls mechanism are important in controlling the process of low temperature slip.

Thesis Supervisor: Tomás A. Arias
Title: Professor

Thesis Supervisor: John D. Joannopoulos
Title: Professor

Acknowledgments

There are many people to whom I wish to thank for providing me with emotional and intellectual support during my time as a graduate student. First I am thankful for my adviser, Professor Tomàs Arias, on many fronts. On the professional level he has been a great research adviser. Professor Arias has always made sure that I stayed focused on the important issues in my research, thereby forcing me to explore the significant scientific matters and not stray off on insignificant details. He has given me the freedom to explore and develop my own ideas, while through great insight, continually pointing me in the right directions. He has work laboriously on improving my writing, which has not only improved the quality of my writing but my train of thought. Along with writing he has also helped me to improve my presentations, specifically, on how to present ideas to others in a clear fashion. On a more personal note, I am grateful to have had an adviser who was always been willing to make my graduate life the best situation possible for me and my family. After accepting his position at Cornell Professor Arias has always made sure that the situation for his students at MIT remained the best it could be. On my trips to Cornell he has always been a gracious host. More importantly, he had helped me continue my graduate studies in California by getting me situated at Cal-Tech for the past two years, while stilling maintaining to be an active adviser. This situation has proved to be extremely beneficial to me and my family.

Next, I am indebted to Professor Bill Goddard for his hospitality during my stay at Cal-Tech. Professor Goddard had allowed me to freely work with his group, provided me with many of the benefits that his group members received and always made sure my needs were met. I thoroughly enjoyed interacting with him and his group and I am thankful to him for providing me with such an opportunity.

I am also very grateful for the many office mates and colleges with whom I have encountered over the past years. To my original office mates at MIT: Sohrab Ismail-Beigi, Torkel Engeness and Gabor Csyani, and our neighboring colleague Dicle Yesilleten, I thank them for providing me with support in research, graduate life and, when need be, an opposing view to my political positions, particularly Torkel with whom I have had many enjoyable disagreements. I'm thankful to Joel Moore for our many enjoyable discussion, particularly for our mildly heated sports debates over lunch. I thank Vivek Sujan for providing me with much needed comic relief, along with interesting talks over many matters of life.

Next, I thank the group members at Cornell: Daniel Freedman, Hande Ustunel and Ivan Daykov, for providing me with great hospitality during my long stays at Cornell. Specifically to Dan for many interesting discussions, whether it be physics, computers or politics.

I thank Alejandro Strachan, Guofeng Wang, Rick Muller and Tahir Cagin, at Cal-Tech, for the hospitality and support they have provided me during my stay there.

I thank my sister-in-law Chris Segall, who has looked over a number of my manuscript and provided me with many grammatical corrections and stylistic advise.

Finally, and most importantly I am thankful for my wife Jessica and daughter Erika, whom have always supported me and have been understanding of the demanding work required from me. Most importantly they have opened many, previously unsee-able, new doors of life to me, which has allowed me to grow in ways I could not have imagined. In turn this has made my work much more enjoyable and less stressful by allowing me to see the more significant things in life.

Contents

1 Introduction **19**

2 New *ab initio* approach for high pressure systems with application to a new high-pressure phase for boron: perturbative momentum-space potentials. **23**

2.1 Methods 25

2.2 Perturbative Derivation 27

2.2.1 Derivation for fixed potentials 27

2.2.2 Connections with Löwdin Perturbation Theory 31

2.3 Applications To Conjugate Gradient Techniques 33

2.3.1 Application to Traditional Conjugate Gradient Techniques . . 33

2.3.2 Application in the Analytic Continued Approach 37

2.3.3 Computational details 39

2.3.4 Application to the Coulomb Potential 44

2.4 Application to High Pressure Boron 47

2.4.1 Convergence 49

2.4.2 Results 51

2.5 Conclusions 55

3 Elasticity of nanometer-sized objects **57**

3.1 Overview 59

3.2 Nanowire rigidities 61

3.3 Method of long waves 62

3.4 Failure of straightforward approach in nanowires 64
3.5 Method of long waves in nanowires 66
3.6 Transferability 69
3.7 Extension from flexion 72
3.8 Correlation between local atomic moduli and electronic structure . . 74
3.9 Conclusions 78

4 Accurate calculations of the Peierls stress in small periodic cells 79
4.1 Reference Calculations 81
4.2 Periodic Boundary Conditions 85
4.3 Corrections 87
4.4 Accurate and Efficient Peierls Stress Calculation 90
  4.4.1 Benefit of fixed lattice vectors 90
  4.4.2 Extraction of elastic constants 92
  4.4.3 Second Peierls stress: $P2$ 94
4.5 Conclusion 94

5 *Ab initio* and finite-temperature molecular dynamics studies of lattice resistance in tantalum 97
5.1 Boundary Conditions 100
  5.1.1 Cylindrical Boundary Conditions 100
  5.1.2 Greens Function Boundary Conditions 101
  5.1.3 Periodic Boundary Conditions 104
5.2 Dependence of the Peierls stress on orientation and temperature . . . 105
  5.2.1 Orientation dependence of the zero-temperature Peierls stress of the $\langle 111 \rangle$ screw dislocation 106
  5.2.2 Temperature dependence of the Peierls stress of the $\langle 111 \rangle$ screw dislocation 108
5.3 Accurate Peierls Stress Calculations in small periodic cells 111
  5.3.1 Calculation of Peierls stress within periodic boundary conditions 112

5.3.2 Demonstration 115
5.4 Density functional results and discussion 116
5.4.1 Computational Details 116
5.4.2 Energy landscapes 117
5.4.3 Verification of cell size 118
5.4.4 Results for the Peierls Stress 119
5.5 Conclusion 122

A Application to Kleinman-Bylander pseudopotentials 123

B Use of continuous symmetries to produce local moduli 127

C Failure of straightforward approches to predict flexion 129

List of Figures

2-1 Flow chart for application to traditional conjugate gradient techniques. 35

2-2 Energy error versus iteration number for the new method, within the conjugate gradient framework for simple cubic hydrogen when using the Coulomb potential. 36

2-3 Energy error versus iteration number for the new method, within the conjugate gradient framework for fcc carbon when using a nonlocal pseudopotential. 36

2-4 Energy convergence versus iteration for simple cubic hydrogen when the overlap matrix is updated self-consistently, but its variational derivative is not taken into account. 42

2-5 Energy convergence versus iteration for fcc carbon when the overlap matrix is updated self-consistently, but its variational derivative is not taken into account. 42

2-6 Energy per atom as a function of cutoff energy for fcc boron, when using the Coulomb potential in the traditional plane-wave approach. The squares correspond $V_1 = 3.83$ Å^3 and the circles correspond to $V_2 = 3.5$ Å^3. 45

2-7 Energy difference as a function of cutoff for fcc boron, when using the traditional plane-wave approach. The volumes per atom are $V_1 =$ 3.83 Å^3 and $V_2 = 3.5$ Å^3. 46

2-8 Energy convergence versus P-space cutoff, using the new method, when $E_c^Q = 7000$ Ryd. The squares correspond to $V_1 = 3.83$ Å^3, the circles correspond to $V_2 = 3.5$ Å^3 and the diamonds correspond to the transferability prediction, Equation (2.19). The horizontal lines correspond to the energy calculated using the traditional approach at a cutoff energy of 7000 Ryd. 46

2-9 Energy difference in the new approach as a function of the P-space cutoff. 47

2-10 Energy per atom versus volume per atom for the fcc (circles), bct (stars) and α-12 (diamonds) structures. Energy cutoff for the P-space is 1200 Ryd and for the Q-space 7000 Ryd. The curves are fitted to Equation (2.30). 50

2-11 Energy per atom versus volume per atom. The results from new method using the cutoffs E_c^P=200 Ryd and E_c^Q=1200 Ryd are displayed as circles (fcc), stars (bct) and diamonds (α-12). The results from new method using the cutoffs E_c^P=1200 Ryd and E_c^Q=7000 Ryd are displayed as lines by fitting the data to Equation (2.30): fcc (dashed), bct (dotted), α-12 (solid). 51

2-12 Energy per atom versus volume per atom. The results from using the traditional approach with cutoff E=200 Ryd are displayed as circles (fcc), stars (bct) and diamonds (α-12). The results from new method using the cutoffs E_c^P=1200 Ryd and E_c^Q=7000 Ryd are displayed as lines by fitting the data to Equation (2.30): fcc (dashed), bct (dotted), α-12 (solid). 52

2-13 Energy per atom versus volume per atom, for the fcc (circles), bct (stars), α-12 (diamond), α-orthorhombic (left facing triangles) and β-orthorhombic (right facing triangles) structures. The results are from the new method using the cutoffs E_c^P=200 Ryd and E_c^Q=1200 Ryd. 53

2-14 Density of states for the valence electrons for the α-orthorhombic boron structure. The straight line corresponds to the chemical potential at $kT = 0.001H$. 54

2-15 Density of states for the valence electrons for the β-orthorhombic boron structure. The straight line corresponds to the chemical potential at $kT = 0.001H$. 55

3-1 Atomic structure of silicon nanowires with an approximate cross-sectional diameter of 1.5 nm. The wires are viewed along the longitudinal axis: $c(2 \times 2)$ structure (left), 2×1 structure (right). 65

3-2 Predictions of atomic moduli e_α for $c(2 \times 2)$ nanowires of varying diameter: (a) straightforward theory (Eq. (3.9)) and (b) new theory (Eq. (3.11)). The insets denote the approximate diameters of the wires. The value of the atomic modulus (Eq. (3.9) or Eq. (3.11)) is along the ordinate and radial distance of the atom from the center line is along the abscissa. 66

3-3 Fractional error as a function of inverse diameter $1/D$ in predicting (a) flexural rigidity from extensional properties (δF_{at}, Eq. (3.14) and δF_{tc}, Eq.(3.16)) and (b) extensional rigidity from flexural properties (δE_{at}, Eq. (3.20) and δE_{tc}, Eq. (3.21)). Note, for convenience, the abscissa is labeled by D and not $1/D$. 71

3-4 $c(2 \times 2)$ wire, with cross-section $\approx$ 2.4nm. Results are from the tight-binding model described in the text. Left: atomic moduli color coded from small to large: blue-green-yellow-red. Right: valence electronic density projected (integrated along the wire axis) onto the cross-section color coded from low to high: blue-green-yellow-red. White dots in the right figure indicate the location of atom cores. Note the correlation of large atomic moduli with large charge density along the surface. . . 76

3-5 2×1 wire, with cross-section $\approx$ 2.4nm: same conventions as Figure 3-4. 76

4-1 Peierls stress calculation within cylindrical boundary conditions: atoms whose distance from the center is less than $R1$ are relaxed under interatomic potential forces, while those in the region between $R1$ and $R2$ are held fixed to the anisotropic elasticity theory solution. 82

4-2 Differential displacement (DD) maps of a [111] screw dislocation at increasing stress computed within cylindrical boundary conditions: **a)** zero applied stress, **b)** initial jump along $(1\bar{1}0)$ at a stress ≥ 0.74 Gpa ($P1$), **c)** second jump, along $(2\bar{1}\bar{1})$ at a stress ≥ 0.91 GPa ($P2$), **d)** subsequent jump along $(2\bar{1}\bar{1})$, **e)** orientation of $\{110\}$ and $\{112\}$ planes. 83

4-3 Convergence of P1 and P2 as a function of $1/R1$, for cylinders ranging from $R1 = 30\AA$ to $R1 = 120\AA$. 84

4-4 Dislocation displacement (DD) map of a quadrupole dislocation array within a 270 atom cell with periodic boundary conditions. The cell may be reduced to 135 atoms with appropriate choice of lattice vectors. 86

4-5 Convergence of P1 calculated within periodic boundary conditions using unrelaxed lattice vectors and bulk elastic constants: Peierls stress calculated using Eq. 4.1 (squares), limit exacted from Figure 4-3 (solid line with width indicating numerical uncertainty). Uncertainties in the periodic calculations are smaller than the square symbols. 87

4-6 Convergence of P1 calculated within periodic boundary conditions: using relaxed lattice vectors and quadrupolar elastic constants (diamonds), using unrelaxed lattice vectors and quadrupolar elastic constants (circles), using unrelaxed lattice vectors, pure shear and elastic constants extracted during the calculation (triangles), asymptotic result extracted from cylindrical boundary conditions (horizontal line). Error bars associated with quadrupolar array are generally smaller than the associated icons. 89

4-7 The first nearest neighbors cannot generate any elastic force on the center dislocation, since they are equally spaced. From the core asymmetry there can be a core-core force in only in the $[1\bar{1}0]$. Note that these symmetry arguments works for higher order neighbors too. . . . 91

4-8 Energy of a $42\AA \times 42\AA \times 2.9\AA$ cell (270 atoms) plotted as a function of applied pure shear strain ϵ_{xz}: direct calculations (squares), quadratic fit (curve). 93

4-9 Convergence of P2 calculated within periodic boundary conditions: using unrelaxed lattice vectors and bulk elastic constants (squares), using relaxed lattice vectors and quadrupolar elastic constants (diamonds), using unrelaxed lattice vectors and quadrupolar elastic constants (circles), using unrelaxed lattice vectors, pure shear and elastic constants extracted during the calculation (triangles), asymptotic result extracted from cylindrical boundary conditions (horizontal line). 95

5-1 Force on the atoms, along the $\langle 111 \rangle$, due to the presence of a domain boundary. The forces are plotted as a function of distance from the center of the unit cell. The domain boundary is generated such that the nearest neighbor distance is always within 95% of the bulk ($\alpha = 1/4$). 104

5-2 Temperature dependence of the Peierls stress along various directions: the $\langle 112 \rangle$, twinning and anti-twinning directions. The fits are done for the high temperature data using Equation (5.1). The temperature is in Kelvin, and the stress in MegaPascals. 109

5-3 Quadrupolar unit cell of size 42Å× 41Å: relative displacements of neighboring columns of atoms (arrows), dislocation centers (plus signs). 111

5-4 Energy versus strain of vanadium in a quadrupolar cell of size 42Å× 20Å. Diamonds denote the energy calculated at various strains. The line is a quadratic fit up to the Peierls stress. 116

5-5 Energy landscape along a reaction coordinate when going from the easy core to the hard core configurations in tantalum and molybdenum: density functional theory (squares in upper panels), MGPT (curves in lower panels). *Ab initio* results for molybdenum are from Reference [42], and the MGPT tantalum results are from Reference [65]. . 118

5-6 Easy core structure for tantalum calculated within density functional theory. This cell of size 21Å× 40 Ågives very similar results to the cell of size 11.5Å× 23Å, used in Reference [42]. The diamond in the figure represents the center of the dislocation. 119

5-7 Energy versus strain for tantalum in a quadrupolar cell of size 11.5Å× 23Å, calculated within density functional theory. Squares denote the calculate energy at various strains. The line is a quadratic fit to the first six data points. The points with strain above 0.045 have not been fully converged. The graph indicates that the points with strain above 0.05 (stress = 1.7GPa) will be at a stress above the Peierls stress. . . 120

5-8 Differential displacement map at a stress of 1.3 GPa. The cell has converged to within the tolerance defined in the text. The diamond in the figure is the location of the center of the dislocation, under no stress. The center of the dislocation, at this applied stress, has not moved. 121

5-9 Differential displacement map at a stress of 3.0 GPa. The cell has *not* converged to within the tolerance defined in the text. This figure shows a split core, where a majority of the dislocation has moved to a new triad along a [110] direction. 121

List of Tables

2.1 The error in calculating the energy per atom for simple cubic hydrogen and fcc carbon. The first column shows the error in energy when using the traditional approach. The next column shows the error in energy when using the new approach. The final column shows the transferability prediction of the new approach, Equation (2.19). . . . 37

3.1 Comparison of errors between the traditional continuum theory and the atomic moduli description when predicting flexural response through Eqs (3.15) and (3.13) (first and second columns, respectively) and when inferring extensional response from flexural response through Eqs. (3.22) and (3.18) (third and fourth columns, respectively). . . . 77

5.1 Peierls stress for the $\langle 111 \rangle$ screw dislocation in tantalum in the twinning, $\langle 112 \rangle$ and anti-twinning directions; the last column shows the ratio between anti-twinning and twinning Peierls stresses. MGPT results from Yang et al [113]. 107

5.2 Magnitude of percentage error in calculating the Peierls stress in periodic supercells of two different sizes from empirical potentials for vanadium and tantalum. 116

Chapter 1

Introduction

Proper description of physical phenomena occurring over multiple length scales is a highly active field of research in condensed matter systems [73, 74, 87]. In such problems, fluctuations occurring over the shortest relevant length scales have important effects on physical phenomena occurring over the largest relevant length scales. When solving such problems difficulties occur as proper theoretical description of the shortest scales are, in general, either mathematically or computationally too demanding to properly describe physical phenomena occurring over the largest length scales. It is therefore crucial to extract the relevant physical effects imposed on the largest length scale phenomena by the smallest scale processes in a computationally and mathematically efficient manner. The crux of this thesis is to develop coarse-graining procedures to properly account for the electronic behavior in a number of condensed matter systems.

In Chapter 2 I develop a method, through the use of perturbation theory, which allows for a substantial reduction in the size of the plane wave basis used within density-functional theory. In this method, the high momentum plane waves states of the electronic wave function are coarse-grained within the system of study. An effective Hamiltonian is generated for this system which acts on the low momentum states. Moreover, this coarse-graining procedure allows for the recovery of the high momentum states to first order within perturbation theory, and, therefore, the response of such states can be incorporated into the computation. It is shown in Section 2.3 that accurate predictions for the error in calculating the energy, due to coarse-graining, can be made in any environment. Therefore, accurate predictions for the transferability of this method can be made in any system. Moreover, this method is incorporated into the conjugate gradient technique and it is therefore computationally efficient.

This procedure allows for the study of systems with a plane wave basis without having to make the pseudopotential approximation and is therefore ideal for high pressure systems. In such systems, the number of plane wave states needed to describe the core region is dramatically reduced while properly accounting for the cores response. In Section 2.4 this method is applied to the study of high pressure phases of boron. It is found that boron undergoes a phase transition from the icosahedral family to the α-orthorhombic structure, both of which are semiconducting. The α-orthorhombic structure has lower energy than traditional mono-atomic structures, which supports the assertion that the metallic, and hence superconducting, phase for boron is much more complicated than a simple mono-atomic crystal. Moreover, we conclude this chapter with the argument that the β-orthorhombic structure could be a candidate for the superconducting phase of boron.

The revolution in nanoscale technology has opened a wonderful opportunity for theoretical physics, as such systems lay at a cross-over between continuum physics and atomic physics. In Chapter 3 a theory of the elasticity of nanometer sized objects is presented. This theory coarse-grains ionic and electronic interactions into well-defined local moduli. Such moduli are able to describe elastic fluctuations over scales on the order of the decay length of the force constant matrix and, therefore, can describe nanoscale elasticity more accurately than current continuum theories. In Sections 3.6 and 3.7 specific examples are presented regarding the benefit of using this approach over continuum approaches. New relations between the bending and extensional properties for nanowires are presented which are much more accurate than continuum theories currently employed in experimental analysis. In Section 3.8 this theory is finally used to demonstrate correlations between the underlying electronic structure and the local elastic response.

The final system of study is the effects of electronic structure on the physics of mechanical slip. More specifically the importance of including electronic structure in the calculation of the Peierls stress in bcc tantalum will be addressed, the stress needed to move an infinite, straight dislocation. For bcc metals the extrapolated experimental value for the Peierls stress is at least a factor of two less [100, 25] than the values calculated from empirical potentials. This discrepancy has generally been attributed to the empirical nature of such potentials, which completely coarse-grains away electronic properties into interatomic potentials. However, other phenomena may also contribute to this discrepancy, as measuring the effects of a single isolated dislocation on the process of slip is a daunting experimental task. Therefore, to help resolve the discrepancy between theoretical and experimental Peierls stresses, the thesis provides the first *ab initio* predictions for the Peierls stress in a cell compliant with the system's electronic behavior. The effects of electronic structure are incorporated through the use of density-functional theory.

Prior to calculating the Peierls stress, the computational demands imposed by density-functional theory must be addressed. These costs limits the size of the unit cells (order ≈ 100 atoms for transition metals) which can be used and the range of phase space that can be explored in order to calculate the Peierls stress. In such small cells the effects imposed by the boundary conditions become extremely important. It remains unclear if these effects can properly be taken into account, in order to extract the stress needed to move an isolated dislocation in an infinite bulk medium. Moreover, if such boundary effects can be accounted, it remains unclear if the range of phase space needed to be explored in order to account for such effects will make the density-functional theory calculation infeasible. In Chapter 4 it is shown how to properly account for the boundary effects in an efficient manner which minimizes the search through phase space and allows a density-functional theory calculation possible.

In Chapter 5 the density-functional theory results are reported. It is shown that inclusion of the electronic structure in the mechanism of slip is indeed very important for bcc metals. The calculated value for the Peierls stress is a factor of $\approx$ six *larger* than extrapolations of experimental data. This discrepancy is much larger than any effects which could be attributed to the use of either our relatively small unit cell or the local density approximation made to density-functional theory. One must therefore consider the possibility of other factors to explain the discrepancy between theoretical and experimental predictions for the Peierls stress.

To explore possible effects leading to this discrepancy, we study the extrapolation of experimental data to determine the zero-temperature Peierls stress. Such extrapolations generally employ fits from mesoscopic or thermodynamics/kinetic models. However, it has not been established that such models can accurately describe the lowest temperature regime correctly. Using molecular dynamics simulations, within an empirical potential framework, finite-temperature values for the Peierls stress are calculated. Moreover, using finite-temperature results and current fitting models, it is shown that extrapolation of finite-temperature data leads to an underestimation of the zero-temperature Peierls stress. This underestimation may contribute to the discrepancy between the experimental extrapolated results and the density-functional theory calculation.

Chapter 2

New *ab initio* approach for high pressure systems with application to a new high-pressure phase for boron: perturbative momentum-space potentials.

Experimental techniques are now able to probe condensed matter systems at higher and higher pressures through the use of diamond-anvil cells or dynamical shock methods [3, 27]. At these newly attainable pressures, structural and electronic phase transitions can occur, opening the door to exploration for new physical phenomena.

Such systems offer an exciting avenue for first principle calculations, as their predictions can not only follow but also sometimes lead results from new experimental techniques [67, 68, 91, 30, 34, 101, 58, 27]. When applying traditional first principle calculations to such systems, care must be taken, as most basis sets take advantage of the distinction between the core regions and valence regions which is prominent at ambient conditions. However, when studying systems over a wide range of pressures, this distinction vanishes, and both regions need to be treated on an equal footing.

The following section discusses some problems that can occur when applying some of the most popular basis sets to high pressure systems.

To overcome the above potential pitfalls and to allow for accurate description of both the core and valence regions while keeping the mathematical stability and systematic convergence of the plane-wave basis, we have developed a method based on perturbation theory. This method can be used for direct all-electron calculations, dramatically reduces the size of the plane-wave basis while properly accounting for all higher momentum states, accounts accurately for the core electrons and their interaction with the valence region, and automatically generates pseudopotentials which change with the environment thereby enhancing transferability. Moreover, the effect of pseudizing in the crystal can be quantified; hence, accurate predictions for transferability can be made in *any* environment. Finally, the method can be implemented into current state of the art minimization techniques, such as the conjugate gradient method, and is therefore computationally efficient.

As an application, we study high pressure phases of boron. Boron crystallizes into many complex structures, which are governed by the regular icosahedron [23, 1]. Boron is semiconducting at ambient conditions, turns metallic under pressure ($\approx$ 170 GPa [27]) and superconducting above 160 GPa [27]. Theoretically, Mailhiot and coworkers [58] were the first to apply density-functional techniques to the study of the phases of Boron at high pressures. To date, however, such studies have been limited to a modest selection of phases and were based on traditional techniques which artificially separate the physics in the core and valence regions. In this chapter, we apply our new, unbiased technique to a wider range of phases and find a new phase, the α-orthorhombic structure, to be lower in energy at high pressure than any phase reported previously and to have important potential implications for the observed semiconductor-metallic phase transition associated with the superconductivity.

We proceed as follows: Section 2.1 describes the various methods that can be used to study systems under high pressure, specifically, the pros and cons of each method. Then our method is developed and tested in Sections 2.2 and 2.3. Finally, we will apply our approach to study the high pressure phases of boron in Section 2.4.

2.1 Methods

Within current state of the art electronic structure calculations, various approaches can be taken, mainly differentiated by the choice in basis set. Each set has its own benefits and disadvantages. Some of the most common basis sets are the plane-waves [45], Gaussian [48], linearized methods [86, 2], and wavelets [7]. We will now go over the various basis sets and focus on problems that may occur when each is applied to high pressure systems.

The Gaussian basis set expands the wave functions in terms of linear combinations of Gaussians designed to represent the atomic orbitals well. Such a basis set has the advantageous property of expanding the wave functions in a small number of computationally efficient basis functions. There are, however, some drawbacks. Notably, such a basis set cannot be improved systematically. This does not tend to be a practical problem for normal systems; however, such a problem can manifest itself for a system studied at various volumes, as the basis set will span a different percentage of real space for systems whose volume differ appreciably. Because it is unclear of how to convergence such a basis set systematically, it is unknown whether standard Gaussian basis sets will perform well at high-pressures, particularly because such bases are biased toward orbitals constructed at ambient conditions. It is thus unclear if such a bias can hamper calculations at high pressures, where unknown phenomena may occur.

Linearized methods generally fall under one of two methods: the Linear Muffin Tin Orbital (LMTO) [2] method or the Linearized Augmented Plane-Wave (LAPW) [86] method. Of these two, the LAPW is more accurate and we will therefore concentrate on this approach. When studying systems under high pressure, the most notable problem that can occur with the LAPW method is the treatment of the core electrons. At high pressures, certain core electrons need to be promoted and treated as valence electrons, and care must be taken with this method when promoting such electrons. Two widely used approaches to promote such electrons are the multiple window approach [86] and the localized orbital approach [86]. Both of these approaches could be particularly problematic for high pressure systems, particularly for first row elements. The multiple window method is not guaranteed to give a good solution [86], as different basis sets are used to expand the core and valence electrons. In the localized orbital approach, this problem is resolved by using one energy window. However, problems may exist, as there are very large energy separations between the valence bands and the core bands, particularly for first row elements.

The plane-wave approach, when used with the pure Coulomb potential, has the advantageous property that convergence of the energy can be systematically improved in a stable and controllable framework. Moreover, such a basis is unbiased and can therefore represent core and valence regions on an equal footing. However, such an approach has only been used for the simplest systems, such as hydrogen [10, 66, 11] and lithium [11] as it requires a huge number of plane-waves to properly account for the singular Coulomb potential and the exclusion principle. Therefore such an approach is not practical beyond the simplest systems.

The pseudopotential approach had been developed to circumvent the above difficulties with plane waves bases [33, 50, 74]. However, pseudopotentials are poorly suited for studying high pressure systems because, although some key properties are known [33, 95, 32], the transferability of pseudopotentials is not systematically understood, particularly when the pseudized regions occupy a large percentage of the available volume as they do at high densities. More fundamentally, apart from nonlinear core corrections in the exchange-correlation potential [55], pseudopotentials completely ignore the core region, which have been shown to play a vital role for high pressure systems [67, 68].

One of the most successful techniques, which keeps the benefits of the pseudopotential approach and can allow for core electrons and can recover details of the true wave function in the core region, is the Projected Augmented Wave (PAW) [13] method. This method has been used to study Lithium and Sodium [67, 68] under high pressure. Such a method is quite elegant; however, it must be constructed from a referenced atomic state. Moreover, the construction of such a potential still requires a real space cutoff. In order to effectively study high pressure systems, such a cutoff should be made quite small, so that the pseudized regions do not overlap. The approach then looses many of its computational benefits.

The final type of basis set of which we are aware in the study of solid state systems are wavelet bases [7]. Such bases have the attractive property of using multi-resolution analysis to provide the necessary resolution in each region of space in a systematic and mathematically stable manner and thereby efficiently handle valence and core electrons exactly. However, such a basis set has just come to the fore and has not yet been adopted by many groups.

We now describe a technique which has the advantage of using a plane-wave basis without pseudopotentials. This method has the added benefit of greatly reducing the size of the plane-wave basis set by generating the important high momentum states through perturbation theory. Below, we show that a properly constructed perturbation expansion can be quite accurate in this context. Finally, we show that this method can easily be implemented in current conjugate gradient techniques and therefore can be used with highly optimized minimization techniques.

2.2 Perturbative Derivation

In the next two sections, the method will be derived. To gain insight into this method, it will first be derived for the simple case of directly diagonalizing the single-particle Hamiltonian. Then, connections will be made to previous approaches [56]. In Section 2.3, the procedure will be implemented into the conjugate gradient framework, so that optimized calculations can be performed. Technical details will be discussed in Section 2.3.3. For simplicity in the formal developments below, we sample the Brillouin zone at the Gamma point. Adding in k-point dependence is straightforward.

2.2.1 Derivation for fixed potentials

Standard electronic structure calculations seek for the minimum of an energy functional $E[\{C\}]$ as a function of a set of basis function coefficients $\{C\}$ subject to an orthonormality constraint. The variational derivative of this energy functional and constraint then lead to the standard eigenvalue problem

$$HC = \epsilon C, \tag{2.1}$$

where H is the single-particle Hamiltonian (fixed and not updated self-consistently for the discussion in this section), C is an eigenvector and ϵ is the corresponding eigenvalue. Note that we here assume that the basis set is orthonormal as our objective here is to work with plane waves.

Separating the coefficients into two groups, those describing behavior in the low spatial frequency space P as C^P and those describing behavior in the high spatial frequency space Q as C^Q, also separates the couplings which H describes into four groups, couplings from low-frequency to low-frequency H^{PP}, from low- to high- frequency H^{QP}, from high to low H^{PQ} and from high to high H^{QQ}. The above equation then decomposes simply into

$$\begin{aligned} H^{PP}C^P + H^{PQ}C^Q &= \epsilon C^P & (2.2) \\ H^{QP}C^P + H^{QQ}C^Q &= \epsilon C^Q. & (2.3) \end{aligned}$$

Solving for the Q-space components of the eigenfunction in terms of the P-space components leads to

$$C^Q = -\frac{1}{H^{QQ} - \epsilon} H^{QP} C^P, \tag{2.4}$$

where the fraction means the inverse of an operator.

A standard technique [28, 56, 54] is to substitute Equation (2.4) into Equation (2.2) in order to generate an effective eigenvalue equation for the P-space,

$$(H^{PP} + H^{PQ} \frac{1}{\epsilon - H^{QQ}} H^{QP}) C^P = \epsilon C^P. \tag{2.5}$$

This equation reduces the problem to the P-space only. If standard diagonalization techniques are used, this reduces the time to diagonalize the Hamiltonian by a factor of $(\frac{N^P}{N^P+N^Q})^3$, where N^α is the number of basis functions in the α-space. However, it is well known that such a decomposition does not necessarily simplify the problem at hand, particularly because inversion of a matrix is computationally intensive and care must be taken in order to achieve self-consistency in the eigenvalue. We now describe an efficient way to go beyond the standard approach to address each of these issues in turn.

In a plane-wave basis, the inversion of $\epsilon - H^{QQ}$ can be approximated accurately and simply in a way which will save considerable computational effort, especially when used in conjunction with conjugate gradient techniques. Specifically, because the Q-space contains the high momentum plane-wave states, the kinetic energy dominates H^{QQ}, which we may then approximate to be the kinetic energy operator H_o^{QQ}, whose α, β component is

$$H^{QQ}_{o,\alpha\beta} = \frac{1}{2}\vec{Q}^2_\alpha \delta_{\alpha,\beta}. \tag{2.6}$$

Here $\delta_{\alpha,\beta}$ is the Kronecker delta and $\vec{Q}$ is a reciprocal lattice vector, and atomic units have been assumed.

In principle, the eigenvalues appearing in the left side of Equation (2.5) must be calculated self-consistently, but this leads to difficulties. Each eigenstate sought then sees a different Hamiltonian and orthonormality is lost. Alternately, in practice one employs on the left-hand side a constant, approximate ϵ which one hopes to be appropriate for all desired eigenvalues. For us, neither approach is satisfactory. To circumvent these difficulties, we linearize C^Q in terms of the eigenvalue

$$C^Q = -\frac{1}{H_o^{QQ}}(1 + \frac{\epsilon}{H_o^{QQ}})H^{QP}C^P + \mathcal{O}(\frac{\epsilon}{H_o^{QQ}})^2. \tag{2.7}$$

Note that in a plane-wave basis such an expansion will converge quickly, as the cutoff in the P-space is, in general, much larger than the eigenvalues of interest.

Substituting Equation (2.7), to linear order in ϵ, into Equation (2.2), gives an effective generalized eigenvalue equation,

$$(H^{PP} + H^{eff})C^P = \epsilon O C^P. \tag{2.8}$$

Here

$$H^{eff} = -H^{PQ}\frac{1}{H_o^{QQ}}H^{QP} \tag{2.9}$$

is the effective single-particle Hamiltonian and

$$\mathcal{O} = 1 + H^{PQ}\frac{1}{H_o^{QQ}}\frac{1}{H_o^{QQ}}H^{QP} \tag{2.10}$$

is a positive-definite overlap matrix. This equation will generate errors of order $(\epsilon/E_c^P)^2$ in the eigenvalue, where E_c^P is the cutoff energy for the P-space. We below, we show that this truncation error proves to be a good measure of the error in the energy per atom. Thus, our method provides for accurate *a priori* predictions for transferability errors.

In addition to computing the eigenvalue spectrum, we often require access to the eigenstates, particularly for density functional theory calculations which require self-consistent solution of the electronic states within a potential dependent upon those states. Calculation of the self-consistent potential requires not only the P-space components C^P from (2.8) but also the Q-space components. The most direct choice for generating the C^Q is to use Equation (2.7); however, we wish to eventually apply this technique to the conjugate gradient method and defining C^Q as in Equation (2.7), no longer preserves orthonormality for the full eigenvector set $\{C\}$ and post-reorthonormalization can make the conjugate gradient procedure unstable.

To avoid these difficulties, we note that the solutions to the generalize eigenvalue problem (2.8) automatically satisfy

$$\begin{aligned} \delta_{ij} &= C_i^{P\dagger}\mathcal{O}C_j^P \\ &= C_i^{P\dagger}\left(1 + H^{PQ}\frac{1}{H_o^{QQ}}\frac{1}{H_o^{QQ}}H^{QP}\right)C_j^P \end{aligned}$$

where the subscripts indicate the coefficients for individual states i and j and we have substituted the definition (2.10). Regrouping terms, we find that identically

$$\delta_{ij} = C_i^{P\dagger}C_j^P + \left(-\frac{1}{H_o^{QQ}}H^{PQ}C_j^P\right)^\dagger \left(-\frac{1}{H_o^{QQ}}H^{PQ}C_j^P\right),$$

so that the set of complete states $\{C\}$ will be exactly orthonormal provided we make the identification,

$$C^Q \equiv -\frac{1}{H_o^{QQ}} H^{QP} C^P, \tag{2.11}$$

which is nothing other than (2.7) truncated at zeroth order. We thus conclude that to avoid issues of orthonormality to allow simple implementation of conjugate gradient techniques, one *must* construct C^Q at this order. Accordingly, we employ (2.11) as the construction for C^Q throughout the reminder of this chapter.

2.2.2 Connections with Löwdin Perturbation Theory

To carry out full density-functional calculations based upon the results from the previous section, one in principle first would solve (2.8) using direct diagonalization techniques to find C^P and then construct C^Q from (2.11). Next, from the wave functions, one would update the charge density, Hartree and exchange-correlation potentials, recompute H^{PP}, H^{eff} and $\mathcal{O}$. Finally, one would iterate this procedure to self-consistency. As this approach is quite similar to the Löwdin perturbation theory [56] which was used in the mid 1980's by a number of groups [99, 114] with regard to electronic structure calculations, this section briefly reviews the Löwdin approach as described in Reference [99] and discuss the major differences between that approach and ours. The following section, Section , shows how conjugate gradient techniques may be applied directly to our approach but not to Löwdin perturbation theory.

Löwdin perturbation theory also decomposes behavior into high and low momentum plane-wave states. This approach also solves an eigenvalue problem $U^{PP}C^P = \epsilon C^P$ for a renormalized Hamiltonian U^{PP} similar to that of Equation (2.5),

$$U^{PP} = H^{PP} + H^{PQ} \frac{1}{\epsilon - H_o^{QQ}} H^{QP}, \tag{2.12}$$

Self-consistency is reached by calculating the charge density either with C^P alone, or with both C^P and C^Q, with as

$$C^Q = \frac{1}{\epsilon - H_o^{QQ}} U^{QP} C^P. \tag{2.13}$$

Here U^{QP} is similar to U^{PP}, except that the first index is in the Q-space. For the reasons discussed above in Section 2.2.1, if C^Q is employed, then the wave functions must be re-orthonormalized.

In practice [99], the value employed for ϵ in Equation (2.12) depends upon the physics under exploration. Thus, prior to the calculation, the shape of the band structure should be approximately known and should have a relatively narrow band-width, requiring great care for the study of systems under unusual physics conditions such as extremely high pressures. Moreover, the approximation of ϵ by $\tilde{\epsilon}$ is always a first order error in the solution to the eigenvalue. This can simply be seen by Taylor expanding Equations (2.12) and (2.13) in a similar fashion as Equations (2.7) and (2.8). If $\tilde{\epsilon}$ is close to ϵ, then this error is small as is the next order. However, if there is a large discrepancy between ϵ and $\tilde{\epsilon}$, then these errors are *manifestly* first order. This is particularly troublesome for calculations including core electrons where the core states energies have large separations from the valence states. We thus expect Löwdin perturbation to be useful primarily only within a pseudopotential framework. In our approach, by contrast, *all* band energies are treating on an equal footing to second order. This is because Equation (2.8) includes all terms through first order by shifting some terms to the right-hand side to form the generalized eigenvalue problem.

The great advantage of Löwdin perturbation theory for its time is that it reduces the time for standard diagonalization from $(N^P + N^Q)^3$ to $(N^P)^3$. However, in the mid 1980's standard diagonalization techniques were dropped in lieu of much more efficient Car-Parrinello [17, 71] and conjugate gradient [96, 71, 9] techniques, which, being based on minimization, require the the eigenvalue equations to represent the variational derivative of some energy functional. It is not clear that the Hamiltonian used within Löwdin perturbation theory is a good approximation to the variational derivative of an energy functional. What particularly complicates this is the dependence of the Hamiltonian on the eigenvalue and that the unfolding of the wave vector into the Q-space does not preserve orthonormality. Therefore, it is unclear how one would employ Löwdin perturbation theory in conjunction with such optimized minimization techniques. The next section demonstrates that, in contrast, our approach represents a very good approximation to the variational derivative of an energy functional and, because it preserves orthonormality, can be used directly with optimized minimization techniques.

2.3 Applications To Conjugate Gradient Techniques

We first discuss applicability to a traditional conjugate gradient techniques in Section 2.3.1 and generalize to the analytic continued approach [9, 40] in Section 2.3.2. Section 2.3.3 gives details of our computational implementation and Section 2.3.4 provides specific computational studies of the various approximations and the convergence of the approach.

2.3.1 Application to Traditional Conjugate Gradient Techniques

Again, we seek the minimum of an energy functional of the form $E[\{C\}]$ as a function of a set of wave function coefficients $\{C\}$. To formulate the separation into low- and high- spatial frequency components as a variational principle associated with an energy functional, we express the energy functional directly in terms of the $\{C^P\}$ and $\{C^Q\}$ *before* taking any variations, $E[\{C^P\},\{C^Q\}]$. We now seek the minimum of this functional subject to the orthonormalization condition

$$C_i^{P\dagger}\mathcal{O}C_j^P = \delta_{ij}. \tag{2.14}$$

Here $\mathcal{O}$ is an overlap matrix, which should give the correct overlap matrix at the minimum of the energy functional. Section 2.3.3 will describe the overlap matrix that we use in our calculations. Finally, the $\{C^Q\}$ are left *unconstrained.*

The sets $\{C^P\}$ and $\{C^Q\}$ are treated as independent variables. However, at each $\{C^P\}$ point, the functional is directly minimized with respect to the set $\{C^Q\}$. The gradients are

$$\frac{\partial E}{\partial C_i^{P\dagger}} \;=\; H^{PP}C_i^P + H^{PQ}C_i^Q - \epsilon O C_i^P \tag{2.15}$$

and

$$\frac{\partial E}{\partial C_i^{Q\dagger}} = 0 = \; H^{QP}C_i^P + H^{QQ}C_i^Q, \tag{2.16}$$

where the second term is set to zero, emphasizing that the energy functional is minimized with respect to $\{C^Q\}$ at each point $\{C^P\}$.

The flowchart in Figure 2-1 describes the minimization procedure within the traditional conjugate gradient framework. Given a point at $\{C^P\}$ and $\{C^Q\}$, calculate the energy. Next, calculate the gradient for the set $\{C^P\}$, Equation (2.15) or (2.18), and hold the set $\{C^Q\}$ fixed. Minimize the energy functional for the set $\{C^P\}$ only, along the conjugate direction $\{X^P\}$. After the functional is minimized along this particular direction, the functional is then minimized with respect to $\{C^Q\}$, Equation (2.16), by setting

$$C^Q = -\frac{1}{H_o^{QQ}} H^{QP} C^P. \tag{2.17}$$

Finally, this process iterates until the energy functional reaches its minimum.

In calculating C^Q, we have again approximated H^{QQ} by H_o^{QQ}, and therefore do not exactly minimize C^Q. Although the form for C^Q is not that which exactly minimizes our functional, we have found the approximation to be sufficiently close that the conjugate gradient technique is quite stable and efficient. Using such a form for C^Q, the gradient for C^P indeed becomes

$$\frac{\partial E}{\partial C_i^{P\dagger}} \;=\; H^{PP}C_i^P + H^{eff}C_i^P - \epsilon O C_i^P, \tag{2.18}$$

where H^{eff} is as defined in Equation (2.9). Thus, we find that, unlike the Löwdin per-

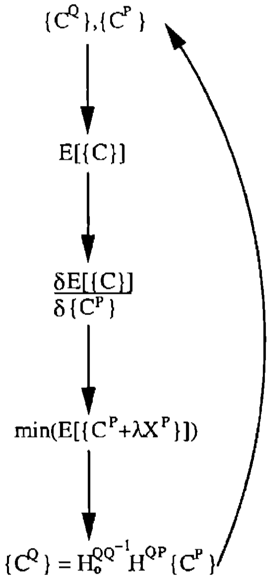

Figure 2-1: Flow chart for application to traditional conjugate gradient techniques.

turbation theory approach, the prescription in Section 2.2.1 represents a set of equations to represent to a very good approximation a variational principle and therefore to be amenable to solution with conjugate gradient methods.

To underscore the effectiveness of conjugate-gradient methods for use within our framework, Figures 2-2 and 2-3 show the iterative convergence of the total energy within the local density approximation (LDA) [72] to density-functional theory for cubic hydrogen and an eight atom cell of fcc carbon, respectively. The calculations use the preconditioner of Teter, Payne and Allen [96], cutoffs of $E_c^P = 8$ H and $E_c^Q = 16$ H for hydrogen and $E_c^P = 30$ H and $E_c^Q = 60$ H for carbon, and the overlap operator $\mathcal{O}$ from Section 2.3.3. The hydrogen calculation uses the pure Coulomb potential and an $8 \times 8 \times 8$ Monkhorst-Pack [64] sampling grid, and the carbon calculation uses the Goedecker, Teter and Hunter pseudopotential [31] with simple Γ-point sampling. Finally, the cubic lattice constants were 2.753 bohr and 6.746 bohr for sc hydrogen and fcc carbon, respectively.

It can be seen that the conjugate gradient technique is stable and that fluctuations occur only in the final stages when the error is $\Delta E/E_{min} \approx 10^{-10}$, well within acceptable convergence. These fluctuations are associated with the fact that H_o^{QQ} is

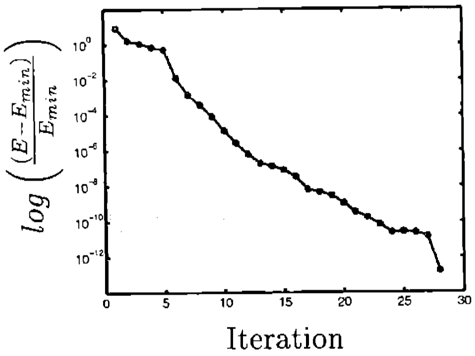

Figure 2-2: Energy error versus iteration number for the new method, within the conjugate gradient framework for simple cubic hydrogen when using the Coulomb potential.

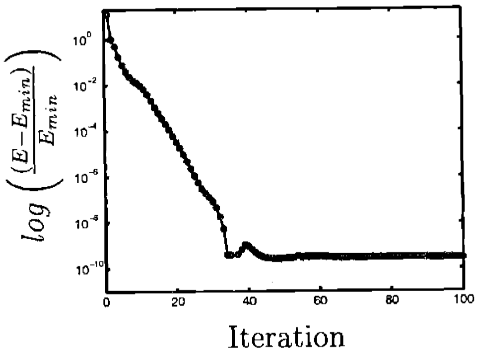

Figure 2-3: Energy error versus iteration number for the new method, within the conjugate gradient framework for fcc carbon when using a nonlocal pseudopotential.

used instead of H^{QQ}. In general, we have found that the stability of the conjugate gradient does not depend on the approximation for C^{Q}, but mainly depends on how and when we update C^{Q}. Table 2.1 compares the error in the energy per atom with the new approach, with cutoffs stated above, to that with the traditional approach, with cutoff $E_c^{trad} = E_c^{P}$. The fully converged results are considered to be that of the traditional approach with energy cutoff $E_c^{conv} = E_c^{Q}$. The results for the new procedure show a vast improvement.

As noted above, one of the advantages of our approach is that it allows for an *a priori* estimate of the transferability errors. We define this *transferability prediction*

	$\Delta E_{trad}(Ec = E_c^P)$	ΔE_{new}	$\Delta E_{new}^{predicted}$
Hydrogen (sc)	$9mH$	$1mH$	$2mH$
Carbon (fcc)	$16mH$	$0.3mH$	$0.2mH$

Table 2.1: The error in calculating the energy per atom for simple cubic hydrogen and fcc carbon. The first column shows the error in energy when using the traditional approach. The next column shows the error in energy when using the new approach. The final column shows the transferability prediction of the new approach, Equation (2.19).

as

$$\Delta E_{new}^{predict} = \sum_{states} \epsilon_{states}(\epsilon_{states}/E_c^P)^2, \tag{2.19}$$

where the sum is over occupied states. For the specific cases of the present two calculations, our prediction gives $\Delta E_{new}^{predict} \approx 0.5(0.5/8)^2 \approx 2mH$ for hydrogen and $\Delta E_{new}^{predict} \approx 2 \times 0.5(0.5/30)^2 \approx 0.2mH$ for carbon, where for simplicity we consider only the 2 s-states. These predictions also appear in Table 2.1. The predicted values are very similar to ΔE_{new}, demonstrating that this prediction, which may be applied in *any* environment, gives sensible estimates of the errors.

Sections 2.3.4 and 2.4 show that in practice the present method is particularly beneficial for all-electron calculations of first row elements, where the reduction in the cutoffs is much more dramatic than the cases presented here.

2.3.2 Application in the Analytic Continued Approach

Our procedure can be easily incorporated into the analytic continued conjugate gradient approach [9]. In such an approach, constrained variables, $\{C\}$, are not minimized, but unconstrained variables $\{Y\}$ are minimized. This approach allows for much better convergence, as all directions are allowed in the search space when minimizing the energy functional [9].

In the analytic continued approach, the sets $\{C\}$ and $\{Y\}$ are related by

$$\mathbf{C} = \mathbf{Y}u^{-\frac{1}{2}}V^{\dagger}, \tag{2.20}$$

where bold faced quantities refer to the expansion coefficients for all states gathered into matrices, each of whose columns represents a particular state. Here, V is a unitary transformation which allows for subspace rotations [9, 40] and u is the expectation value of $\mathbf{Y}$ with respect to the overlap matrix $\mathcal{O}$,

$$u = \mathbf{Y}^{\dagger}\mathcal{O}\mathbf{Y}. \tag{2.21}$$

Note that Equation (2.20) is constructed so that the $\mathbf{C}$ automatically satisfy the orthogonality constraint (2.14), as direct substitution verifies. This approach allows the total energy to be found by minimizing the energy $E[\mathbf{Y}]$ directly using standard, unconstrained conjugate-gradient techniques.

In our case, the gradient becomes

$$\begin{aligned}\frac{\partial E}{\partial \mathbf{Y}^{P\dagger}} &= (1 - \mathcal{O}\mathbf{C}^{P}\mathbf{C}^{P\dagger})(H^{PP} + H^{eff})\mathbf{C}^{P}FVU^{\frac{1}{2}} \\ &\quad + \mathcal{O}\mathbf{C}^{P}VQ(V^{\dagger}[\tilde{H}, F]V),\end{aligned} \tag{2.22}$$

where H^{eff} is as defined in Equation (2.9), F is a diagonal "filling" matrix composed of the state occupancies, $\mathcal{O}$ is the overlap matrix, defined similarly to Equation (2.10), and $Q()$ is the Q-operator [9, 40], defined by

$$\left(W^{\dagger}Q(A)W\right)_{nm} \equiv \frac{\left(W^{\dagger}AW\right)_{nm}}{\sqrt{\mu_n} + \sqrt{\mu_m}},$$

where W is the unitary, column order, eigenvector matrix for u and μ are the corresponding eigenvalues. In Equation (2.22), the Q-operator operates on the matrix $V^{\dagger}[\tilde{H}, F]V$, where $[\tilde{H}, F]$ is the commutator between the filling matrix F and the subspace Hamiltonian matrix,

$$\tilde{H} = \mathbf{C}^{P\dagger}(H^{PP} + H^{eff})\mathbf{C}^{P}.$$

Finally, the solution for $\mathbf{C}^{Q}$ becomes

$$\mathbf{C}^{Q} = -\frac{1}{H_o^{QQ}}H^{QP}\mathbf{C}^{P}. \tag{2.23}$$

We note that H^{eff} in Equation (2.22) acts as a pseudopotential generated directly from the crystal environment and not from a referenced atomic calculation which one must hope to be transferable. The overlap matrix $\mathcal{O}$ acts to preserve the correct orthonormalization for the P-space wave function. This overlap matrix is similar to those found in the Ultra-Soft Pseudopotentials (USSP) [98] and Projected Augmented Wave [13] methods. In those methods, the softening procedure is generated in a real space formalism, from a specific reference state, and depends on the choice of a cutoff in real space cutoff. In this work, the softening is done in a momentum space formalism without artificial core radii, making the procedure ideal for high-pressure studies where the loss of distinction between core and valence regions is precisely the physics of interest. As a final advantage of the present approach, Equation (2.19) gives a direct measure of transferability errors.

2.3.3 Computational details

We will now describe briefly efficient calculation of specific terms in our procedure. The text focuses on all-electron calculations as these are of interest in the present work. Appendix A discusses details for the use of this approach with hard but transferable Kleinman-Bylander pseudopotentials.

Form for overlap matrix

The overlap matrix has the form

$$\mathcal{O} = 1 + \left(H^{PQ}_{h,xc} + H^{PQ}_{ion}\right) \frac{1}{H^{QQ}_{o}} \frac{1}{H^{QQ}_{o}} \left(H^{QP}_{h,xc} + H^{QP}_{ion}\right), \tag{2.24}$$

where $\frac{1}{H^{QQ}_{o}}$ is the inverse of the kinetic energy, H_{ion} is the contribution from the local ionic potential and $H_{h,xc}$ is the contribution from the Hartree and exchange-correlation potentials, which depends on the density. There are a number of viable options for implementing $\mathcal{O}$. We have explored both the option of fixing $H_{h,xc}$, and thus $\mathcal{O}$ to some value and the option of updating it self-consistently.

The benefit of holding the overlap matrix fixed is that

$$\frac{\partial \mathcal{O}}{\partial \mathbf{C}^{P\dagger}} = 0, \tag{2.25}$$

so that Equation (2.15) is the exact variational derivative of the energy functional. Appendix A further shows that such a fixed operator makes efficient implementation of Kleinman-Bylander pseudopotentials possible. A clear choice for a fixed overlap matrix is to hold $H_{h,xc}$ in Equation (2.24) to that of the "free-atom" crystal, a crystal whose charge density is just the superposition of the charge densities from isolated atoms. In such a case, the overlap matrix becomes

$$\mathcal{O} \;=\; 1 + H^{cr-at,PQ}\frac{1}{H_o^{QQ}}\frac{1}{H_o^{QQ}}H^{cr-at,QP}, \tag{2.26}$$

where $H^{cr-at,PQ} = H_{h,xc}^{cr-at,PQ} + H_{ion}^{PQ}$ and $H_{h,xc}^{cr-at,PQ}$ is Hartree and exchange-correlation potential for the "free-atom" crystal. One possible cause for concern when using a fixed overlap matrix is that the orthonormalization is no longer exact (so that, for instance, the electronic charge will not be precisely conserved) because H^{QP} in Equation (2.23) will differ from its free-atom crystal value. However, we have found this to never affect the convergence of the calculations and to yield quite accurate results, as Figures 2-2 and 2-3 and Table 2.1 show.

Alternately, exact orthonormalization can be preserved when using a fixed overlap operator if one chooses to redefine $\mathbf{C}^Q$ as

$$\mathbf{C}^Q = -\frac{1}{H_o^{QQ}}H^{cr-at,QP}\mathbf{C}^P. \tag{2.27}$$

While this preserves orthonormality among the states, it does give a slightly different approximation to $\mathbf{C}^Q$, which causes a slight change in the H^{eff} which should be used in (2.8). We find, however, that ignoring this discrepancy makes no practical difference in the final results. With this alternate approach, the convergence is quite similar to those of Figures 2-2 and 2-3, and the energy per atom is within 1μ H, as compared to using Equation (2.23) for $\mathbf{C}^Q$. Another benefit of using the form Equation (2.27) comes when using non-local pseudopotentials, as this form is computationally more efficient. (See Appendix A for details.)

Finally, the H^{eff} which should be used with the construction in Equation (2.27) is

$$H^{eff} = -H^{PQ} \frac{1}{H_o^{QQ}} H^{cr-at,QP}. \tag{2.28}$$

Maintaining this consistency comes at the cost of introducing a slightly non-Hermitian Hamiltonian. Despite this, we again have not experienced any practical problems working with this form.

The second option for implementing the overlap matrix is to use the Hartree and exchange correlation potentials self-consistently. When doing so, the gradient of the total energy involves terms including the derivative of the overlap matrix. Unfortunately, we have yet to find a method for calculating these contributions to the gradient which does not require multiplication by matrices of size $N^P \times N^P$, a completely impractical feat for all but the most trivial of systems.

We have found somewhat to our surprise, however, that updating the overlap matrix self-consistently while completely ignoring these contributions to the gradient that, despite that with this approximated gradient, the gradient technique remains stable and maintains its good convergence, as Figures 2-4 and 2-5 show. In these calculations, $H_{h,xc}^{cr-at}$ was used only at the first iteration to initialize the calculation. After that, the overlap was updated self-consistently and the gradient was always calculated ignoring the aforementioned contributions from the changes in $\mathcal{O}$. The discontinuity in Figure 2-4 is a result of the fact that the error in the variational derivative is larger than before, as H_o^{QQ} and H^{cr-at} were only minor discrepancies. Perhaps a more stable approach would be to use $H_{h,xc}^{cr-at}$ for a number of iterations and then restart the conjugate gradient techniques using the self-consistent overlap matrix. In any event, we find the final energy per atom again to be within 1μ H of all of the approaches above.

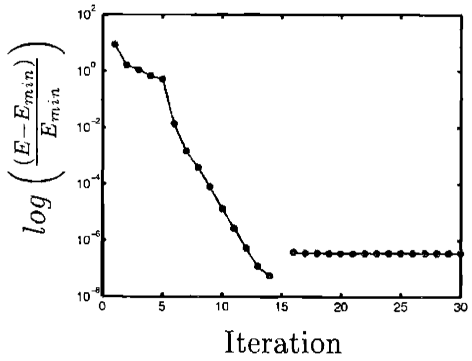

Figure 2-4: Energy convergence versus iteration for simple cubic hydrogen when the overlap matrix is updated self-consistently, but its variational derivative is not taken into account.

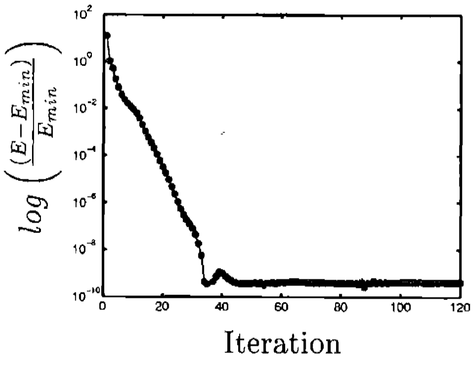

Figure 2-5: Energy convergence versus iteration for fcc carbon when the overlap matrix is updated self-consistently, but its variational derivative is not taken into account.

Numerical implementation

Specifying the mathematical form of the overlap matrix in one of the forms from the previous section and thus also the forms for $\mathbf{C}^Q$ and H^{eff} leaves the task of evaluating these and related quantities numerically. This section first discusses efficient methods for this evaluation and then describes how to build conjugate gradient minimization from the ability to perform these evaluations.

The term $\mathcal{O}\mathbf{Y}^P$ must be calculated for defining u, Equation (2.21), and in the gradient, Equation (2.22). The most efficient method for calculating this term is to perform four Fourier transforms per electronic wave function, always multiply terms in the space in which they are diagonal. We find it useful to keep this term in storage so as to only calculate it once in a conjugate gradient loop. Such storage is minimal, as will be seen.

To reduce the time spent in Fourier transforms, we make the approximation of using a slightly smaller Fourier transform grid than might normally be used. The gradient, the $\mathbf{C}^Q$, and the overlap matrix only involve momentum transfers of $P+Q$. Higher momentum transfers do not occur because H^{QQ} is approximated by H_o^{QQ}, which is diagonal. Accordingly, rather than Fourier grids of size $2Q$, when employ grids of size $P+Q$. We find that using the full Fourier transform grid decreases the energy minimally: for hydrogen and carbon doing so decreases the energy per atom by only 0.5μ H and 0.8μ H, respectively.

The reduction of the Fourier transform grid to size $P+Q$ from a size of $2Q$, which would be needed in a non-perturbative approach, saves significant storage in the ratio

$$\frac{FFT_{new}}{FFT_{full}} = \frac{1}{8}\left(1+3\left(\frac{E_P}{E_Q}\right)^{\frac{1}{2}}+3\left(\frac{E_P}{E_Q}\right)+\left(\frac{E_P}{E_Q}\right)^{\frac{3}{2}}\right). \tag{2.29}$$

In our boron calculation, this is a factor of nearly three, which can make the difference between being able to perform the calculation on a workstation or requiring parallel computing capability.

We find the following procedure to be very stable for performing conjugate gradient minimization. First, given $\mathbf{C}^P$ generate $\mathbf{C}^Q$ according to Equation (2.23) or (2.27).

Next, calculate the total energy and the gradient for $\mathbf{Y}^P$ at this point from Equation (2.22). Holding $\mathbf{C}^Q$ fixed, minimize $\mathbf{C}^P$ along the search direction, and generate a new $\mathbf{C}^P$, and iterate to convergence.

This procedure for solving for the P-space and generating the Q-space, when needed, is very beneficial for plane-wave calculations when using either the Coulomb potential or a very hard, yet highly transferable, pseudopotentials because, generally for such calculations the computational bottleneck is memory and this approach requires permanent storage only in the P-space. (The Q-space wave functions for a particular band can be generated only when needed.) Moreover, in terms of computational time, a savings of $1 + N_Q/N_P$ for all direct matrix multiplications occurs, and the P-space approach is therefore also more efficient in terms of computational time for systems with many bands.

2.3.4 Application to the Coulomb Potential

To demonstrate the benefits of our approach, this section presents all-electron calculations for fcc boron at two different volumes ($V_1 = 3.83$ Å^3 and $V_2 = 3.5$ Å^3), exploring covergence with energy cutoff, usage of memory and computational time, and our ability to predict transferability errors. We carry out all calculations within the local density approximation with ten special k-points in the reduced Brillouin zone and a Fermi surface integration temperature of $kT \approx 0.0037$ H.

Figure 2-6 shows the convergence of the energy as a function of cutoff for the direct plane wave approach. The data in the figure demonstrate that the traditional plane-wave approach converges quite slowly, requiring an energy cutoff of over 12000 Ryd to bring the total energy to within 0.1 eV per atom. However, as is well known, the higher-energy plane wave states provide convergence mostly to the inert region of the core near the nucleus and thus physically meaningful energy differences converge much more rapidly than the absolute total energy. As a more meaningful reference, Figure 2-7 shows the convergence of the energy difference between volume states V_1 and V_2 using the direct plane wave approach.

Figure 2-8 shows the convergence with P-space cutoff of the total energy when

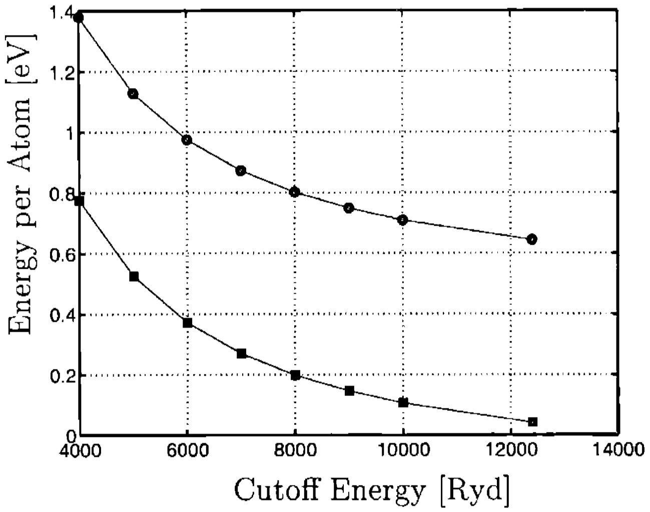

Figure 2-6: Energy per atom as a function of cutoff energy for fcc boron, when using the Coulomb potential in the traditional plane-wave approach. The squares correspond $V_1 = 3.83$ Å^3 and the circles correspond to $V_2 = 3.5$ Å^3.

using the perturbative approach with a Q-space cutoff of 7000 Ryd and employing $H^{cry-at}_{h,xc}$ for construction of $\mathcal{O}$. The figure shows show that there is almost no difference in the total energy predictions (circles and squares for the two volume states) when reducing the cutoff in the P-space to 3500 Ryd and that reducing the P-space cutoff down to 1000 Ryd gives just as accurate total energies as a 6000 Ryd cutoff in the traditional approach. The figure also shows that the transferability prediction based on the two core electrons (diamonds) gives the correct order of magnitude and is never off by more than a factor of three in this case.

Figure 2-9 shows the performance of the new approach in computing energy differences. Energy differences in the perturbative approach tend to fluctuate slightly and lack the monotonic behavior which the traditional approach exhibits due to loss of ability to describe physical changes in the high momentum states. Perturbation theory recovers these changes nearly perfectly and so the resulting error in energy difference is smaller and loses systematic behavior. From these results we conclude that a a cutoff in the P-space of 1200 Ryd and of 7000 Ryd in the Q-space is more than sufficient to predict accurate energy differences and to capture any unforeseen

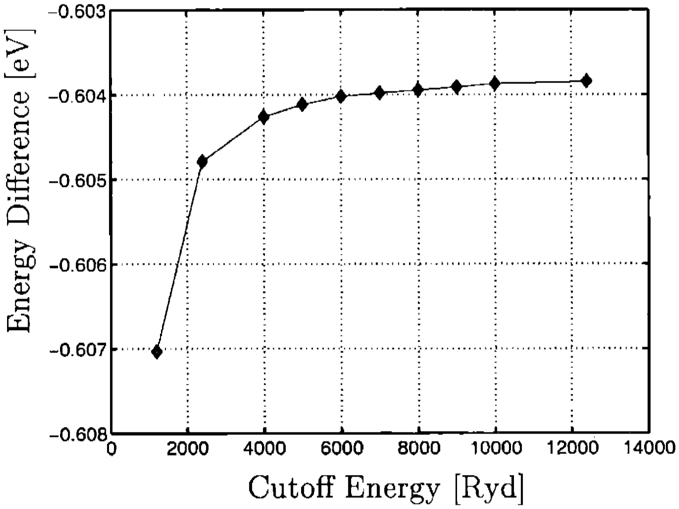

Figure 2-7: Energy difference as a function of cutoff for fcc boron, when using the traditional plane-wave approach. The volumes per atom are $V_1 = 3.83$ Å^3 and $V_2 = 3.5$ Å^3.

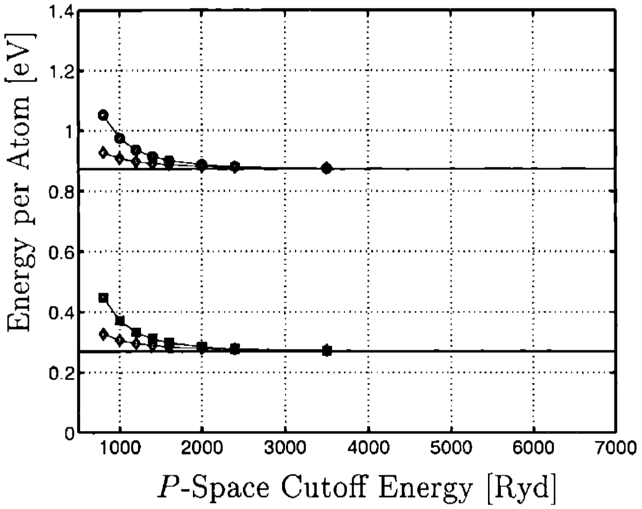

Figure 2-8: Energy convergence versus P-space cutoff, using the new method, when $E_c^Q = 7000$ Ryd. The squares correspond to $V_1 = 3.83$ Å^3, the circles correspond to $V_2 = 3.5$ Å^3 and the diamonds correspond to the transferability prediction, Equation (2.19). The horizontal lines correspond to the energy calculated using the traditional approach at a cutoff energy of 7000 Ryd.

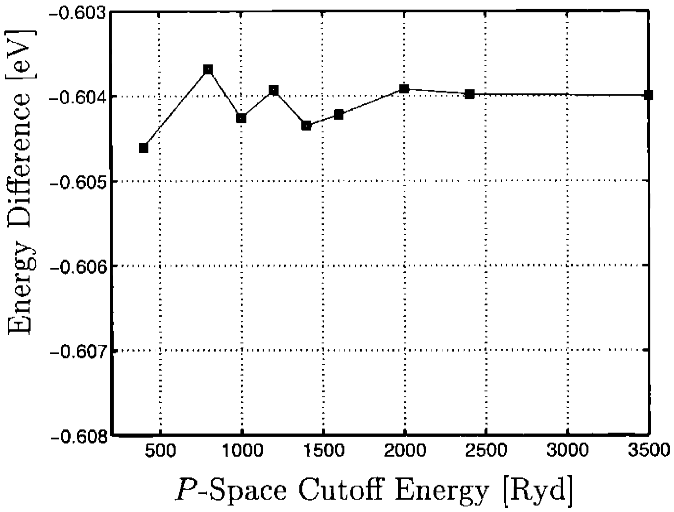

Figure 2-9: Energy difference in the new approach as a function of the P-space cutoff.

physical processes which come into play.

To make a direct comparison of computational savings, we note that the total energy and energy difference, when using the new method with $E_c^P = 1200$ Ryd and $E_c^Q = 7000$ Ryd, is very close to the traditional approach with energy cutoff $E_c^{trad} =$ 6500 Ryd. At these cutoffs, the memory savings from the perturbative approach is a factor of 12.5 for the wave functions and 2.7 for the FFT's. The time for matrix multiplications decreases by a factor of 5.4 and for Fourier transforms by a factor of 2.7 which largely compensates the need for a few more Fourier transforms in generating $\mathbf{C}^Q$ and $\mathcal{O}\mathbf{Y}^P$.

2.4 Application to High Pressure Boron

As a physical application, we study the high-pressure phases of boron, whose rich physics remains mysterious. Boron is known to exhibit a semiconducting to metallic phase transition at $\approx$ 170 GPa [27], and under high pressure and low temperatures, boron superconducts [27]. Previous theoretical studies of Boron under pressure include that of Mailhiot *et. al.* [58], who used both the LMTO method and the pseudopotential method. They have found their pseudopotential results to be more reliable and predict a sequence of structural phase transitions with increasing pressure from the icosahedral structure (α-12) to a body centered tetragonal structure (bct) to the face-centered cubic structure (fcc). They find the α-12 → bct transition to occur at 210 GPa, and established this as an upper bound for the semiconducting to metallic phase transition.

To calculate the energy for different phases in boron we use our perturbative potential approach with the analytically continued conjugate gradient approach as described in Section 2.3 with $\mathcal{O}$, $\mathbf{C}^Q$ and H^{eff} calculated as in Section 2.3.4. All calculations employ the local density approximation with the parameterization of Perdew-Zunger [72] to the Ceperley-Alder [19] exchange-correlation energy.

We consider a wider range of structures than explored previously, not only fcc, bct, and α-12 structures but also orthorhombic boron with the α-gallium and β-gallium basis. We consider these orthorhombic structures because they are the structure for gallium, another Group III element, which has as its ground-state structure α-orthorhombic at low pressures and β-orthorhombic at high pressures [23]. Below, we show that these structures play quite important roles.

For the bct structure, we use the same $c/a = 0.65$ ratio as was used in Reference [58], where this ratio was shown to give the ground state at a volume ≈ 3.91 Å^3 within the pseudopotential calculation. We have tested this ratio for a number of high pressure states and have found the ideal ratio to remain constant over a wide range of pressures. Hence, we hold c/a at this value for all calculations in our study, and thus our bct energies results represent a quite close upper-bound.

For the α-12 structure, we use the structure listed in Table 5 of Reference [23], the same used by Mailhiot *et. al.* [58]. This structure is rhombohedral with angle $\alpha = 58.06°$. The basis locations for the atomic positions are

$$\pm(x_1 x_1 z_1;\; x_1 z_1 x_1;\; z_1 x_1 x_1;\; x_2 x_2 z_2;\; x_2 z_2 x_2;\; z_2 x_2 x_2),$$

where $x_1 = 0.0104$, $z_1 = -0.3427$, $x_2 = 0.2206$ and $z_2 = -0.3677$. The space group for the α-12 structure is R$\bar{3}$m. Note that we may regard this α-12 structure as representative of the low-pressure states of boron which are all governed by the icosahedron.

For the orthorhombic structures, we use the Gallium structures as found in Wyckoff's book [109]. For the α-orthorhombic structure, we hold the lattice vector ratios to $a/b = 0.99867$ and $a/c = 0.590035$ and place the atomic basis at coordinates

$$\pm(0, u, v;\ 1/2, u + 1/2, \bar{v};\ 1/2, u, v + 1/2;\ 0, u + 1/2, 1/2 - v),$$

where $u = 0.0785$ and $v = 0.1525$. The space group is Cmca. For the β-orthorhombic structure, we hold the the lattice vector ratios at $a/b = 0.3567$ and $a/c = 0.9148$ and place the atomic basis at

$$\pm(0, u, 1/4;\ 1/2, u + 1/2, 1/4),$$

where $u = 0.133$. The space group is Cmcm. Note that we do not optimize the lattice vector ratios for the orthorhombic structures for boron but here hold them fixed to that of gallium at standard conditions. Therefore, the energies which we report for these structures should be regarded simply as upper bounds.

2.4.1 Convergence

We now establish plane wave cutoffs for our specific study which will both make for practical calculations (particularly for the α-12 structure) and give accurate structural energy differences. For this we shall compare the energy per atom as a function of volume for the fcc, bct and $\alpha 12$ structure. As these are convergence tests, we employ relatively modest Brillouin sampling: 4×4×4, 4×4×6, and 1×1×1 (the Γ point) meshes for the fcc, bct and $\alpha 12$ structure, respectively. To facilitate integration over the Fermi surface, we employ an electronic temperature of $kT \approx 0.0037$ H.

Figure 2-10 summarizes the results for the three structures when using the plane wave cutoffs from Section 2.3.4, $E_c^Q = 7000$ Ryd and $E_c^P = 1200$ Ryd. The curves

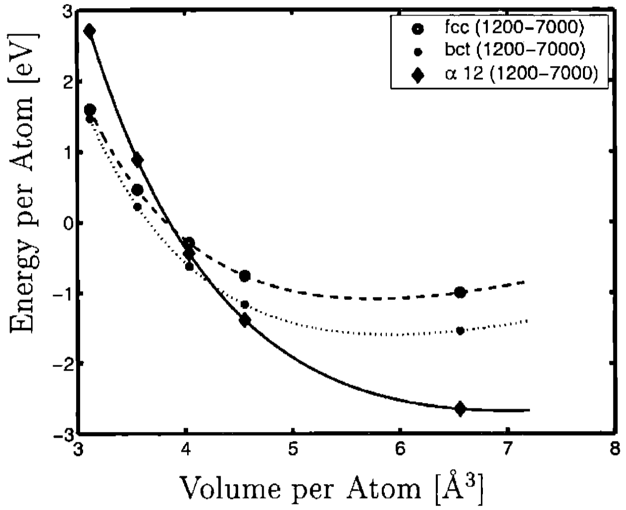

Figure 2-10: Energy per atom versus volume per atom for the fcc (circles), bct (stars) and α-12 (diamonds) structures. Energy cutoff for the P-space is 1200 Ryd and for the Q-space 7000 Ryd. The curves are fitted to Equation (2.30).

from the figure are simple fits to

$$E = a_0 + a_1 V^{-1/3} + a_2 V^{-2/3} + a_3 V^{-1}. \tag{2.30}$$

Having established previously that the above cutoffs give extremely good energy differences, we then searched for possible reductions in the cutoffs which continue to reproduce these results accurately. We find reducing the cutoffs to 200 Ryd for the P-space and 1200 Ryd for the Q-space to both lead to efficient calculations and to give highly accurate results. Figure 2-11 compares the results at this reduced cutoff (data points) with the previous results at the higher cutoffs (curves).

As a comparison, we also calculate the energy when using a traditional, direct plane-wave approach with a cutoff of 200 Ryd. Figure 2-12 shows a similar plot, where the points are the plane wave data and the curves represent the fit to the fully converged results. Note that, although fcc structure is fairly well converged at this low cutoff, there are rather large errors for the α-12 structure. Thus, such a low cutoff is unreliable for the study of such systems. The fact the low cutoff represents one structure well and not another demonstrates the unpredictability of

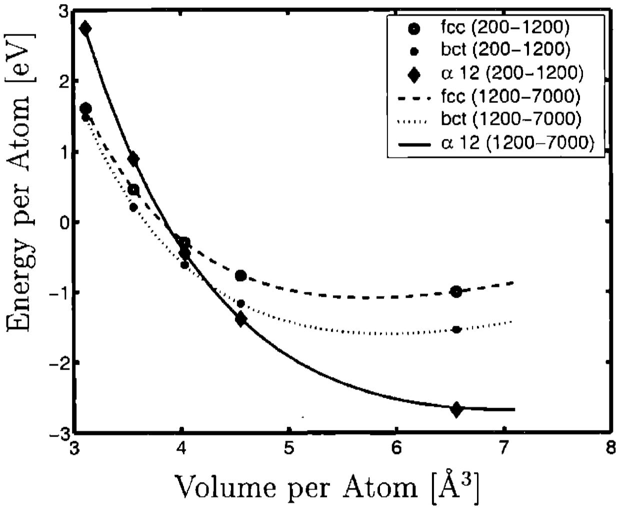

Figure 2-11: Energy per atom versus volume per atom. The results from new method using the cutoffs E_c^P=200 Ryd and E_c^Q=1200 Ryd are displayed as circles (fcc), stars (bct) and diamonds (α-12). The results from new method using the cutoffs E_c^P=1200 Ryd and E_c^Q=7000 Ryd are displayed as lines by fitting the data to Equation (2.30): fcc (dashed), bct (dotted), α-12 (solid).

transferability errors, underscores the need to predict those errors reliably, and places pseudopotential studies of such systems, which assume that errors in processes at such high energy scales cancel, in doubt.

Finally, we note that the memory savings of using the new method, with cutoffs of 200 Ryd and 1200 Ryd, versus the traditional approach, which would require a cutoff of 1200 Ryd to produce results of similar reliability, is quite substantial, a factor of $\approx$ 15 for wave functions and $\approx$ 3 for the FFT box. The time for the matrix multiplication correspondingly reduces by a factor of 6 and for the Fourier transforms by a factor of 3, similar to Section 2.3.4. Because of these savings, particularly in memory, all of our calculations below were possible on a single desktop computer and there was no need for parallel supercomputing.

2.4.2 Results

Having found appropriate plane wave cutoffs, we next converged both the Brillouin sampling and the fictitious Fermi temperature. We find that a fictitious Fermi tem-

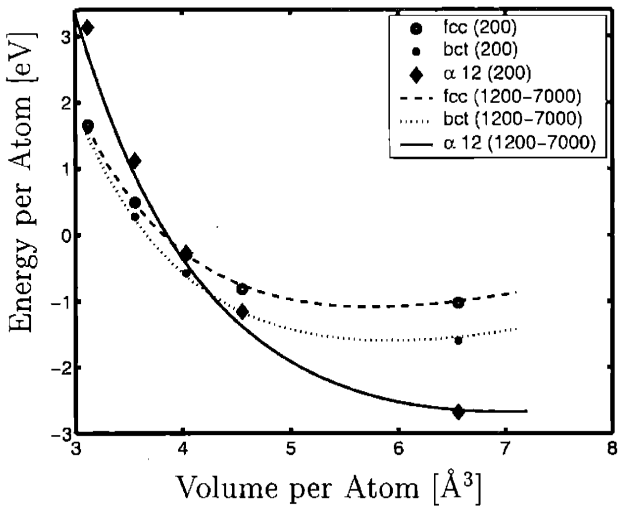

Figure 2-12: Energy per atom versus volume per atom. The results from using the traditional approach with cutoff E=200 Ryd are displayed as circles (fcc), stars (bct) and diamonds (α-12). The results from new method using the cutoffs E_c^P=1200 Ryd and E_c^Q=7000 Ryd are displayed as lines by fitting the data to Equation (2.30): fcc (dashed), bct (dotted), α-12 (solid).

perature of $kT = 0.001H$ converges the total energy to a within a few tenths of a millihartree per atom ($0.2mH$ for the fcc structure). For the fcc and bct structures, Brillouin sampling on 6×6×6 and 4×4×6 meshes, respectively, suffice to converge the total energy per atom to within the same tolerance. We then generate meshes for the remaining structures by maintaining the same reciprocal space sampling density as closely as possible, resulting in meshes of size 2×2×2, 4×4×4 and 6×4×6 for the α-12, α-orthorhombic and β-orthorhombic structures, respectively.

Figure 2-13 shows our final results, which are converged to within a few tenth of a millihartree per atom. Most notably, we find a new phase, the α-orthorhombic , to be the lowest in energy phase under high pressure. α-orthorhombic boron becomes energetically favorable over α-12 boron at a pressure of 71 GPa, and remains the energetically favored phase up to the highest pressures we have studied, which are over 500 GPa. Although there are other structures in the same icosahedral family for boron, due to the dramatic rise in energy of the α-12 structure, we do not expect these alternate structures to have a significantly lower energies. Finally, optimizing the

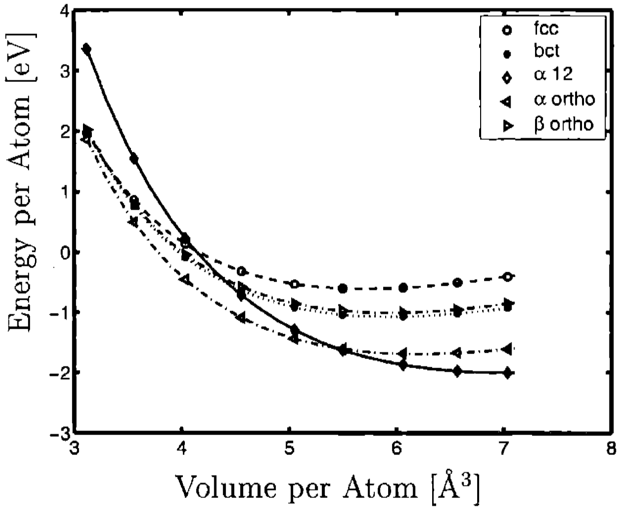

Figure 2-13: Energy per atom versus volume per atom, for the fcc (circles), bct (stars), α-12 (diamond), α-orthorhombic (left facing triangles) and β-orthorhombic (right facing triangles) structures. The results are from the new method using the cutoffs E_c^P=200 Ryd and E_c^Q=1200 Ryd.

lattice vectors ratios for the orthorhombic phases will only make them more favorable. We, therefore, expect our prediction of a phase transition from the icosahedral family to the α-orthorhombic structure to be robust.

As a point of comparison to the existing pseudopotential calculations [58], which had not considered the orthorhombic structures, ignoring those structures, we also find the sequence of transitions α-12 $\rightarrow$ bct $\rightarrow$ fcc. Although our value of 194 GPa for the first of these transitions agrees well with the pseudopotential result of 210 GPa, our prediction of $\approx$ 475 GPa for the second transition differs substantial from the pseudopotential result of 360 GPa. This large discrepancy most likely results from the inadequacies of the pseudopotential to effectively account for the response within the core. The inconsistent performance of the pseudopotential results underscores the importance of control over transferability when studying high pressure systems.

Given the availability of high-pressure resistivity data for boron [27], it is interesting to consider the electronic structure of the hitherto unexplored α-orthorhombic phases for boron. Figures 2-14 and 2-15 show low-resolution plots of the density of states for α-orthorhombic and β-orthorhombic boron at 250 GPa and 217 GPa,

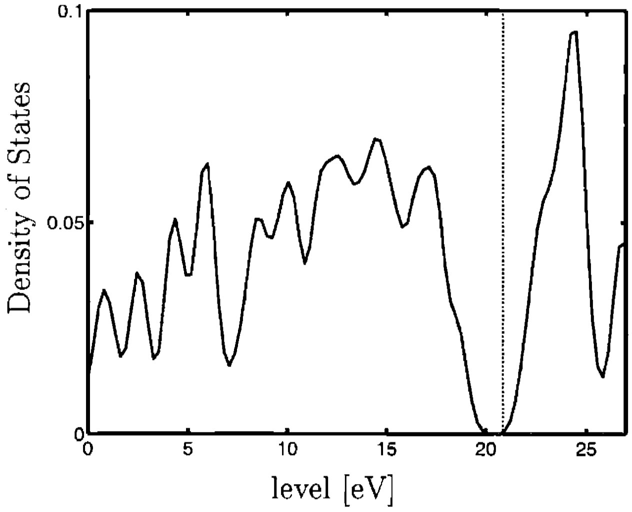

Figure 2-14: Density of states for the valence electrons for the α-orthorhombic boron structure. The straight line corresponds to the chemical potential at $kT = 0.001H$.

respectively, as generated using the Brillouin zone sampling from the total energy calculations. The plots have low resolution because, as is well known, meshes which give reliable total energies often are too modest to give detailed density of states. (Providing smooth curves required a Gaussian broadening of width 1 eV.) The figures clearly show that, whereas the β-orthorhombic phase is semimetallic, the density of states of the α-orthorhombic phase clearly exhibits a gap at the Fermi level, even at high pressures.

Experimentally, the room-temperature resistance of boron decreases discontinuously as a function of pressure at 30 GPa, 110 GPa and 170 GPa [27]. In comparing our results to these data, it is important to recall that the α-12 structure is only meant to be representative of the icosahedral family of low-pressure structures and that, with optimization of the aspect ratios, the curves for the α-orthorhombic and β-orthorhombic structures will displace to even lower energies. In particular, a downward shift of only 0.15 eV (10%) in the α-orthorhombic curve would lower our prediction for the α-12$\rightarrow$$\alpha$-orthorhombic transition from 71 GPa to 30 GPa. Thus, while further investigation is clearly needed, these data suggest that a structural transition from the icosahedral family to the orthorhombic phase is a viable candidate for the

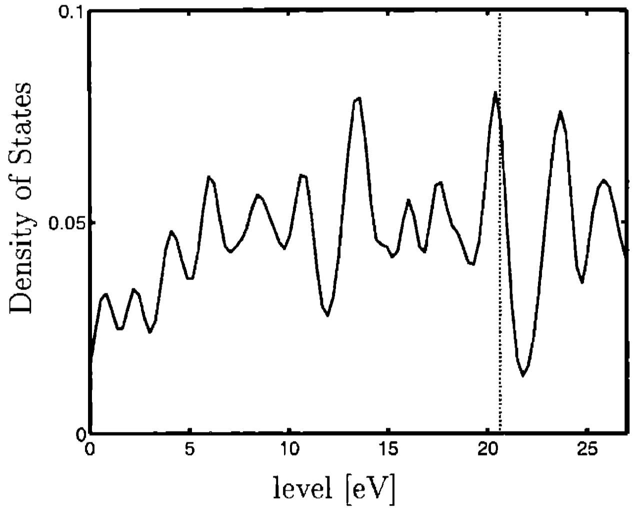

Figure 2-15: Density of states for the valence electrons for the β-orthorhombic boron structure. The straight line corresponds to the chemical potential at $kT = 0.001H$.

resistance discontinuity observed in boron at 30 GPa.

Because Boron is observed experimentally to be metallic above 160 GPa, our results imply that another, yet unexplored, structure must become energetically favored at this pressure and be responsible for the highest of the observed discontinuities in the room-temperature resistance. Whatever this metallic structure is, it cannot be simple as the fcc, bct, bcc and hcp structures because none are competitive at high pressures. It is suggestive, however, that our energetic upper-bound for the metallic β-orthorhombic structure is quite competitive with the fcc and bct structures at the very highest pressures. Although further calculations would certainly be needed to verify this conjecture, it is quite possible that the observed discontinuity in the resistivity at 170 GPa represents a structural transition from the semiconducting α-orthorhombic to the metallic β-orthorhombic phase.

2.5 Conclusions

We have developed a new method which allows for dramatic reduction in the number of plane waves needed in all-electron density functional theory calculations or in calculations with hard, but highly transferable pseudopotentials. The foundation of the approach is to treat the higher energy plane wave components of the electronic states implicitly through a perturbative approach, thereby allowing these components to be recovered quickly only when needed, thus alleviating memory storage requirements by factors as high as fifteen in practical calculations. The approach lends itself well to current optimized minimization techniques such as conjugate gradient methods and has the benefit of allowing quantitative estimates of transferability to new systems for which there is little or no experience and for which the transferability of pseudopotentials is in question, such as condensed matter at high pressure where effects in the core region become much more important.

In addition, the first application of this approach has led to new intriguing conjectures as to the structure of boron at high pressures. We have carried out the first *ab initio* calculations of the orthorhombic structures of boron, which we show to play an important role in the high pressure behavior of this material. We find that, prior to becoming metallic, boron makes a phase transition from the icosahedral family to the semiconducting α-orthorhombic structure. The low energy of this semiconducting phase indicates that the structure of the superconducting phase for boron is more complicated that the simple monotonic lattices explored to date. While further calculations including optimization of the lattice ratios for the orthorhombic phases are needed, our results lead to the conjecture that the metallic β-orthorhombic structure is a good candidate for the superconducting phase.

Chapter 3

Elasticity of nanometer-sized objects

The recent development of artificial free-standing structures of nanometer dimensions has led to great interest in their mechanical properties. A wealth of experimental information is now available for nanowires [105, 20, 69, 18] and nanotubes[105, 97, 46], and a computational literature is developing on the subject[112, 36, 57, 77, 62, 63, 15]. Many of these works make use of results from the continuum theory of elasticity to analyze the behavior of nanometer structures. However, the applicability of continuum theories to nanoscale objects, where atomic-level inhomogeneities come to the fore, has yet to be explored in depth.

Rigorous understanding of the elastic properties of nanoscale systems is crucial in understanding their mechanical behavior and presents an intriguing theoretical challenge lying at the cross-over between the atomic level and the continuum. In the absence of an appropriate theoretical description at this cross-over, critical questions remain to be answered: To what extent can continuum theories be pushed into the nanoregime? How to provide systematic corrections to continuum theory? What effects do different bonding arrangements have on elastic response? What signatures in the electronic structure correlate with the mechanical properties of the overall structure?

Recently, there have been a number of theoretical explorations of the impact of nanoscale structure on mechanical properties[15, 60, 5, 59, 83, 47]. These studies fall under two broad approaches, either the addition of surface and edge corrections to bulk continuum theories[15, 60] or the extraction of overall mechanical response from atomic scale interactions[5, 59, 83, 47]. The latter approach has the distinct advantage of allowing first principles understanding of how different chemical groups and bonding arrangements contribute to overall elastic response, thus opening the potential for the rational design of nanostructures with specific properties.

In coarse graining from interatomic interactions to mechanical response, some works rely upon the problematic decomposition of the total system energy into a direct sum of atomic energies[5, 59], which is always arbitrary and particularly inconvenient for connection with *ab initio* electronic structure calculations. The remaining works which attempt to build up overall response from atomic level contributions[83, 47] fail to account properly for the Poisson effect. Below we show that failure to account for this effect leads to surprisingly unphysical results.

This chapter presents the first theory for the analysis of overall mechanical response in terms of atomic-level observables which suffers from neither difficulty from the preceding paragraph. This analysis allows, for the first time, quantitative understanding of how continuum theory breaks down on the nanoscale, of how to make appropriate corrections, and of how to predict the effects of different bonding arrangements on overall elastic response. It is well known that the decomposition of overall elastic response into a sum of atomic level contributions is not unique. It is shown here, however, that with the additional constraint of dependence of moduli on local environment our definition of atomic level moduli becomes physically meaningful and essentially unique when coarse-grained over regions of extent comparable to the decay range of the force-constant matrix.

For concreteness, we focus on nanowires. However, a brief description will be presented of how to extend this work to any system with nanometer dimensions. This chapter proceeds as follows. Section 3.1 briefly overviews the present state of the field. Next, as the traditional concept of Young's modulus becomes ill-defined on the nanoscale well defined continuum elastic constants, appropriate for nanowires, are presented in Section 3.2. It is then shown how to decompose these constants exactly into atomic-level contributions based on true physical observables (rather than individual atomic energies) using a straight-forward application of Born and Huang's method of long waves [14], resulting in a decomposition similar in spirit to those in [83, 47] (Section 3.3). Section 3.4 demonstrates the surprising, radical breakdown of this approach when applied to nanoresonators. Then, in Section 3.5, we identify the source of the difficulty as the Poisson effect and furthermore present the first local analysis of mechanical response truly applicable to nanoresonators.

The chapter then goes on to applications. Section 3.6 verifies the physical meaningfulness of our newly defined quantities by verifying that they predict response to modes of strain for which they were not directly constructed. Then, in Section 3.7, this approach is used to generate a new, much more accurate, relationship between experimentally accessible observables describing response to flexural and extensional strain in nanomechanical resonators. Finally, Section 3.8 uses this theory to explore possible links between underlying electronic structure and local elastic response.

3.1 Overview

As this introduction mentions, the literature pursues two broad categories of approach to the study of mechanical properties on the nanoscale, either surface and edge corrections to continuum theory or extraction of overall response from the underlying atomic interactions. In the former category, Reference [15], through scaling arguments and numerical examples, notes that the Young's modulus for nanomechanical resonators scales as a bulk term plus surface and edge corrections. Although providing insight and motivation, this work leaves completely open how one should understand these corrections from first principles. Reference [60] provides a more rigorous study based on separating nanoscale systems into continuum surface and bulk regions. This latter approach allows prediction of changes in stiffness properties as one approaches nanometer length scales and has the appeal of generating physically motivated correction terms. However, it relies on the separation of a nanomechanical resonator into bulk and surface continua as an *ansatz* and therefore neither predicts when such a picture suffices to give an accurate description nor prescribes further corrections.

References [5, 59, 83, 47], on the other hand, start from the more general atomic level description and then try to unveil physical properties from the underlying atomic description. It is important to note that these works do not deal directly with nanoscale systems but rather focus on the effects of nanoscale inhomogeneities in *bulk* systems.

References [5] and [59] concern the elastic properties of grain boundaries. These works define atomic-level elastic moduli as the second derivative of the energy associated with each atom with respect to strain and then go on to study the behavior of such moduli near grain boundaries. The difficulty with this approach is that it requires a breakdown into individual contributions from each atom of the total energy of any system. Such an atomic energy is neither observable nor uniquely defined and therefore cannot serve as an appropriate basis for theoretical understanding.

Although References [83] and [47] work from valid physical observables, the components of the force-constant matrix, these works focus on bulk-like or mesoscopic scale systems and fail for nanoscale systems for the reasons which that will be described in this chapter. Reference [83] investigates nonlocal elastic constants on the mesoscopic scale and links them to the underlying atomic interactions. It then proceeds to define an elastic constant for each atom and studies the behavior of these quantities near surfaces and grain boundaries. Reference [47] defines a bond frequency from the force-constant matrix from which it deduces the possibility of bond rupture during crack nucleation. Neither of the above works properly accounts for the Poisson effect, which is shown in Sections 3.3, 3.4 and 3.5 to play a critical role in the elasticity of nanoscale systems. Moreover, straightforward generalization of these works to include this effect fail for the the same reasons as does the related approach which is described in Section 3.3.

3.2 Nanowire rigidities

The prime difficulty in the application of continuum theory to objects of nanometer cross-section is the loss of the ratio of the inter-atomic spacing to the cross-sectional dimension as a small parameter. However, so long as the length of an object and the wavelength of the distortions considered both greatly exceed the inter-atomic spacing and the cross-sectional dimension, the object properly may be viewed as a one-dimensional continuum. Although this work focuses on nanowires, the generalization of the discussion below to nanoscale systems of other dimensionality such as thin plates or nanoscopic objects is straightforward.

Viewed as a linear continuum, the free energy per unit length f of a nanowire is

$$f = (Eu^2 + FR^{-2} + T\tau^2)/2, \tag{3.1}$$

where u is the linear strain of extension, R is the radius of curvature and τ is the rate of twist of the torsion. The coupling constant E is the *extensional rigidity*, F is the *flexural rigidity* and T is the *torsional rigidity*. Unlike traditional bulk continuum concepts, the free-energy function Eq. (3.1) is observable in principle and thus provides an unambiguous operational definition of the rigidities. The use of traditional continuum concepts, such as the Young's modulus and the cross-sectional area, is avoided because such concepts are neither uniquely nor well-defined for nanoscale systems.

The rigidities in Eq. (3.1) are related to the phonon frequencies through

$$\begin{aligned} \omega_{LA} &= \sqrt{E/(\lambda m)}q, & (3.2)\\ \omega_{TA} &= \sqrt{F/(\lambda m)}q^2, & (3.3)\\ \omega_{RA} &= \sqrt{T/(\lambda m I_r)}q, & (3.4) \end{aligned}$$

where ω is the frequency for either the longitudinal, transverse or rotational acoustic modes, respectively, λ is the linear atomic number density, q is the wave vector and m is the mass of a single atom. (This work focuses on single species systems for simplicity.) Finally, I_r is defined unambiguously as the mean rotational moment $I_r = (1/N_c) \sum_\alpha (x_\alpha^2 + y_\alpha^2)$, where the sum ranges over all atoms in the cell, N_c is the number of atoms per unit cell, the wire is assumed to run along the z-axis and the origin lies on the center line of the wire.

Finally we note, that although the rigidities in Eq. (3.1) are well-defined, certain traditional continuum relations between them do not hold. Specifically, we show below that the traditional continuum relationship between the extensional rigidity E and the flexural rigidity F, which has recently been used in the analysis of experiments[105, 97, 46, 69], fails on the nanoscale.

3.3 Method of long waves

One reason for breakdown of traditional continuum relations on the nanoscale is that the continuum perspective course grains away important fluctuations which occur over distances on the order of the inter-atomic spacing. To overcome this shortcoming we propose to course grain only on distances over which the underlying interatomic interactions vary, the decay length of the force-constant matrix. The straightforward approach to generate such a theory is the "method of long waves" developed by Born and Huang[14], which is somewhat similar to the approaches which have been used previously to defects in bulk systems[83, 47]. This section applies the method of long waves to nanoresonators. The next section shows how, surprisingly, this and related approaches fail in the study of systems with free surfaces and therefore, in general, cannot be used to describe nanoscale systems. Section 3.5, describes how to go beyond the straightforward application of the "method of long waves" in order to achieve a meaningful description.

Initially longitudinal waves are focused on and, as noted in Section 3.2, we choose our origin to lie on the center line of the wire, which runs along the z-axis. For nanowires, the presence of surfaces breaks periodicity in the transverse directions resulting in a one-dimensional crystal with an extremely large unit cell of length $L_c = N_c/\lambda$, where N_c and λ are as in Section 3.2. In all expressions below, boldfaced quantities are $3N_c$-dimensional and arrowed vector quantities are three-dimensional. Finally, sums with Greek indices range over atoms in the unit cell.

To relate the rigidities to the dynamical matrix, we begin similarly to Born and Huang and choose to factor the Bloch phases (e^{iqz}) out of the representation of the phonon polarization vector **u**, incorporating them into the definition of the dynamical matrix **D**, so that the acoustic phonon polarization vectors are periodic across the cell boundaries. This ensures a uniform description of the distribution of elastic energy along the axis of the wire. To generate a scalar equation for the phonon frequency, Born and Huang project the secular equation for the dynamical matrix,

$$\mathbf{D}\mathbf{u} = -m\omega^2\mathbf{u}, \tag{3.5}$$

against the zeroth-order polarization vector $\mathbf{u}^{[0]}$. Here, however, to more symmetrically represent the distribution of elastic energy, the full polarization vector **u** is projected onto Equation (3.5). Equating the frequency ω in Eq. (3.5) with the longitudinal frequency in Eq. (3.2) gives

$$-\frac{E}{\lambda} = \frac{[\mathbf{u}^{\dagger}\mathbf{D}\mathbf{u}]^{[2]}}{\mathbf{u}^{\dagger}\mathbf{u}} = \sum_{s,t=0}^{1} \frac{(-1)^s}{N_c}\, \mathbf{u}^{\dagger[s]}\, \mathbf{D}^{[2-s-t]}\, \mathbf{u}^{[t]}, \tag{3.6}$$

where the numerator of the Rayleigh quotient has been expanded to second-order in powers of (iq) and where the 3×3 sub-block of $\mathbf{D}^{[n]}$, which couples atoms α and β, is

$$[\mathbf{D}^{[n]}]_{\alpha\beta} = \frac{1}{n!}\sum_{\vec{R}} \Phi_{\alpha\beta}(\vec{R}) \left(\hat{z}\cdot(\vec{R}+\vec{\tau}_\beta-\vec{\tau}_\alpha)\right)^n. \tag{3.7}$$

Here, $\vec{R}$ is a lattice vector along the $z-axis$, $\Phi_{\alpha\beta}(\vec{R})$ is the 3×3 sub-block of the force-constant matrix which couples atoms α and β located at positions $\vec{\tau}_\alpha$ and $\vec{R}+\vec{\tau}_\beta$, respectively, and

$$\Phi_{\alpha\beta}(\vec{R}) = -\frac{\partial^2 U}{\partial\vec{\tau}_\alpha \partial(\vec{R}+\vec{\tau}_\beta)},$$

where U is the energy of the unit cell.

Finally, substituting Eq. (3.7) and $[\mathbf{u}^{[0]}]_\alpha = \hat{z}$ into Eq. (3.6), allows E to be expressed as a sum over atoms (α) in the unit cell and all atoms ($\beta, \vec{R}$) in the system,

$$\begin{aligned} E &= \frac{1}{L_c}\sum_{\alpha} e_\alpha && (3.8) \\ e_\alpha &= \sum_{\beta\vec{R}}\Big\{ -\Delta\vec{Z}_{\alpha\beta}\cdot\Phi_{\alpha\beta}(\vec{R})\cdot\Delta\vec{Z}_{\alpha\beta}/2 + \vec{u}^{[1]}_{\alpha}\cdot\Phi_{\alpha\beta}(\vec{R})\cdot\vec{u}^{[1]}_{\beta} \\ &\quad +\Delta\vec{Z}_{\alpha\beta}\cdot\Phi_{\alpha\beta}(\vec{R})\cdot\vec{u}^{[1]}_{\beta} - \vec{u}^{[1]}_{\alpha}\cdot\Phi_{\alpha\beta}(\vec{R})\cdot\Delta\vec{Z}_{\alpha\beta}\Big\}. && (3.9) \end{aligned}$$

Here, $\Delta\vec{Z}_{\alpha\beta} \equiv \hat{z}\hat{z}\cdot(\vec{\tau}_\alpha - \vec{\tau}_\beta - \vec{R})$, $\vec{u}^{[1]}_{\alpha}$ is the first-order polarization vector and e_α is refered to as the "atomic moduli".

The atomic moduli as currently defined in Eq. (3.9) provide a useful microscopic analysis of elastic response in bulk systems which is similar in spirit to the decompositions used previously in the study of bulk material systems [83, 47]. To see that Eq. (3.9) indeed decomposes the overall elastic response of bulk systems into atomic contributions coarse-grained over distances on the order of the decay-length of the force-constant matrix, first we note that for infinite bulk systems, elastic waves are planar. This implies that the first-order polarization vector ($\vec{u}^{[1]}_{\alpha}$) is uniform from primitive cell to primitive cell and thus depends only on the local environment of each atom. Next, we note that although the strain terms ($\Delta\vec{Z}_{\alpha\beta}$) scale linearly with distance between atoms, the terms which contribute to the final result are bounded in range by the inter-atomic interactions ($\Phi(\vec{R})$). Thus, the atomic moduli depend only on the local atomic environment over distances which the decay of the force-constant matrix determines.

3.4 Failure of straightforward approach in nanowires

It is now demonstrated through direct calculations that the approach outlined in the previous section gives unphysical results when applied to nanoresonators. Specifically, this section studies the behavior of [100]-oriented nanoresonators of silicon, which recent *ab initio* studies[43] predict to undergo a size-dependent structural phase transition between the two structures in Figure 3-1 at a cross-section of ~3 nm. (The inter-

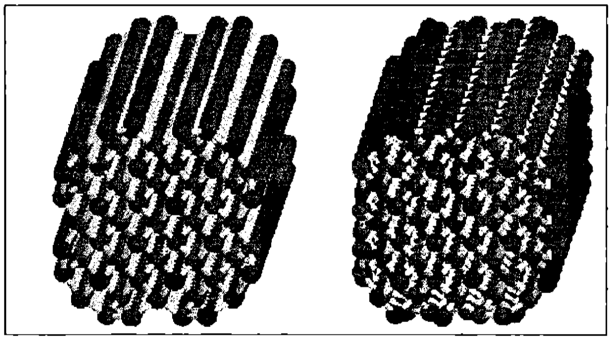

Figure 3-1: Atomic structure of silicon nanowires with an approximate cross-sectional diameter of 1.5 nm. The wires are viewed along the longitudinal axis: $c(2 \times 2)$ structure (left), 2×1 structure (right).

ested reader may refer to Reference[43] for explicit details of the microscopic structure of these wires.) Initially, we use the Stillinger-Weber inter-atomic potential[88], which suffices for the exploration of general nanoelastic phenomena and which allows study of cells with many thousands of atoms. Later in the chapter (Section 3.8) we use the Sawada tight-binding model[79] with modifications proposed by Kohyama[52] to explore the correlation between our local approach and the underlying electronic structure. For all calculations below, the atomic coordinates, the periodicity of the wire and, need be, the electronic structure are fully relaxed. Finally, periodic boundary conditions along the z-direction are employed.

Figure 3-2a shows that the atomic moduli e_α predicted for nanowires using the straightforward approach of Eq. (3.9) are unphysical in that they depend upon the macroscopic dimensions of the system and not simply on the local environment of each atom. In particular, the atomic moduli on the surface grow linearly with the diameter of the wire and the moduli in the center of the wire fail to approach the expected bulk limit, $e_b \equiv Y_b/\rho_b$, where Y_b is the Young's modulus in bulk and ρ_b is the number density in bulk. (Note that these two effects are interelated, as the moduli must sum to give the macroscopic value in the bulk limit.)

Although one has some freedom in choosing the terms used in the perturbation expansion Eqs. (3.5) and (3.6), for example to project Eq. (3.5) against $\mathbf{u}^{[0]}$ instead of $\mathbf{u}$, all such expansions will lead to similar linear scaling along the surface of the

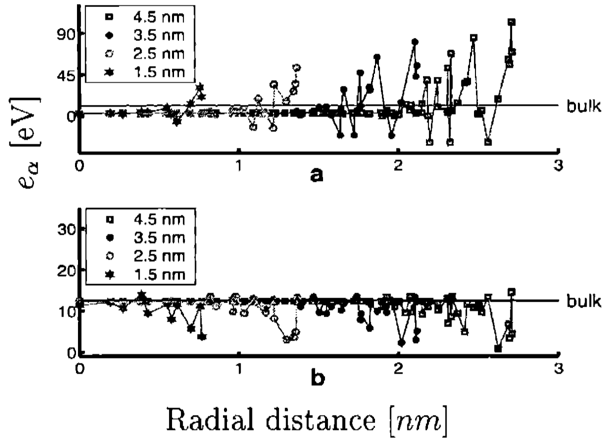

Figure 3-2: Predictions of atomic moduli e_α for $c(2\times2)$ nanowires of varying diameter: (a) straightforward theory (Eq. (3.9)) and (b) new theory (Eq. (3.11)). The insets denote the approximate diameters of the wires. The value of the atomic modulus (Eq. (3.9) or Eq. (3.11)) is along the ordinate and radial distance of the atom from the center line is along the abscissa.

wire and approach an incorrect value at the center of the wire. Thus, straightforward application of the method of long waves fails to result in a local, and hence physically meaningful, description of elastic response in nanoscale systems, as will straightforward variations thereon such as those in References [83, 47].

3.5 Method of long waves in nanowires

To cure the difficulties uncovered in the previous section, we first identify the cause of the pathological behavior and then exploiting the freedom in Eq. (3.9) this pathology is removed.

The failure of the straightforward approach arises from the fact that elastic waves in nanoresonators, or any system with free surfaces, are not strictly planar. In particular, the Poisson effect, which the first order polarization vector $\mathbf{u}^{[1]}$ contains, causes each atom to displace by an amount in direct proportion to its distance from the center line of the system. Eq. (3.9) then leads directly to linear scaling of the atomic moduli at the surfaces of the wire.

Defining an atomic elastic reponse dependent soley on the local enivornment requires separation of extensive elastic effects from intensive nanoscopic effects. To seperate the extenive motion in the first order polarization vector from that of its intensive motion, we define the atomic displacements ($\vec{u}^{rl}_\alpha$) as the intensive nanoscopic motions,

$$\vec{u}^{rl}_\alpha \equiv \vec{u}^{[1]}_\alpha - (-\sigma_x \hat{x}\hat{x} \cdot - \sigma_y \hat{y}\hat{y}\cdot)\,\vec{\tau}_\alpha, \tag{3.10}$$

where $\sigma_{x,y}$ are the Poisson ratios. There are three logical choices for the Poisson ratios: some sort of local atomic definition, an overall average for the wire, or the bulk values. We choose to use bulk Poisson ratios for a number of reasons. First, a locally varying definition makes it impossible to exploit the continuous rotational and translational symmetries in the dynamical matrix, which is found necessary to employ below in constructing atomic moduli with local behavior. Second, only by employing the bulk (rather than average) Poisson ratios is a definition found which approaches the appropriate bulk value in the centers of wires of finite width. Finally, we note that one always has the freedom of working with bulk Poisson ratios because any motion along the surface in addition to that resulting from bulk Poisson effect will not scale extensively with the diameter of the wire and can therefore be incorporated into the intensive atomic displacements $\vec{u}^{rl}_\alpha$.

After making the decomposition in Eq. (3.10), the continuous rotational and translational symmetries of the dynamical matrix are exploited to eliminate all extensive dependencies in Eq. (3.9). Appendix B outlines the procedure for doing this, which then transforms Eq. (3.9) into

$$\begin{aligned} e_\alpha = \sum_{\beta \vec{R}} \Big\{ & - \Delta\vec{r}_{\alpha\beta} \cdot \Psi_{\alpha\beta}(\vec{R}) \cdot \Delta\vec{r}_{\alpha\beta}/2 + \vec{u}^{rl}_\alpha \cdot \Phi_{\alpha\beta}(\vec{R}) \cdot \vec{u}^{rl}_\beta \\ & + \Delta\vec{r}_{\alpha\beta} \cdot \Phi_{\alpha\beta}(\vec{R}) \cdot \vec{u}^{rl}_\beta - \vec{u}^{rl}_\alpha \cdot \Phi_{\alpha\beta}(\vec{R}) \cdot \Delta\vec{r}_{\alpha\beta} \Big\}, \end{aligned} \tag{3.11}$$

where $\Delta\vec{r}_{\alpha\beta}$ represents the *total* strain between atoms α and β,

$$\Delta\vec{r}_{\alpha\beta} \equiv (-\sigma_x\hat{\mathbf{x}}\hat{\mathbf{x}} - \sigma_y\hat{\mathbf{y}}\hat{\mathbf{y}} + \hat{\mathbf{z}}\hat{\mathbf{z}}) \cdot (\vec{\tau}_\alpha - \vec{\tau}_\beta - \vec{R}),$$

and $\Psi_{\alpha\beta}(\vec{R})$ renormalizes as

$$\Psi_{\alpha\beta}(\vec{R}) \equiv 2\Phi_{\alpha\beta}(\vec{R}) - \left(\mathrm{Tr}\,\Phi_{\alpha\beta}(\vec{R}) \cdot \Sigma\right) \Sigma^{-1},$$

where $\Sigma_{jk} \equiv \delta_{jk}\sigma_j$, is a diagonal 3×3 matrix with elements σ_x, σ_y and $\sigma_z \equiv -1$, respectively and δ_{jk} is the Kronecker delta.

This new construction ensures that the modulus of each atom depends only upon its local atomic environment because $\vec{u}^{rl}_\alpha$ no longer includes extensive motions and, although $\Delta\vec{r}_{\alpha\beta}$ still depends on relative atomic distances, the renormalized Ψ decays as Φ does. Thus, it is now the range of the force-constant matrix which controls the size of the neighborhood upon which each atomic modulus can depend. Therefore, the moduli of atoms in the interior now *must* correspond to the expected bulk value, the moduli of the atoms on the surface now *cannot* depend upon the extent of the system, and the resulting description is physically meaningful. Figure 3-2b illustrates the success of Eq. (3.11).

The fact that decomposition of elastic response into atomic level contributions is not unique raises questions as to the physical meaning of such a decomposition. Our new decomposition Eq. (3.11) is the first which remains dependent only upon local environment for systems with free surfaces. Any other definition *which respects locality* can only redistribute portions of each atom's modulus among other atoms within a region of extent comparable to the decay of the force-constant matrix. Any sum over such a region of the moduli will always be nearly the same. Therefore, coarse grained over such regions, properly localized atomic moduli become physically meaningful. Section 3.6 and Appendix C demonstrate this explicitly by comparing the predictions for flexion from either properly localized moduli or straightforwardly defined moduli, respectively. To further demonstrate that alternate local definitions are equivalent in this coarse-grained sense, we have explored alternate local constructions. In particular, while the present construction takes care to employ the continuous symmetries of the dynamical matrix in such a way so as to respect symmetry among the x, y, z Cartesian coordinates, atomic moduli have also been constructed while treating the x, y coordinates symmetrically but not the z coordinate and we have found nearly identical results for all of the applications below.

This section is closed with a brief description of how the above approach extends to any system of nanometer dimensions. To be considered small in this context, a dimension must be much smaller than the wavelength of the distortions considered. This thesis focuses on nanowires, systems with two small dimensions. For a system with one small dimension, for instance a plate with nanometer thickness, the above approach develops in the same way with the one minor change that the definition of $\vec{u}_{\alpha}^{rl}$ (Eq. (3.10) involves the Poisson effect only in the one small dimension. For an object with three small dimensions, for instance adiabatic loading of a nano-object, the nature of the Poisson effect depends upon the mode of loading, and the system should treated as either of the above cases accordingly. Finally, objects of no small dimension, and hence no Poisson effect, can be described straightforwardly as bulk-like using Eq. (3.9).

3.6 Transferability

To establish that these newly defined atomic moduli are not mere convenient mathematical constructions but are physically meaningful, we now consider their transferability to phenomena not considered in their original construction. In particular, we consider flexion, where the elastic distortion is no longer homogeneous throughout the cross-section.

If our newly defined atomic moduli are indeed a measure of the local elastic response, then under flexion the free energy per unit length will take the form

$$f = (1/L_c) \sum_{\alpha} e_{\alpha} u_{\alpha}^2 / 2, \tag{3.12}$$

where u_α is a measure of the longitudinal strain which atom α experiences. For this form to be sensible, the diameter D of the wire must not become comparable to the range of the force-constant matrix so that the atoms which contribute to each e_α all experience similar strains u_α.

Within continuum theory, uniform flexion with radius of curvature R corresponds to a longitudinal strain which varies linearly across the wire, $u = x/R$. (This holds to better than to two parts in 10^3 for all wires in this thesis.) This would then predict a flexural rigidity of

$$F_{at} = \frac{1}{L_c} \sum_\alpha e_\alpha {x_\alpha}^2. \tag{3.13}$$

Figure 3-3a shows the fractional error (δF_{at})

$$\delta F_{at} \equiv (F_{at} - F)/F, \tag{3.14}$$

in predicting the flexural rigidity from Eq. (3.13), where F is determined directly through numerical calculations. The figure shows that these errors are indeed quite small. Note that use of the straightforward definition in Eq. (3.9) with its unusually scaling surface moduli leads to invalid predictions for flexion. (Appendix C shows this directly through scaling arguments.) As a result, to have *predictive* power, definitions of atomic moduli must properly account for the Poisson effect.

To demonstrate that this new approach has greater predictive power than traditional continuum approaches, the figure also shows the fractional error (δF_{tc}) in predicting the flexural rigidity when using the traditional continuum relation

$$\begin{aligned} F_{tc} &= E(I/A), & (3.15)\\ \delta F_{tc} &= (F_{tc} - F)/F & (3.16) \end{aligned}$$

where I/A defines the mean bending moment, which is defined unambiguously as

$$I/A = (1/N_c) \sum_\alpha x_\alpha^2. \tag{3.17}$$

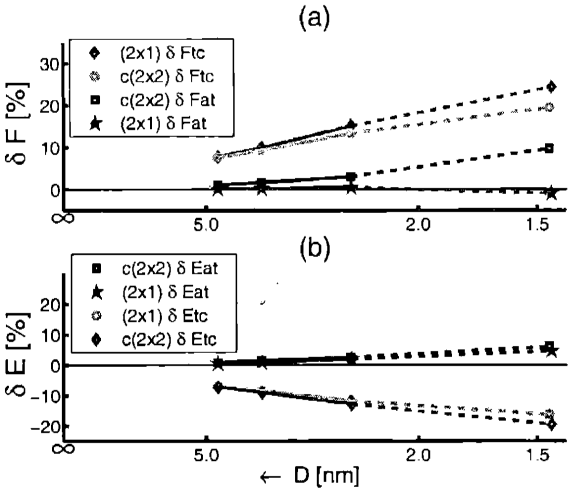

Figure 3-3: Fractional error as a function of inverse diameter $1/D$ in predicting (a) flexural rigidity from extensional properties (δF_{at}, Eq. (3.14) and δF_{tc}, Eq.(3.16)) and (b) extensional rigidity from flexural properties (δE_{at}, Eq. (3.20) and δE_{tc}, Eq. (3.21)). Note, for convenience, the abscissa is labeled by D and not $1/D$.

The linear behavior of the fractional error δF_{tc} as a function of $1/D$ indicates that continuum theory does not properly account for surface effects, a result of the fact that flexion places a larger emphasis on the surface than does extension. The dramatic improvement from the use of Eq. (3.13) arises because the atomic moduli place proper emphasis on the surface and on the interior, as they properly treat each atomic environment locally. The atomic moduli therefore properly account for elastic fluctuations along the cross-section of the wire which are on scales too small for traditional continuum theories to capture.

Finally, the only appreciable error within the new framework occurs for the smallest wires (D$\approx$ 1.5nm). At this point, the cross-sectional dimension becomes comparable to the range of the force-constant matrix, and Eq. (3.12) represents an improper use of the physical concept of atomic moduli. As described above (second from last paragraph in Section 3.5), only sums of atomic moduli over regions of extent comparable to the range of the force-constant matrix carry physical meaning. Any sum sensitive to variations over shorter scales, as is Eq. (3.12) when limited to wires narrower than the range of the force-constant matrix, cannot be depended upon to lead to meaningful results. This underscores the fact that properly construed atomic moduli are not truly atomic-level quantities but a concept coarse grained over the range of the force constant matrix. As it has been seen, however, this coarse-graining is on scales significantly smaller than those captured by traditional continuum theory.

3.7 Extension from flexion

Our newly defined atomic moduli is now applied to derive a new relation for the extensional modulus in terms of the flexural modulus and other experimentally accessible observables, a relation often needed in experimental analyses [105, 97, 46, 69]. It is then show that the new relation is much more accurate than the standard continuum-theory based relation currently employed in experimental analyses. Finally, our concept of atomic moduli is employed to provide quantitative insight into the improvement of our new relation over the traditional continuum relation.

The basis for the following analysis is the fact that Eq. (3.13) gives a very good estimate of the true flexural modulus, as Figure 3-3a confirms. Using the exact relation for E, Eqs. (3.8) and (3.11), and Eq. (3.13), we derive the following leading-order prediction E_{at} for the extensional modulus,

$$E_{at} = \frac{1}{2}\left(\frac{F}{I/A} + Y_b\frac{\lambda}{\rho_b}\right), \tag{3.18}$$

with a predicted error $\delta E_{at}^{(p)}$ of

$$\delta E_{at}^{(p)} = \frac{N_s}{EL_c}\left\{B_{at}\left[\langle e_s\rangle_{x^2} - e_b\right] + \left[\langle e_s\rangle_{x^2} - \langle e_s\rangle\right]\right\}. \tag{3.19}$$

Here, N_s is the number of "surface" atoms, defined as those for which e_α differs significantly from the limiting bulk value e_b, $\langle e_s\rangle_{x^2}$ is the inertia weighted average surface moduli

$$\langle e_s\rangle_{x^2} \equiv \frac{\sum_s e_s x_s^2}{\sum_s x_s^2},$$

with the sums ($\sum_s$) ranging over "surface" atoms, $\langle e_s \rangle$ is the average surface moduli

$$\langle e_s \rangle \equiv \frac{1}{N_s} \sum_s e_s$$

and

$$B_{at} \equiv (1/2) \frac{\frac{1}{N_s} \sum_s x_s^2}{\frac{1}{N_c} \sum_c x_c^2} - 1,$$

where $\sum_c$ implies sums over all atoms in the unit cell. This result holds for any division of the atoms into "surface" and "bulk" to the extent that each "bulk" atom has atomic modulus e_b.

Figure 3-3b shows the relative error δE_{at},

$$\delta E_{at} = (E_{at} - E)/E, \tag{3.20}$$

between the extensional modulus E determined directly from numerical calculation and as determined from our new relation, Eq. (3.18). (Note that $\delta E_{at}^{(p)} = \delta E_{at}$ exactly when the moduli prediction $F_{at} = F$ holds.) As the relevant point of comparison, the figure also shows the relative error δE_{tc},

$$\delta E_{tc} = (E_{tc} - E)/E, \tag{3.21}$$

associated with the traditional continuum result

$$E_{tc} = F \frac{A}{I}. \tag{3.22}$$

Hence, Eq. (3.18) is much more accurate than the standard continuum result Eq. (3.22).

To understand the improvement of the new relation, Eqs. (3.8) and (3.13) may also be combined to yield a prediction for the fractional error in the traditional continuum analysis,

$$\delta E_{tc}^{(p)} = \frac{N_s}{E L_c} \left\{ B_{tc} \left[\langle e_s \rangle_{x^2} - e_b \right] + \left[\langle e_s \rangle_{x^2} - \langle e_s \rangle \right] \right\}, \tag{3.23}$$

which takes *precisely* the same form as Eq. (3.19) except for the change in the prefactor in the first term from B_{at} to $B_{tc} \equiv 2B_{at} + 1$. For continuous wires of homogeneous circular or regular polygonal cross-section, we have exactly $B_{at} = 0$. Thus, generally we expect B_{at} to be close to zero and B_{tc} to be close to unity. It is now noted that the term in the first set of square brackets ($[\langle e_s \rangle_{x^2} - e_b]$) in both Eq. (3.19) and Eq. (3.23) is an average difference between surface and bulk atoms and, therefore, is generally much larger than the term in the second set of square brackets $[\langle e_s \rangle_{x^2} - \langle e_s \rangle]$, which is the difference between two differently weighted averages over the surface atoms. Thus the larger term nearly vanishes in our new relation, Eq. (3.19), but not in the traditional continuum relation, Eq. (3.23). From this analysis, it is seen that the reason why the traditional continuum relation has larger errors is that it does not properly differentiate between the local surface and bulk environments.

The atomic moduli also lead to a quick, intuitive argument to understand the improvement of Eq. (3.18) over Eq. (3.22). From the results it is seen that the surface moduli can be quite different than those of the bulk. It is also known that flexion places larger emphasis on the surface than does extension. If the average surface modulus is less/more than that of the bulk then the first term in Eq. (3.18) $(F \cdot A/I)$ will underestimate/overestimate the extensional rigidity, while the second term will overestimate/underestimate it. Therefore, errors will tend to cancel in the average of the two.

3.8 Correlation between local atomic moduli and electronic structure

The local atomic moduli are know used to explore the link between local elastic properties and the underlying electronic structure. To do this, we calculate the atomic moduli, Eq. (3.11), for both the $c(2 \times 2)$ and (2×1) structures, using the Sawada [79] tight-binding model with modifications proposed by Kohyama[52]. Various wires have been studied, all of which give similar results. For brevity, we report only wires with cross-sectional diameter $\approx$ 2.4nm. The supercell of our calculation is four bulk cubic lattice constants long in the periodic direction, and hence sampling the Brillouin zone at the Γ point in the electronic structure calculations is more than sufficient.

The left panels of Figures 3-4 and 3-5 show the resulting atomic moduli, with values color coded so that yellow corresponds to the bulk value (17.1 eV/atom). The figure shows that deviations from this value concentrate near the surface in patterns characteristic of the structure of the wire. Moduli near the surface fluctuate widely, ranging from 6-27 eV/atom for the $c(2 \times 2)$ structure and from 4-26 eV/atom for the 2×1 structure.

To allow comparison with the underlying electronic structure, the right panels in the figures display the valence charge densities from the tight-binding calculation projected (integrated along the wire axis) onto the cross-section of the wire. (To compute the electron density from the tight-binding coefficients, orbitals from a density functional calculation of the silicon atom are employed.) The figures display the electron densities using a color map similar to that employed for the atomic moduli. Intriguingly, there is an apparent correlation between the values of the atomic moduli and the underlying electron density. In particular, large/small atomic moduli correlate with regions of large/small electron density in Figure 3-4, indicating that charge distribution along the surface of these wires greatly affects the local elastic properties and thereby the overall elastic response, particularly to flexion which emphasizes surface effects. Figure 3-5 exhibits a similar correlation, but not as pronounced. Note that, in this figure, coincidence of red atomic moduli just under the surfaces of the first layer of atoms correlates with red charge densities in the same location.

Unlike in the classical potential case, where properly defined surface moduli are systematically lower or equal to the bulk value due to decrease in the number of bonds (Figure 3-2b), we find that in a quantum model, surface moduli may even greatly exceed the bulk value due to changes in local charge density which can enhance the mechanical strength of bonds (Figures 3-4 and 3-5.) This contrast underscores both the importance of considering contributions of the electronic structure to mechanical response and the need for a definition of atomic moduli which can be computed from physical observables obtainable from electronic structure calculations.

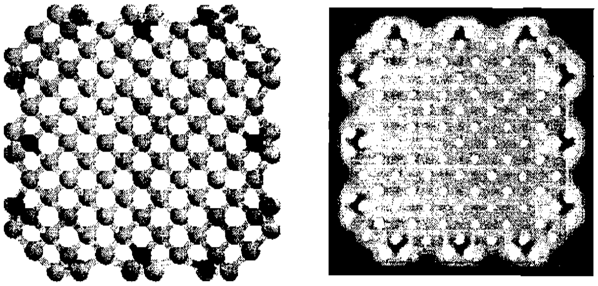

Figure 3-4: $c(2 \times 2)$ wire, with cross-section ≈ 2.4nm. Results are from the tight-binding model described in the text. Left: atomic moduli color coded from small to large: blue-green-yellow-red. Right: valence electronic density projected (integrated along the wire axis) onto the cross-section color coded from low to high: blue-green-yellow-red. White dots in the right figure indicate the location of atom cores. Note the correlation of large atomic moduli with large charge density along the surface.

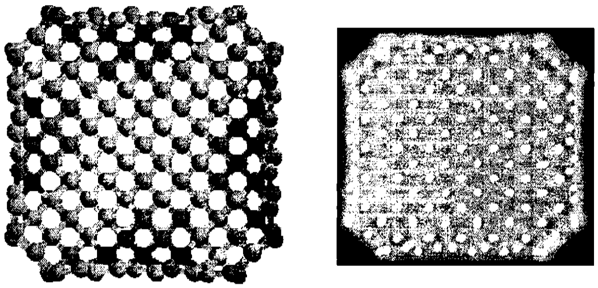

Figure 3-5: 2×1 wire, with cross-section ≈ 2.4nm: same conventions as Figure 3-4.

Structure	δF_{tc}	δF_{at}		δE_{tc}	δE_{at}
2×1	13.1%	2.86%		-11.6%	1.78%
$c(2 \times 2)$	4.91%	1.79%		-4.68%	2.02%

Table 3.1: Comparison of errors between the traditional continuum theory and the atomic moduli description when predicting flexural response through Eqs (3.15) and (3.13) (first and second columns, respectively) and when inferring extensional response from flexural response through Eqs. (3.22) and (3.18) (third and fourth columns, respectively).

The ultimate use of atomic level moduli is to understand mechanical response. Table 3.1 compares the errors from both continuum theory and the use of atomic-level moduli in predicting mechanical response for the two wires under consideration in this section. The quantities compared exactly parallel those of the previous section. The first two columns of the table consider prediction of flexural response from continuum theory and our atomic moduli, respectively, and the second two columns consider prediction of extensional response from flexural response using either the traditional continuum relation or our new relation, respectively. The table shows that the new relations, Eqs. (3.13) and (3.18) are again very accurate. The table also shows that these predictions are superior to the corresponding continuum results, Eqs. (3.15) and (3.22), respectively.

Interestingly, the continuum predictions for the $c(2 \times 2)$ wire are fairly reliable. The atomic moduli provide an avenue for understanding this as well. Fluctuations in the moduli in the $c(2 \times 2)$ wires are localized and hence average out over regions of extent comparable to the decay of the force-constant matrix. Moreover, in this particular case they tend to average to values close to that expected of the bulk. Without meaningful fluctuations on the length scales of the decay of the force-constant matrix, we expect continuum theory to perform well for this wire. In contrast, the 2×1 wire exhibits much more systematic variations in the moduli. The outermost surface atoms have a consistent and significantly reduced modulus, and there is also a clear significant and systematic variation in the moduli throughout the cross-section of the wire. Because this second wire does exhibit meaningful fluctuation over distances comparable to the decay range of the force constant matrix, we expect traditional continuum relations to give particularly poor results, underscoring the importance of the local atomic-level moduli description.

3.9 Conclusions

We have presented the first definition of atomic-level elastic moduli for nanoscale systems which are defined in terms of physical observables, correctly sum to give the exact overall elastic response and depend only on the local environment of each atom. Although these moduli are not necessarily uniquely defined, their sum over regions of extent comparable to the range of the force constant matrix is physically meaningful and may be used to make accurate predictions of mechanical response. The moduli resulting from our formulation transfer to different modes of strain and correctly account for elastic fluctuations on the nanoscale. They also lead to a quantitative understanding of when traditional continuum relations breakdown and how to properly correct them properly. Specifically, we demonstrated a more accurate method for relating extensional and flexural properties. These moduli provide a clear and natural method for distinguishing *mechanically* between "surface" atoms and "bulk" atoms and give insight into the correlation between the local mechanical response and the underlying electronic structure. Finally, these moduli allow the identification of which atomic arrangements lead to more pliant or stiffer response opening the possibility of their use as a tool to aid in the rational design of nanostructures with specific mechanical properties.

Chapter 4

Accurate calculations of the Peierls stress in small periodic cells

Long, low-mobility [111]-screw dislocations control low temperature plastic behavior in bcc metals. Unlike their fcc counter parts, bcc metals violate Schmid behavior and have many active slip planes. The microscopic origins of such behavior is crucial in the understanding of their plastic behavior. Therefore detailed and accurate first principle calculations are invaluable.

The Peierls stress, the zero temperature limit of the critical stress for slip, has been calculated in a variety of ways using various types of boundary conditions [102, 82, 65, 111, 93, 113, 16, 76]. These calculations, in general, rely on empirical potentials to simulate various configurations and incorporate a relatively large number of atoms. In general three types of boundary conditions are used, fixed cylindrical boundary conditions [82, 65, 111, 93], lattice greens functions [75, 113, 76] or periodic boundary conditions [102, 16]. For these approaches a large number of atoms is generally taken in order to minimize any artificial effects the boundary conditions may impose. Generally, this number is too large to be suited for *ab initio* calculations, even on the fastest and largest super-computers. Applying corrections to these effects is therefore important in order to have a reliable *ab initio* calculation.

The simplest approach is to use fixed cylindrical boundary conditions. However, care must be taken due to the mismatch of the boundary with the dislocation, particularly when the dislocation moves. This mismatch can be minimized by performing calculations in very large systems, effectively extrapolating to the limit of infinite cylinder size. The size of the system needed to extract accurate values can be greatly reduced by applying leading order corrections due to the mismatch in the boundary [82]. However, even with these corrections, accurate calculations can generally be made only for a cylinder with a radius of $\sim 30\AA$ or greater, which corresponds to ~700 atoms when using periodic boundary conditions along the dislocation line. Such fixed cylindrical boundary conditions are generally ill-suited for an *ab initio* calculation due to both this large number of atoms and the artificial effects of the free surface at the boundary on the electrons. An alternative approach to account for boundary effects, and thereby reduce the size of the system needed for accurate calculation, is to use lattice greens function techniques [113, 76, 75]. This technique, although quite elegant, still faces the issue of free surface effects when applied to first principles quantum mechanical calculations. In Section 5.1 we shall detail such problems.

Periodic boundary conditions are in general the most natural and straight forward way to calculate the Peierls stress in a density functional theory calculation. In periodic boundary conditions one is forced to have a net zero Burgers vector per unit cell. This is generally accomplished by using either a dipole or quadrupole array of dislocations [78, 12, 53]. Peierls stress calculations have been done in periodic boundary conditions using empirical potentials, however, to avoid dislocation-dislocation interactions, generally requires the use of unit cells [16] which would be impracticable for *ab initio* calculations. Wang *et al.*[102] have introduced a promising method for use in small, periodic cells, but this approach requires the decomposition of the total energy into individual atomic contributions, which while feasible for inter-atomic potential approaches, is not well-defined in quantum mechanical calculations.

In this chapter it is shown how an accurate Peierls stress can be obtained in very small periodic cells. It is shown how leading order effects, due to the array of closely packed dislocations, can be accurately accounted. It is further shown how an accurate Peierls stress can be obtained by simply applying a pure shear to the system and minimizing the energy. This is a tremendous advantage in *ab initio* calculations as it minimizes the number of atomic configurations which need be explored. As an application of these ideas, we focus specifically on the calculation of the Peierls stress in bcc tantalum for a [111]-screw dislocation in which the maximum resolved shear stress is along a {110}. This is among the most relevant geometries in understanding the plastic response of this material.

The chapter is organized as follows. Section 4.1 presents the results of Peierls stress calculations in very large cylindrical cells, as a reference against which we shall compare our new approach. Section 4.2 presents the results of calculations using periodic boundary conditions and underscores the problems that arise. Section 4.3 shows how to overcome these problems, and, finally, Section 4.4 presents several techniques for accelerating the calculation. Finally, Section 4.5 concludes the chapter.

4.1 Reference Calculations

All calculations presented throughout this chapter employ a quantum-based, embedded atom force field (qEAMFF) developed in [89]. To provide the reference value of the Peierls stress for our calculations within periodic boundary conditions, we first perform calculations for isolated dislocations in a cylindrical geometry with fixed boundary conditions.

To form the dislocation, we proceed as follows. First, we define coordinates for our calculations as follows: the x-axis lies along the $[1\bar{1}0]$ direction, the y lies along the $[11\bar{2}]$, and the z lies along the [111]. A cylinder with radius $R2$ of Ta is then taken (Figure 4-1) which has two regions, a fixed region and a relaxation region. In the relaxation region ($r < R1$), where r is the radial distance from the center, the atoms are allowed to relax in response to their interatomic forces. The atoms in the fixed region ($R1 < r < R2$) are held fixed to their positions according to the solution of anisotropic elasticity theory. Finally, periodic boundary conditions (with period of one Burger's vector) are employed along the direction of the dislocation. Thus, these calculations consider only straight, infinite dislocations. A [111]-screw dislocation

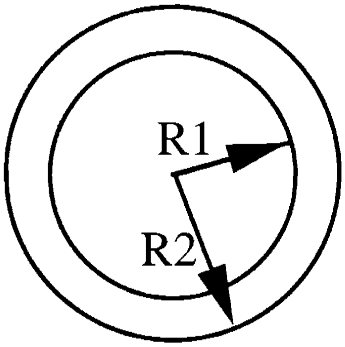

Figure 4-1: Peierls stress calculation within cylindrical boundary conditions: atoms whose distance from the center is less than $R1$ are relaxed under inter-atomic potential forces, while those in the region between $R1$ and $R2$ are held fixed to the anisotropic elasticity theory solution.

then is obtained by displacing all atoms in the cylinder according to the solution of anisotropic elasticity theory [90, 35] and then optimizing the positions of the atoms in the relaxation region.

To calculate the Peierls stress, we then apply a strain to the system which ensures that the resulting stress has only one component, σ_{xz}, which generates a force on the dislocation line in the $[11\bar{2}]$ direction [38]. We then optimize the locations of the atoms in the relaxation region subject to this external strain. Figure 4-2 shows the resulting dislocation structure in a large cyllinder ($R1 \approx 120\text{Å}$) for a series of different strains using a differential displacement (DD) map [100]. In these maps, the circles represent columns of atoms viewed along the [111] direction. The arrows indicates the change in relative displacement that neighboring atomic columns make, relative to the bulk, due to the presence of the dislocation. The lengths of the arrows are normalized so that a displacement of 1/3 of a Burgers vector corresponds to an arrow of full length. The first panel (a) shows the ground-state structure of the dislocation at zero stress. The center of the dislocation is located at a diamond encased in triad of arrows. Going around this triad makes three displacements of one-third of a Burgers vector for a net displacement of one full Burgers vector relative to the bulk. The ground state structure of the core is seen to break the symmetry of the lattice by extending outward along three $\{110\}$ planes. This "degenerate split core" is consistent with molecular

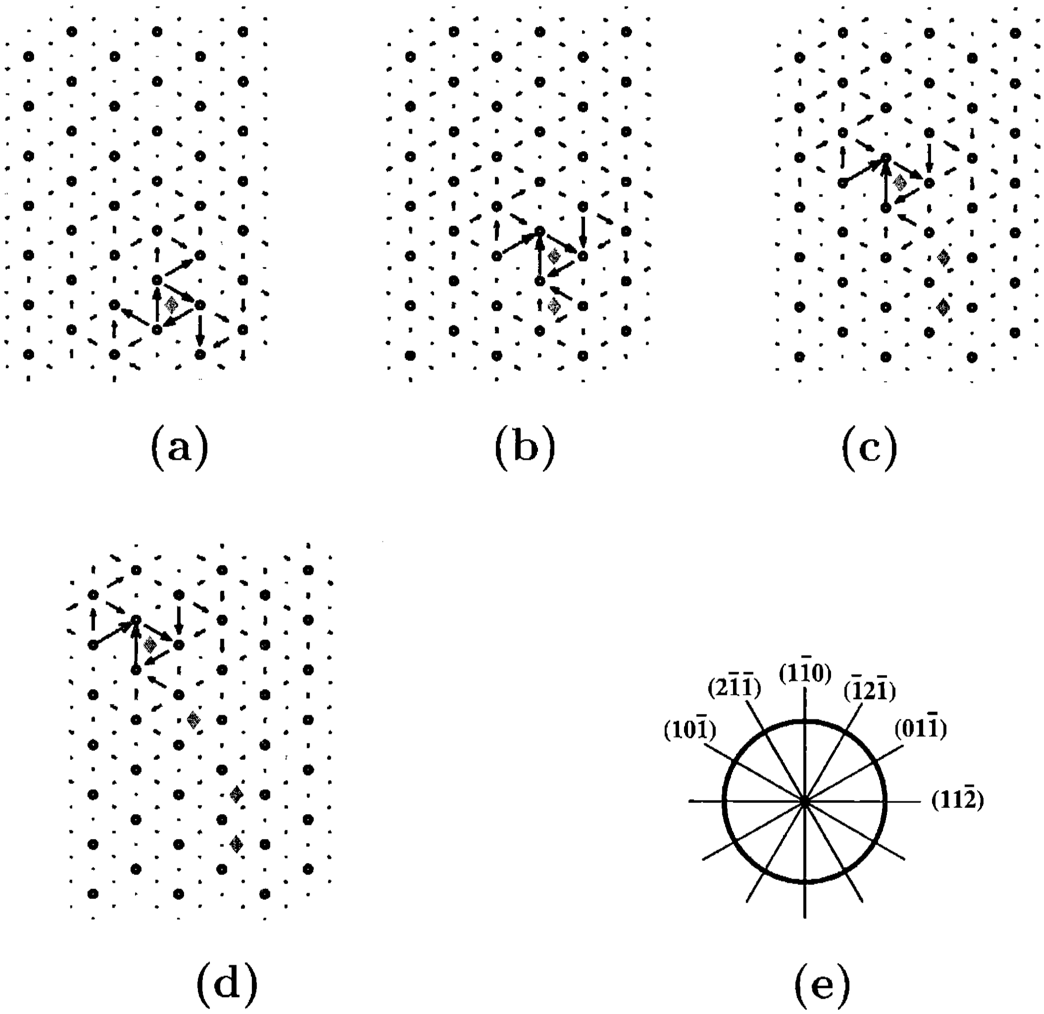

Figure 4-2: Differential displacement (DD) maps of a [111] screw dislocation at increasing stress computed within cylindrical boundary conditions: **a**) zero applied stress, **b**) initial jump along $(1\bar{1}0)$ at a stress ≥ 0.74 Gpa ($P1$), **c**) second jump, along $(2\bar{1}\bar{1})$ at a stress ≥ 0.91 GPa ($P2$), **d**) subsequent jump along $(2\bar{1}\bar{1})$, **e**) orientation of $\{110\}$ and $\{112\}$ planes.

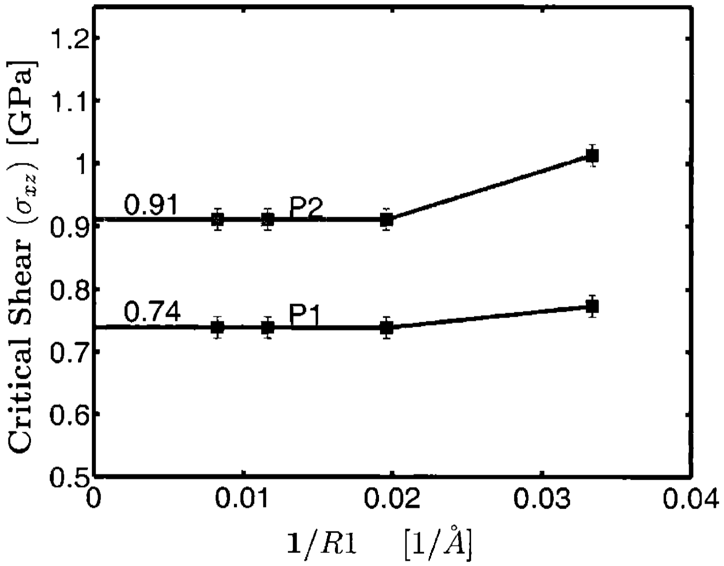

Figure 4-3: Convergence of P1 and P2 as a function of $1/R1$, for cylinders ranging from $R1 = 30Å$ to $R1 = 120Å$.

dynamic results, using periodic boundary conditions, found in reference [102] when using the same interatomic potential.

As the strain is applied to the ground state structure (Figures 4-2b-d), the dislocation feels force along the $(1\bar{1}0)$-plane. As the applied strain obtains a critical value, the dislocation center moves one lattice spacing along the $(1\bar{1}0)$-plane (Figure 4-2b). As the strain is increased further, the dislocation then glides along the $(2\bar{1}\bar{1})$ (Figures 4-2 c,d) in two steps, first along $(10\bar{1})$ and then spontaneously along $(1\bar{1}0)$. There are consequentially two Peierls barriers that the dislocation must overcome, the first along $(1\bar{1}0)$ and the second along $(10\bar{1})$. This leaves some ambiguity for the definition of the Peierls stress. Different authors have used different definitions [102, 111, 93, 113]. For clarity we will consider the value of the σ_{xz} stress for the first jump (Figure 4-2a-b) as the first Peierls stress ($P1$) and the value of the σ_{xz} stress for the second jump (Figure 4-2b-c) as the second Peierls stress ($P2$).

To extract the limit of these critical stresses for an isolated dislocation in an infinite crystal, we have repeated the above calculations in cylinders of various sizes ranging from $R1 = 30Å$ to $R1 = 120Å$ and extracted the Peierls stress as a function of radius. Figure 4-3 summarizes our results. In the limit, we find values of 0.74 GPa and 0.91 GPa for $P1$ and $P2$, respectively.

As a consistency check that we indeed expect finite-size effects to be small for our largest cylinders, one can employ the method of Shenoy and Phillips [82]. This methods estimates the unaccounted restoring stress that the boundary applies to a displaced dislocation to be

$$\frac{K_s b}{2\pi} A \frac{d}{R^2},$$

where $K_s = (S_{11}/(S_{11}S_{44} - S_{15}^2))^{1/2}$ in terms of the modified elastic compliances S_{ij} [90], b is the Burgers vector, d is the distance the dislocation has moved from the center of the cylinder, R is the radius of the cylinder, and A is a dimensionless constant that can be calculated through elasticity theory or computationally. In our case, $A \approx 2$, $K_s = 68$GPa and $b = 2.9\mathring{A}$. Finally, for $P1$ we have $d \approx .1\mathring{A}$ and for $P2$ we have $d \approx 2.7\mathring{A}$. For our largest cylinder ($R1 = 120\mathring{A}$), we calculate a restoring stress of 0.0004GPa and 0.012GPa, respectively. Both values are quite small, well within the uncertainties in Figure 4-3.

4.2 Periodic Boundary Conditions

In periodic boundary conditions, the unit cell must contain a net zero Burgers vector. In practice this is generally accomplished through the use of either a dipolar or quadrupolar array of dislocations [78, 12, 53]. Our calculations employ a quadrupole array, which has been shown to be the more appropriate choice for screw-dislocations [53]. Figure 5-3 illustrates a cell containing 270 atoms.

As our first attempt to calculate the Peierls stress in periodic boundary conditions, we take a quadrupole array with lattice vectors fixed at the values corresponding to the perfect bulk material, that is the appropriate lattice vectors prior the insertion of dislocations. Below, we refer to this choice as "unrelaxed" lattice vectors, as they generally do not correspond to the lattice vectors of an unstrained quadrupole array.

To extract an estimate of the Peierls stress, we then follow a procedure analogous to that in Section 4.1, applying strain until the dislocations move. Here, rather than

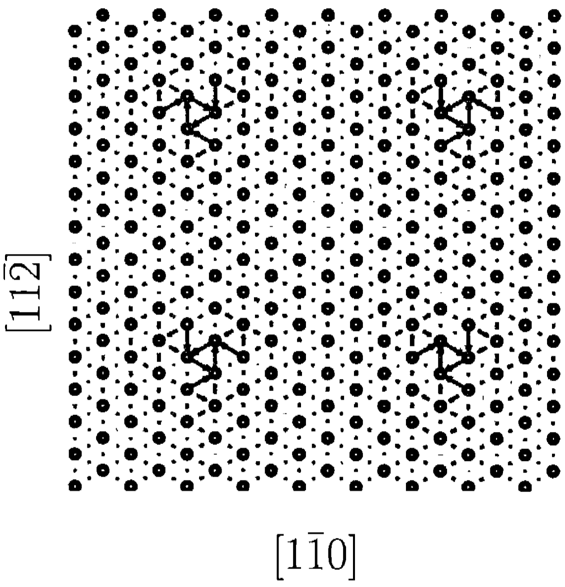

Figure 4-4: Dislocation displacement (DD) map of a quadrupole dislocation array within a 270 atom cell with periodic boundary conditions. The cell may be reduced to 135 atoms with appropriate choice of lattice vectors.

applying the strain to the fixed region ($R1 < r < R2$), we strain the *unrelaxed* lattice vectors. Then, we then compute the critical stress from the strain through the elastic constant matrix,

$$\sigma = \mathbf{C} \cdot \epsilon, \tag{4.1}$$

where σ is a column vector of the stresses, ϵ is the applied strain vector, and $\mathbf{C}$ is the elastic constant matrix, *assumed* to equal that of the bulk material. The advantage of this approach is that it requires exploration of a minimal number of configurations and bulk lattice and elastic constants are relatively easy to obtain from first principles calculations. The disadvantage of this approach is that its underlying assumptions cast doubt of the accuracy of the results for unit cells of modest size.

Figure 4-5 explores the convergence of this approach with increasing cell size for calculation of the first Peierls stress ($P1$). The two smallest cells contain 90 atoms ($\sim 2.9\AA \times 24\AA \times 24\AA$) and 270 atoms ($\sim 2.9\AA \times 42\AA \times 42\AA$) (or 45 and 135 atoms, if symmetry is exploited), and are the only cells convenient for detailed *ab initio* studies.

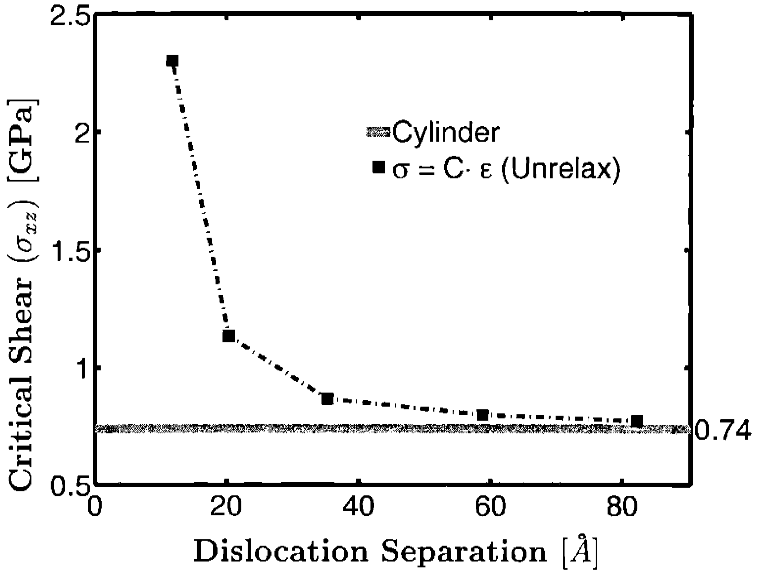

Figure 4-5: Convergence of P1 calculated within periodic boundary conditions using unrelaxed lattice vectors and bulk elastic constants: Peierls stress calculated using Eq. 4.1 (squares), limit exacted from Figure 4-3 (solid line with width indicating numerical uncertainty). Uncertainties in the periodic calculations are smaller than the square symbols.

The results in these cells, however, are extremely poor, with errors of 200% and 53%, respectively. Thus, great care must be taken when working with such small cells and a method is needed to correct for these finite-size effects.

4.3 Corrections

The preceding calculations make two major assumptions: (1) that the quadrupole array of dislocations does not change the elastic constant matrix from that of bulk material, and (2) that the use of unrelaxed lattice vectors is appropriate. To explore the impact of these assumptions, we repeat the above calculations while using both the relaxed lattice vectors and elastic constants of the quadrupolar array.

Numerical calculations show that the symmetry of the elastic constant matrix of the quadrupolar array ($\mathbf{C}'$) is the same as that of the bulk, although the individual components may differ. In particular, the stress-strain relation takes the form

$$\sigma \;=\; \mathbf{C}' \cdot \epsilon \tag{4.2}$$

$$\begin{bmatrix} \sigma_{xx} \\ \sigma_{yy} \\ \sigma_{zz} \\ \sigma_{yz} \\ \sigma_{xz} \\ \sigma_{xy} \end{bmatrix} = \begin{bmatrix} (4 \times 4) & 0 \\ 0 & (2 \times 2) \end{bmatrix} \cdot \begin{bmatrix} \epsilon_{xx} \\ \epsilon_{yy} \\ \epsilon_{zz} \\ \epsilon_{yz} \\ \epsilon_{xz} \\ \epsilon_{xy} \end{bmatrix} \tag{4.3}$$

In this equation, the lower 2 × 2 sub-block couples the σ_{xz} and σ_{xy} stresses only to the corresponding strains, while the upper 4 × 4 block couples the $\sigma_{xx}, \sigma_{yy}, \sigma_{zz}$ and σ_{yz} stresses only to their corresponding strains. Note, therefore, that for the present Peierls stress calculations only the lower 2 × 2 block is relevant.

Figure 4-6 shows the results (diamonds in the figure) of the extraction of the Peierls stress when using relaxed lattice vectors and the elastic constants for the quadrupole. The figure shows that the Peierls stress now converges much more quickly with cell size. (The figure does not include results for the smallest cell, which proved unstable to the relaxation of the lattice vectors.) For the smallest stable cell (135 atoms including symmetry), the error is reduced from 53% to only 18%, indicating the possibility of extracting reasonable results from cells of size suited to *ab initio* calculations. Although results for reasonably sized cells are accurate, this approach, however, is not necessarily well suited for *ab initio* calculations because relaxation of the lattice vectors and the calculation of the elastic constant matrix requires the exploration of many new atomic configurations.

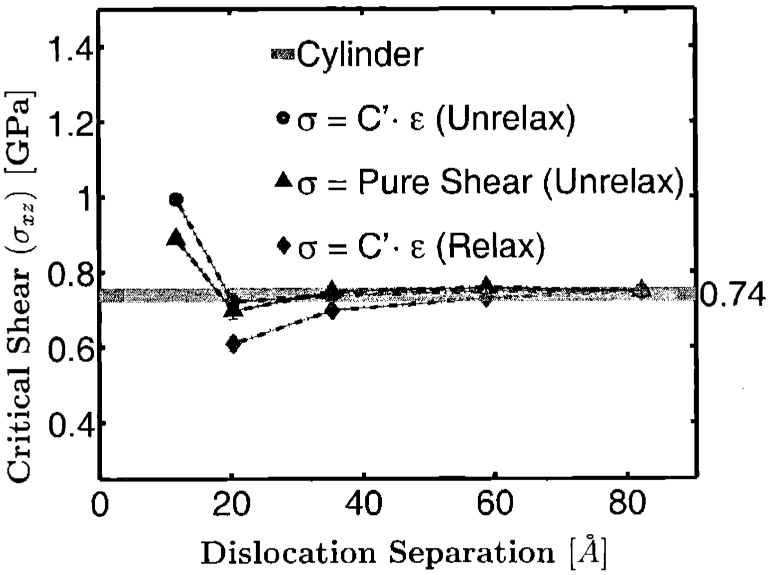

Figure 4-6: Convergence of P1 calculated within periodic boundary conditions: using relaxed lattice vectors and quadrupolar elastic constants (diamonds), using unrelaxed lattice vectors and quadrupolar elastic constants (circles), using unrelaxed lattice vectors, pure shear and elastic constants extracted during the calculation (triangles), asymptotic result extracted from cylindrical boundary conditions (horizontal line). Error bars associated with quadrupolar array are generally smaller than the associated icons.

4.4 Accurate and Efficient Peierls Stress Calculation

Having found an accurate approach, we now explore how to minimize that calculations associated with the above corrections. We begin by considering the necessity of relaxing the lattice vectors and then consider computation of the *relevant* components of the elastic constant matrix $\mathbf{C}'$.

4.4.1 Benefit of fixed lattice vectors

Working with unrelaxed lattice vectors generates spurious strains in the unit cell. The question is whether these strains create spurious stresses which confound the extraction of the Peierls stress. The elastic force which any such stresses would generate on the dislocation take the form [38]:

$$\mathbf{F}_L = \mathbf{b} \cdot \sigma \times \eta. \tag{4.4}$$

Here, $\mathbf{F}_L$ is the force per unit length on the dislocation, $\mathbf{b}$ is the Burgers vector, σ is the stress tensor written as a *matrix*, and η is the sense vector, the direction along which the dislocation runs. For a [111]-screw dislocation $\mathbf{b}$ and η both lie along the $z-$axis, and, therefore, only two components of stress can generate a force on the dislocation, σ_{xz} and σ_{yz}, and confound the extraction of the Peierls stress. We now consider whether the strains associated with the unrelaxed lattice vectors can generate such stresses. We distinguish two types of strain, dilation and shear.

The presence of the quadrupolar array tends to dilate the unit cell in the (111) plane. Due to symmetry, this dilation tends to be uniform, as we have confirmed by direct numerical calculation on the unit cells. The above form of the elastic constant matrix $\mathbf{C}'$ prevents such dilation from generating any σ_{xz} component. The second confounding component σ_{yz} would also vanish were the 4×4 subblock of the elastic

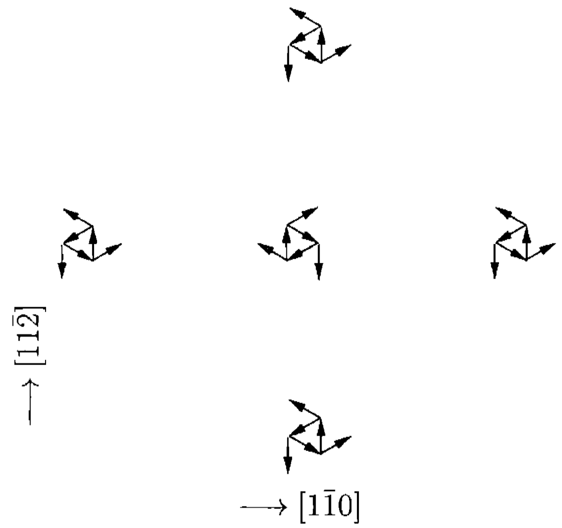

Figure 4-7: The first nearest neighbors cannot generate any elastic force on the center dislocation, since they are equally spaced. From the core asymmetry there can be a core-core force in only in the $[1\bar{1}0]$. Note that these symmetry arguments works for higher order neighbors too.

constant matrix to have precisely the same symmetry as that of the bulk. Numerically, we find that that this is almost the case, and that the dilation contribution to σ_{yz} ranges from 0.02% (in our largest cell) to only 4% (in the 135 atom cell) of the stress experienced in the *unrelaxed* cell. The diagonal components of strain ϵ_{ii} do not significantly affect the extraction of the Peierls stress, and therefore need not be relaxed to extract meaningful Peierls stresses.

Turning to shear strains, the equal spacing of the dislocation array leads to zero shear within linear elasticity theory. From symmetry, however, core-core interaction (non-elastic) can generate a force in the $[1\bar{1}0]$-direction only, Figure 4-7, which results in one non-zero component of strain, ϵ_{yz}. From direct calculations it is shown that this is in fact the only non-zero component of shear strain. Relaxing this component of strain, therefore, creates a artificial material environment, different from what isolated dislocations would experience. To more quickly approach the limit of isolated dislocations, one should therefore *not* relax this component of the strain. This advantage of using of unrelaxed lattice vectors is well known and commonly exploited in the materials literature in the study of *two*-dimensional defects such as grain boundaries or surfaces[6, 103]. We therefore expect to be able to extract accurate Peierls stresses without the need for relaxing either off-diagonal or diagonal components of strain.

Figure 4-6 shows the results (circles in the figure) of extracting the Peierls stress when using *unrelaxed* lattice vectors, but while still computing the stresses with the appropriate elastic constant matrix $\mathbf{C}'$. The results converge even more quickly than those obtained by relaxing the lattice vectors, thus supporting our analysis. Therefore, extremely good results (already within 2% in the 135 atom cell) can be obtained by not relaxing the lattice vectors. This not only produces results of far superior quality, it also reduces the computational effort.

4.4.2 Extraction of elastic constants

The results of Section 4.4.1, while quite impressive, still require calculation of the elastic constant matrix $\mathbf{C}'$ of the quadrupolar array. Significant savings can be gained with the simple realization that only the 2×2 sub-block of the elastic constant matrix enters calculation of $P1$ and $P2$ through Eq. 4.3. Moreover, within linear elasticity theory, these components can be extracted equally well at the relaxed or unrelaxed lattice vectors, thereby again mitigating the need for relaxation of the lattice vectors.

Not all of the components of the 2×2 sub-block,

$$\mathbf{C'}_2 \equiv \begin{bmatrix} C'_{44} & -C'_{16} \\ -C'_{16} & C'_{55} \end{bmatrix}, \tag{4.5}$$

need be computed independently.

To see this, consider the application of a pure, shear strain ϵ_{xz} to the system. As a result of the symmetry of $\mathbf{C}'$, this generates only two components of stress, σ_{xz} and σ_{xy}. From equation 4.4, however, σ_{xy} does not generate any forces on the dislocation and thus, within linear elasticity, does not effect our calculation of the Peierls stress. The remaining stress, whose critical value is the Peierls stress, can be computed from just one component of $\mathbf{C'}_2$,

$$\sigma_{xz} = C'_{44}\epsilon_{xz}. \tag{4.6}$$

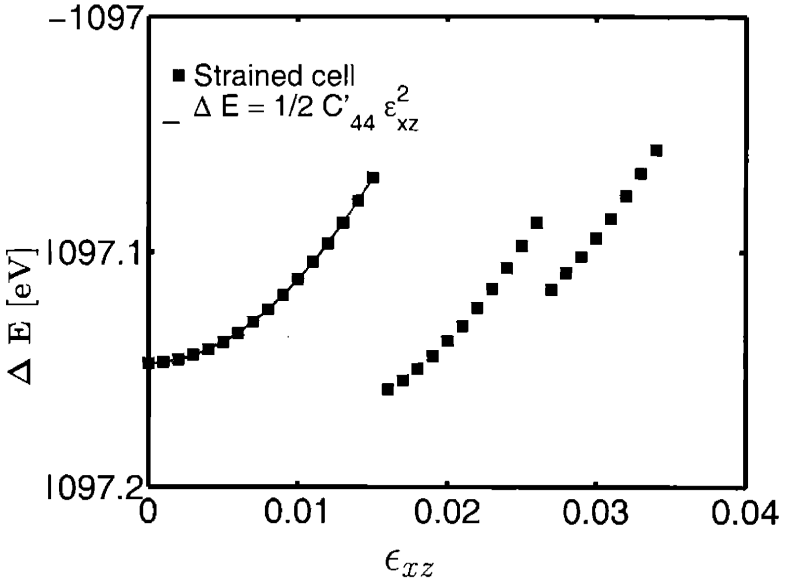

Figure 4-8: Energy of a 42Å × 42Å × 2.9Å cell (270 atoms) plotted as a function of applied pure shear strain ϵ_{xz}: direct calculations (squares), quadratic fit (curve).

Finally, we note that this pre-factor can be extracted without any additional calculation. Figure 5-4 shows the total energy of the quadrupole array plotted as a function of strain during the extraction of the critical Peierls stress. Prior to the first dislocation glide event at $\epsilon_{xz} \approx 0.015$, the energy increases quadratically according to

$$\Delta E = \frac{1}{2} C'_{44} \epsilon^2_{xz}, \tag{4.7}$$

which contains precisely the same pre-factor as in Eq. 4.6.

Figure 4-6 shows the result (triangles in the figure) of the extraction of the Peierls stress from the application of a pure, shear strain ϵ_{xz} to the *unrelaxed* lattice vecotrs and extracting the relevant elastic constant from the curvature of the energy prior to the glide events. The results are of nearly the same quality as working with unrelaxed lattice vectors and using the full elastic constant matrix $\mathbf{C}'$.

Finally, we note that although σ_{xy} does not generate an elastic force on the dislocation, through equation (4.4), it can affect the value of the Peierls stress, as was shown by Duesbery [24]. For systems in which the ratio of C'_{44}/C'_{16} is small such an effect should be relatively small. In all cells used the ratio C'_{44}/C'_{16} varies from $\approx 1/90$, for bulk, to $\approx 1/5$, for the smallest quadrupole cell. It can be seen from Fig. 4-6 that this effect is indeed small and the value of the Peirls stress is quite accurate. In Section 5.3 we shall show more explicitly that such an effect is minimal for the cases of interest in this thesis.

4.4.3 Second Peierls stress: $P2$

Figure 4-9 shows our preliminary results for the the extraction of the second Peierls stress $P2$. These results are complicated by the fact that after the first transition $P1$, the quadrupole array is now distorted and no longer a perfect quadrupole, thereby generating non-negligible dislocation-dislocation forces and further modifying the elastic constant matrix of the cell. As a possible correction to this effect, we are presently exploring moving the distorted cores back to their original quadrupole locations before further increasing the stress. Nonetheless, we find that significant improvements can be made by using the elastic constant matrix of a perfect quadrupole array and ignoring the dislocation-dislocation interactions. Finally, results for pure shear calculations are quite encouraging.

4.5 Conclusion

This chapter present an accurate and effective way to calculate the {110} Peierls stress in a [111] screw dislocation in a bcc material. The results show that accurate results can be obtained even for the smallest cells while using unrelaxed lattice vectors and extracting the elastic constants directly from the calculations. The method most importantly appears to make *ab initio* calculations of Peierls stresses viable in periodic boundary conditions for the first time.

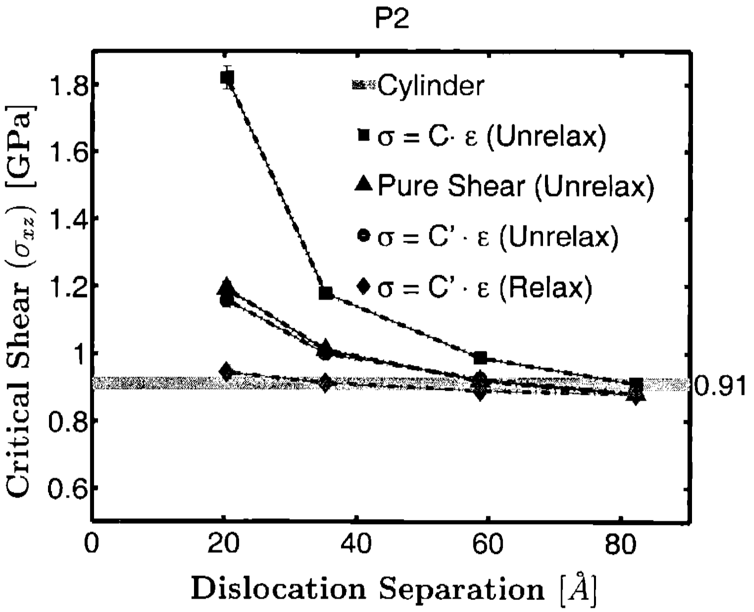

Figure 4-9: Convergence of P2 calculated within periodic boundary conditions: using unrelaxed lattice vectors and bulk elastic constants (squares), using relaxed lattice vectors and quadrupolar elastic constants (diamonds), using unrelaxed lattice vectors and quadrupolar elastic constants (circles), using unrelaxed lattice vectors, pure shear and elastic constants extracted during the calculation (triangles), asymptotic result extracted from cylindrical boundary conditions (horizontal line).

Chapter 5

Ab initio and finite-temperature molecular dynamics studies of lattice resistance in tantalum

The study of the plasticity of crystalline materials is a rich many-body problem involving physics on multiple length scales, with many remaining unexplained mysteries. The plasticity of bcc metals, for instance, is particularly challenging. Unlike their fcc and hcp counterparts, the bcc metals exhibit many active slip planes, have a strong temperature dependence in their plasticity and violate the simple empirical Schmid law [80]. Moreover, theoretical calculations of the most basic question in plasticity, the stress needed to induce yield at low temperature in a pure sample, differ from experimental extrapolations by over a factor of two [25]. The purpose of this work is to provide needed insight into this discrepancy.

Ultimately, it is the physics of the $\langle 111 \rangle$ screw dislocation defect which controls the low-temperature plasticity of bcc materials [100, 25]. The Peierls stress, the yield stress at which these dislocations first begin to move spontaneously, is difficult to compare directly with experiment. Whereas most computational work on the Peierls stress measures the stress to move an isolated, infinitely straight dislocation at zero temperature [100, 24, 81, 102, 76, 107, 108, 113, 111, 65, 110, 93, 44], experiments measure the Peierls stress at a finite temperature in systems with many interacting, curved dislocations and in media with defects and surfaces. As an example of the present challenges which the literature faces, using model generalized pseudopotential theory (MGPT) [110], Yang *et. al.*[113] predict for the T=0 Peierls stress a value 2.5 times greater than experimental extrapolations [94]. Because such potentials are not based upon first principles, it is impossible to determine *a priori* whether this discrepancy is due to the interatomic potential, the environmental complexities discussed above, or to a flaw in our understanding of the relation between the Peierls stress and the experiments.

As it is a daunting experimental task [84] to observe properties of a single dislocation locked deep in the heart of a material, accurate theoretical calculations of such systems is essential. Nearly all theoretical calculations to date, concerning such dislocations, have relied upon empirical potentials [100, 24, 81, 102, 82, 65, 111, 110, 44, 113, 76, 16, 93]. Given the empirical nature of such calculations, the complex directional bonding properties of bcc materials, and the lack of direct comparison with experiments for validation, first principles *ab initio* calculations of dislocations in such systems are clearly needed. Ismail-Beigi and Arias [42] were the first to show that density functional theory calculations were crucial in understanding the fundamental properties of the $\langle 111 \rangle$ screw dislocation core structure in bcc molybdenum and tantalum. Until that work, most computational studies based on empirical potentials [100, 24, 76, 110, 102, 111, 65, 81], supported the idea that the dislocation core breaks symmetry, with two energetically equivalent ground state structures which spread outward along two different equivalent sets of three $\{110\}$ planes [100], similar to the concept originally proposed by Hirsch [37, 61]. Until the availability of the *ab initio* calculations, the prevailing view of the violation of the Schmid law in the bcc metals was based upon this structure [100]. Ismail-Beigi and Arias [42], in contrast, showed that for both molybdenum and tantalum the ground-state structure within density functional theory was a non-degenerate symmetric core, strongly supporting the work of Suzuki and Takeuchi [92, 93, 49] which first suggested that it is the Peierls potential itself that controls the lattice resistance and not the details of the core structure. To help resolve the discrepancy between theoretical and experimental

Peierls stresses, the work below provides a reliable *ab initio* prediction of the Peierls stress in bcc tantalum which is free of the unrealistic electronic boundary conditions employed in the only other *ab initio* prediction of the Peierls stress [107, 108].

Here, we show that the Peierls stress, calculated within density function theory, is over a factor of *five* larger than expected from extrapolation of experimental results [94]. This supports the view that the discrepancy between the experimental and computational predictions are largely due to the aforementioned environmental complexities, to a flaw in relating the experimental data to the Peierls stress, or to a combination of both.

To further explore possible physical effects leading to this discrepancy, we study the extrapolation of experimental data to determine the zero-temperature Peierls stress. Such extrapolations generally employ fits from mesoscopic or thermodynamics/kinetic models [94, 51, 22, 21]. However, it has not been established that such models can accurately describe the lowest temperature regime correctly, placing doubt on the quality of these extrapolations. To address this issue, the work below also provides the first temperature- and orientation- dependent study of the Peierls stress in a bcc metal. We moreover show that extrapolation of our finite temperature results using a current fitting model leads to an underestimation of the zero-temperature Peierls stress. This underscores the difficulty in extrapolating the experimental data accurately but accounts only for the observed discrepancy.

Section 5.1 of this chapter reviews the various techniques in use for calculation of the Peierls stress in the context of efficacy for application to *ab initio* calculations. Section 5.2 gives the first calculation of the temperature and orientation dependent Peierls stress in a bcc material. Section 5.3 describes our technique for obtaining Peierls stresses within small unit cells with periodic boundary conditions. Finally, Section 5.4 presents our *ab initio* prediction for the Peierls stress and compares and contrasts it to currently available experimental and computational values.

5.1 Boundary Conditions

The fundamental distinction among theoretical approaches to calculation of the Peierls stress is the choice of boundary condition. The literature describes three types of boundary conditions: cylindrical boundary conditions [100, 81, 82, 110, 111, 93, 44, 24], Greens function (or "flexible") boundary conditions [85, 75, 113, 76, 100, 107, 108], and periodic boundary conditions [81, 102, 16]. We now briefly review each with emphasis on the unique challenges of *ab initio* electronic structure calculations.

5.1.1 Cylindrical Boundary Conditions

In the practice of cylindrical boundary conditions, anisotropic elasticity theory [38, 90, 35] is used to generate a dislocation in the center of a cylinder. The cylinder is then separated into *inner* and *outer* regions. The atoms in the outer region are held fixed to the solution of anisotropic elasticity theory while the atoms in the inner region relax under the inter-atomic forces. To calculate the Peierls stress, a stress is applied to the system until the dislocation moves.

This approach suffers numerous draw backs when applied to density functional theory. To avoid surface effects and to properly account for the non-linear nature of the dislocation, such cylinders generally have to be quite large. First, even the outer cylinder is of finite size and therefore the outer region must be sufficiently large enough so that forces generated by it onto the inner region are equivalent to those generated from an infinite continuum. The inner region also must be sufficiently large to mitigate two effects. The inner region must be large enough so that linear elasticity theory represents well the forces which it imposes on the outer region. The inner region also must be large enough so that motion of the dislocation is not adversely affected by the fixed outer region, which is a concern because the fixed outer region represents the displacement field when a dislocation is at its center and therefore generates a extraneous force which tends to prevent motion of the dislocation [82]. When using simple, inter-atomic potentials, the use of large cylinders mitigates all of these effects. However, this approach is not viable for density functional calculations with their extreme computational demands.

This approach, moreover, is particularly ill-suited for electronic structure calculations because the artificial surface at the outside of the outer region, being far different from the bulk, give rise to strong scattering of the electrons far different than would an infinite continuum. This is particularly problematic for metals, because the single-particle density matrix, which quantifies the effects of this scattering on the inter-atomic forces, decays only algebraically in metals [41]. The following subsection demonstrates that the boundary regions should be quite large in order for these surface effects not to result in large fictitious forces in the active region of the calculation.

5.1.2 Greens Function Boundary Conditions

The use of Greens function, or flexible, boundary conditions [85, 75, 100], is an effective way to reduce the size of the simulation cell. This approach also employs a cylindrical geometry. However, rather than the "inner" and "outer" atomistic regions of the cylindrical boundary approach, the Greens function approach employs three interatomic regions: an inner "core" region containing the center of the dislocation, an intermediate "buffer" region, and an outermost "continuum-response" region. With *proper* implementation, the outer and inner regions couple only indirectly through the response of the buffer region.

In this method, all three regions respond to the presence of a dislocation; however the response of each region is treated differently through a number of steps. Initially, all regions are displaced by the solution to anisotropic elasticity theory. Each iteration then begins by relaxing the atoms in the core region according to the forces which they experience, as computed from either an inter-atomic potential or an *ab initio* method. The forces generated from the mismatch between the outer and inner regions, which the cylindrical approach above ignores, are then relieved by moving the atoms of *all three regions* according to the elastic Greens function, leaving only the nonlinear effects from the core region unaccounted. The next iteration then begins by relaxing these forces as described above. Iterations proceed until until the forces in the core and buffer region are negligible.

What distinguishes this approach from simple cylindrical boundary conditions is that the continuum region, via the Greens function response, is allowed to respond to the motion of the dislocation and to the elastic response generated by the core region as the dislocation moves. So long as the continuum response region (a) accurately represents the structure induced by the presence of the dislocation and (b) is sufficiently wide to properly reproduce the forces on the atoms in the buffer and inner regions, this approach accurately describe basic properties of a dislocation.

In order for the first assumption (a) above to hold, the inner core region must be sufficiently large to contain all atoms with displacements outside of the linear regime and the buffer region must be sufficiently wide so that displaced atoms in the core have no effect on the forces experienced in the continuum-response region. The second assumption (b) requires that the continuum-response region to be sufficiently large so that its termination has no effect on the forces on the atoms in the buffer or inner region. The radius of the calculation must therefore exceed the sum of the non-linear core radius plus twice the range over which motion of atoms creates forces within the lattice. As the latter range can be quite large for electronic structure calculations in metals, the application of this approach to electronic structure calculations can be problematic.

The Greens function approach has predicted successfully dislocation properties when applied to time consuming empirical potentials [76, 113] which have a limited interaction range. The approach also has been applied to density functional calculations of the Peierls stress for molybdenum and tantalum [107, 108], where its application is more questionable due to the above interactions. In these latter works, the artificial boundary on the outside of the continuum-response region have been treated in one of two ways [107, 108], either by keeping the surface free in vacuum or by embedding in periodic boundary conditions with the vacuum filled with material which must contain severe domain boundaries due to the incompatibility of a net Burgers vector with periodic boundary conditions.

To gauge the effects which this artificial boundary may have and how far these effects penetrate from the continuum-response region into the buffer region, we perform a test calculation within the density functional theory pseudopotential approach [71] of the magnitude of the forces generated onto the system due to the presence of a domain boundary similar to those in the works cited above [107, 108].

For this calculation, we employ the same computational procedure as for our production calculations in Section 5.4. Here, however, as this is a test, we employ only a single k-point to sample the Brillouin zone (Γ). We begin with an orthorhombic cell of 24 atoms of tantalum in a bulk arrangement with supercell lattice vectors $\vec{r}_1 = a\langle 1\bar{1}0\rangle$, $\vec{r}_2 = 4a\langle 11\bar{2}\rangle$ and $\vec{r}_3 = a/2\langle 111\rangle$. We choose this cell because its length along $\vec{r}_2$ is the same as the smallest simulation cell used in References [107] and [108]. We then generate a domain boundary at the edge of cell along the $(11\bar{2})$ plane by changing the lattice vector $\vec{r}_2$ to $\vec{r}_2 = 4a\langle 11\bar{2}\rangle + \alpha\vec{r}_3$ and holding the atoms fixed in their bulk locations ($\alpha = 0$). α is chosen such that the shift is small and the nearest neighbor distance is always within 95% of the bulk, representing even less of a disturbance that in Reference [107], where atom were within 90% of the bulk nearest neighbor distance. To estimate the effect of the scattering of electrons at the domain boundary on the interatomic forces, we hold the atoms fixed and compute the *ab initio* forces acting upon them.

Figure 5-1 shows the forces along the $\langle 111\rangle$ direction as a function of distance from the center of each domain. Note that relatively large forces develop deep within the cell. These data indicate that the continuum-response region should be quite large ($\approx 5-10$ Å) in order for the response of the electrons not to adversely effect the forces in the buffer region. Note also that the the buffer region should be of similar width to prevent forces from the non-linear displacements in the core from penetrating into the linear continuum-response region. Such large continuum-response and buffer regions can make the calculation infeasible with current computational techniques.

In fact, the only density functional calculations of the Peierls stress in this system to date employ the Greens function method but with a distance from the buffer region to the domain boundary of only ≈ 3.7 Å. It thus is unclear whether the continuum region in these calculations is sufficiently large to lead to reliable results and clearly

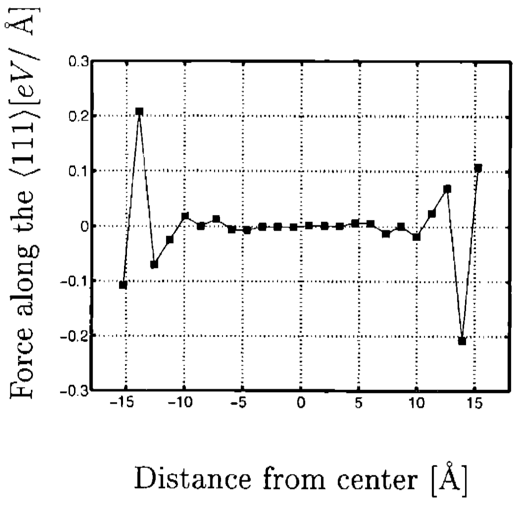

Figure 5-1: Force on the atoms, along the ⟨111⟩, due to the presence of a domain boundary. The forces are plotted as a function of distance from the center of the unit cell. The domain boundary is generated such that the nearest neighbor distance is always within 95% of the bulk ($\alpha = 1/4$).

further calculations are needed to support those results. Below, we provide just such calculations using the method of periodic boundary conditions, which perturb the electronic system far less than the introduction of domain boundaries.

5.1.3 Periodic Boundary Conditions

The final common choice for boundary conditions is to repeat the dislocation core periodically throughout space, so that the dislocation is no longer isolated, but embedded in bulk material containing an array of dislocations. Consistency with periodic boundary conditions then demands that the unit cell contain an even number of dislocations with Burgers vectors of alternating sign, arranged typically in dipolar [78, 8, 53] or quadrupolar [12, 53, 42] arrays. For static properties of the dislocation core, such cells give reliable results as the elastic fields of the surrounding dislocations effectively cancel at the location of each core.

Periodic boundary conditions can also been used to calculate the Peierls stress [81, 102, 16]. Care must be taken, however, because the symmetry of the dipole/quadrupole array breaks as the dislocations move and the dislocation-dislocation interaction then ceases to be negligible. The use of large unit cells can control this effect [16]; however, such a direct, brute-force approach is not practical for computationally demanding *ab initio* calculations. To make such calculations feasible, they must occur in small periodic cells, thereby demanding proper accounting of the dislocation-dislocation interactions.

We have shown in another work [81] that, under certain conditions, such interactions can be accounted accurately with minimal extra computational effort, so that accurate values of the Peierls stress can be obtained from density functional calculations in periodic cells. As the residual errors with this approach are associated with the boundary conditions, the magnitude of such an error can be tested by other computational methods, such as empirical potentials. Our previous work shows that that this residual error is relatively small [81], a fact which we confirm explicitly below.

Because the deviations from the bulk arrangement at periodic boundaries are relatively mild, such calculations are ideal for mitigating electronic boundary effects. Given the simplicity of working with these boundary conditions and the possibility of the extraction of accurate values for the Peierls stress from small unit cells, we choose to work with periodic boundary conditions throughout this work. Section 5.3 outlines our procedure for calculating the Peierls stress while working with periodic boundary conditions and describes the sources and the magnitude of the residual errors. (See Reference [81] for a full discussion of these issues.)

5.2 Dependence of the Peierls stress on orientation and temperature

[1]

To illustrate the complexities of relating computational predictions to experimental findings, we now explore the dependence of the Peierls stress in bcc tantalum on orientation and temperature. The strong dependencies which we shall find underscore

---

[1] The calculations in this section were done by Alejandro Strachan from the Process Simulation Center, Beckman Institute, California Institute of Technology.

the unique properties of dislocations in this material.

Despite recent advances in *ab initio* quantum mechanical methods, such methods are still too computationally intensive to study such properties as the temperature dependence of the Peierls stress. Therefore, for these calculations, we employ a molecular dynamics (MD) framework carried out using a first-principles-based, many body force field (FF) for tantalum, which we denote qEAM, which we have developed to allow accurate and computationally efficient evaluation of atomic interactions [89, 102].

As described above, we carry out these calculations within periodic boundary conditions. The super-cell consists of a quadrupolar arrangement [12, 53] of dislocations containing 5670 atoms with lattice parameters $a_x = 70.59$ Å, $a_y = 73.39$ Åand $a_z = 20.11$ Å, where the x-, y-, and z- axes of our coordinate system are along $\langle 1\bar{1}0 \rangle$, $\langle 11\bar{2} \rangle$, and $\langle 111 \rangle$ directions, respectively. As we have shown in a another work [81], such a cell gives very accurate values for the Peierls stress.

5.2.1 Orientation dependence of the zero-temperature Peierls stress of the $\langle 111 \rangle$ screw dislocation

To calculate the zero temperature Peierls stress, we start with a fully relaxed quadrupole dislocation configuration at zero stress and increase the stress in steps of 50 MPa until the dislocations move. Once the dislocations move, we restart the calculation from the structure equilibrated just prior to the motion and increase the stress in smaller steps (5 MPa) in order to more narrowly define the critical stress. At each incremental target stress, we relax the atoms and stresses in the cell by running two very low temperature (T=0.001 K) MD simulations. The first run is for 15 ps at constant stress and temperature (NσT ensemble) using a Rahman-Parrinello barostat [70] and a Hoover [39] thermostat, and the second run is for 50 ps at constant volume and temperature (NVT ensemble). We find this approach to be quite stable for relaxing the cell and the atoms of the system.

The $\langle 111 \rangle$ screw dislocation has three equivalent $\{112\}$ and three equivalent $\{110\}$ potential slip planes, with such planes occurring at 30° intervals. To study the orien-

Potential	Twin	⟨112⟩	Anti-Twin	Asymmetry
qEAM FF	575 MPa	655 MPa	1075 MPa	1.6412
MGPT [113]	605 MPa	640 MPa	1400 MPa	2.29

Table 5.1: Peierls stress for the ⟨111⟩ screw dislocation in tantalum in the twinning, ⟨112⟩ and anti-twinning directions; the last column shows the ratio between anti-twinning and twinning Peierls stresses. MGPT results from Yang et al [113].

tation dependence of the Peierls stress, we apply three types of pure shear stress to the system: a σ_{xz} stress, a positive σ_{yz} stress and a negative σ_{yz} stress. (Note that with coordinate axes as defined above, the z-axis lies along the dislocation line.) These stresses leads to forces on the dislocation in the ⟨112⟩, ⟨110⟩-twinning and ⟨110⟩-antitwinning directions, respectively [38]. Along these directions, we find Peierls stresses of $\tau_{112} = 655$ MPa, $\tau_{twin} = 575$ MPa, and $\tau_{antitwin} = 1075$ MPa, respectively. Table 5.1 shows that our essentially zero-temperature results are in good agreement with those of Yang and collaborators [113], who employed model generalized pseudopotential theory (MGPT) [110], a different inter-atomic potential. The result of such a strong dependence of the Peierls stress on orientation is consistent with the experimentally observed breakdown of the Schmid law in bcc metals.

To make quantitative comparison with experiments, which are carried out at nonzero temperature, we compare our results to those of Tang *et. al* [94], who fit experimental data [104] to a mesoscopic model and then extrapolate to extract the zero-temperature Peierls stress. Their predicted value of 248 MPa for the ⟨112⟩ Peierls stress is over a factor of two lower than our result. This type of discrepancy, where the theoretical Peierls stress overestimates the zero-temperature extrapolation of the experimental data by a factor of two to three, is quite generally observed [25]. This discrepancy may be due either to inaccuracies in the theoretical calculations or, perhaps, to a flaw in the comparison between the zero-temperature extrapolation of the experimental data and theoretical predictions.

5.2.2 Temperature dependence of the Peierls stress of the $\langle 111 \rangle$ screw dislocation

To explore potential difficulties with the zero-temperature extrapolation, we now present what to our knowledge is the first temperature-dependent study of Peierls stress using a realistic potential for a bcc metal. For these calculations, we continue to employ the qEAM FF and begin with the zero-temperature, equilibrated structures. We then apply various constant shear stresses (lower than the T=0 Peierls stress) to the system while slowly increasing the temperature (in steps of 10 K) until the dislocations move. Similarly to the T = 0.001K case, for each temperature we first run for 10 ps in the NσT ensemble and then for 25 ps in NVT ensemble.

Because the Peierls stress can depend on the rate at which the strain is applied, to place our results in context, we first estimate the strain rate in our computations. The strain rate is approximately $\dot{\gamma} = \rho v_d b$, where v_d is the dislocation velocity, ρ is the dislocation density and b is the Burgers vector. Using a dislocation density typical of the experiments [94] ($\rho = 10^{11} 1/m^2$) and estimating the dislocation velocity as the ratio between the distance traveled in one jump ($1/3a\langle 112 \rangle = 2.717$ Å) and the simulation time (35 ps), we obtain an effective strain rate of $\sim 10^2 1/s$, which is large compared to the strain rates (4×10^{-5}) in the experiments used for the zero-temperature extrapolations [94, 104].

Figure 5-2 summarizes our results for the temperature dependence of the Peierls stress as a function of temperature for the three directions ($\langle 112 \rangle$, twinning and anti-twinning). As expected, the Peierls stress obtained from our MD simulations decreases rapidly with increasing temperature, particularly for very low temperatures. It is important to mention that, although our simulations are three dimensional, the dislocations move as straight lines without the formation of double kinks because our simulation cell is only seven Burger's vectors long along the dislocation lines. Such double kinks are quite important at finite temperatures as they tend lower the lattice resistance at non-zero temperatures. Our results are approximately a factor of $2 - 4$ larger than the fit of Tang *et. al.* [94] to the experimental data of Wasserbäch [104].

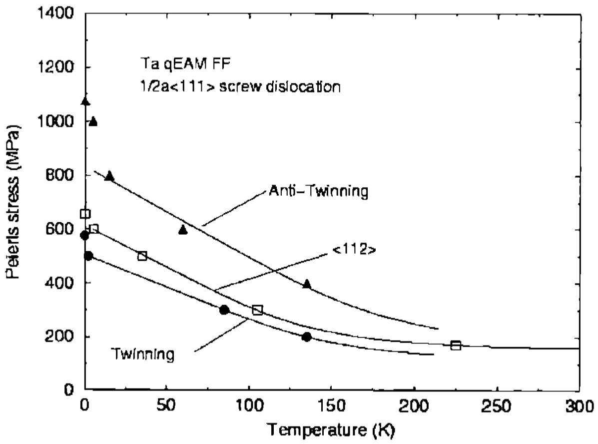

Figure 5-2: Temperature dependence of the Peierls stress along various directions: the ⟨112⟩, twinning and anti-twinning directions. The fits are done for the high temperature data using Equation (5.1). The temperature is in Kelvin, and the stress in MegaPascals.

We feel that this is reasonable, considering the facts that our simulation cells do not allow for double kink formation and that, as discussed above, our strain rates are much higher than those in the experiments [94, 104].

Experimental extrapolations of the Peierls stress to zero temperature generally come from mesoscopic or kinetic/thermodynamic model [94, 51, 22, 21] fits to experimental data and extrapolated to zero temperature. To explore the effects of this procedure, we fit our atomistic data to such a model, perform the extrapolation and then compare with our direct zero-temperature results.

For the fit we use an analytical expression for the dependence of the Peierls stress with temperature at constant strain rate [21, 22] based on a mechanism involving double kink nucleation and propagation. This model gives for the temperature dependent Peierls stress

$$\tau_P = \frac{\tau_0}{\beta E^{\mathrm{kink}}} \mathrm{asinh}\left(\frac{\dot{\gamma}}{\dot{\gamma}_0^{\mathrm{kink}}} \mathrm{e}^{\beta E^{\mathrm{kink}}} \right), \tag{5.1}$$

where β is $1/k_B T$, with k_B being Boltzmann's constant and T the absolute temperature, E^{kink} is the kink energy [38], τ_0 is the effective Peierls stress and $\dot{\gamma}_0^{\mathrm{kink}}$ is the reference strain rate. Here, the effective Peierls stress is

$$\tau_0 = \frac{E^{\text{kink}}}{bL^{\text{kink}} l_P} \tag{5.2}$$

and the reference strain rate is

$$\dot{\gamma}_0^{\text{kink}} = 2b\rho l_P \nu_D, \tag{5.3}$$

where b is the Burgers vector, L^{kink} is the kink length, ρ is the dislocation density and ν_D is the attempt frequency which may be identified with the Debye frequency to a first approximation [21, 22], and l_P is the distance between two consecutive Peierls valleys. Physically, E^{kink} is the minimum energy to form a double kink, L^{kink} is the minimum length for this double kink and τ_o is the stress, whose work to move a dislocation a distance l_P is equal to E^{kink}.

Figure 5-2 shows the fit of Equation (5.1) to our atomistic data. To mimic how zero-temperature lattice resistances are generally extracted, we adjust the three unknown parameters (τ_0, E^{kink} and $\dot{\gamma}_0^{\text{kink}}$) to fit our higher temperature data *only*. Intriguingly, extrapolation of our higher temperature results to zero-temperature leads to an underestimation of the Peierls stress of between 10% and 20%. We would expect that a fit to data from a cell sufficiently large to allow for double kink formation (which is active in the experiments at non-zero temperatures) would lead to an even a larger underestimation of the zero-temperature stress. These results therefore suggest that the general discrepancy between extrapolated experimental values and the calculated values for the zero-temperature Peierls stress may be the result of failure of nonzero-temperature models to describe properly the low-temperature regime. This illustrates one possible difficulty in relating the experiments to computational predictions and underscores the need for first principles studies of such a phenomena.

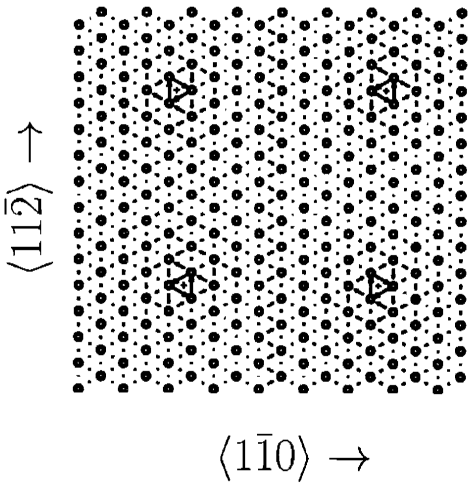

Figure 5-3: Quadrupolar unit cell of size 42Å× 41Å: relative displacements of neighboring columns of atoms (arrows), dislocation centers (plus signs).

5.3 Accurate Peierls Stress Calculations in small periodic cells

Having underscored the need for first principles electronic structure studies and already determined the most effective boundary conditions for such studies as periodic, we now focus on determination of the cell of minimal size appropriate to calculation of the zero-temperature Peierls stress for a ⟨111⟩ screw dislocation in bcc tantalum for shear along the (110) plane.

To minimize image effects, we employ periodic boundary conditions with a quadrupolar unit cell. Figure 5-3 shows a differential displacement map [100] of such a cell of size 42Å× 41Åin the plane perpendicular to the Burgers vector. In such a map, the dots indicate columns of atoms along the ⟨111⟩, and the vectors between the columns of atoms indicate the relative shift along the Burgers vector due to the presence of a dislocation between each pair of columns, with the vectors scaled so that a vector of full length between the columns corresponds to 1/3 a Burgers vector. In this ground state structure of the dislocation, triads of full length vectors surrounds the center of each dislocation, corresponding to a new displacement by a full Burgers vector upon completion of a closed loop about the each center.

As Section 5.1 notes, for calculations of static properties such as the ground-state dislocation core structure, the strain fields from the surrounding dislocations in a quadrupolar array essentially cancel at each dislocation core. However in a dynamical problem such as the calculation of the Peierls stress, the dislocations begin to interact with the stress fields of the others as they begin to move. Our previous work [81] shows that, for the particular geometry considered here, accurate values for the Peierls stress can be extracted from quite small unit cells provided the proper procedure is followed. We now outline that procedure while reviewing the relevant background.

5.3.1 Calculation of Peierls stress within periodic boundary conditions

To calculate the Peierls stress in a small periodic cell, we begin with lattice vectors appropriate to bulk material in the absence of dislocations and then, while relaxing the internal coordinates of the cell, apply increasing pure ϵ_{xz} strains (same Cartesian coordinates from Section 5.1.3) until the dislocations move. Such a strain drives the dislocation along the $\langle 11\bar{2}\rangle$ direction [38]. Before the dislocation moves, the strain energy of the cell increases quadratically,

$$E = \frac{1}{2}C'\epsilon_{xz}^2, \tag{5.4}$$

where C' is an elastic constant associated with the quadrupole unit cell which can be extracted simply from the energies of the cell as the strain increases. The stress associated with this strain is

$$\sigma_{xz} = C'\epsilon_{xz}, \tag{5.5}$$

so that at the strain at which the dislocation moves, Equation (5.5) gives the Peierls stress.

The great benefit of the above procedure is that it requires a *minimal* search through phase space in order to calculate the Peierls stress and accounts accurately for the effects of the dislocation-dislocation interactions. The C' elastic constant, which comes as a direct byproduct of the procedure and requires no further calculations, suffices to account accurately for the leading order effects of the inter-dislocation interactions. This correction captures most of the effects from working with small unit cells and and can differ from that of an equivalent bulk cell by a value of two or more.

The above procedure involves several approximations requiring justification. First, we apply strain relative to the lattice vectors of the bulk cell in the absence of the dislocation, rather than those of the quadrupole array. Previously, we have shown through explicit calculation on model inter-atomic potentials that working with the relaxed lattice vectors of the quadrupolar array does not improve the value calculated for the Peierls stress and therefore is not needed [81]. The reason for this is that although working with the bulk lattice vectors generates artificial stresses, these are primarily diagonal (σ_{ii}), because the greatest effect of the presence of the dislocations is to dilate the system [81]. In the present geometry, such diagonal stresses result only in a constant shift in the energy over the range of applied strain and do not generate driving (Peach-Kohler [38]) forces on the dislocations [81].

Some slight care must be taken with the above argument. Duesbery and others [24, 44] have pointed out that stresses which do not result in driving forces on a dislocation still may affect the overall value of the Peierls stress needed to drive the dislocation, because such stresses may modify the dislocation core structure [26], an effect not accounted in linear elasticity theory. This effect of non-driving stresses is, in fact, one of the common violations of the Schmid law which bcc metals exhibit. Diagonal stresses, however, do not have a large effect [24] on the value for the Peierls stress, as they tend to only compress or expand the core. Fortunately, because the bulk lattice vectors should be relatively close to the that of the dislocation cell, we expect all of these effects to be quite small, as we have found previously [81] and again verify in the test calculations below.

The second simplification in our procedure is that rather than applying a stain which imposes a pure σ_{xz} stress, we apply a pure ϵ_{xz} stain, which also generates a residual σ_{xy} stress [38]. To generate a pure stress of the form σ_{xz}, one would have to apply an additional ϵ_{xy} stain of a magnitude determined by yet another elastic constant of the quadrupolar array. Because the calculation of this constant would increase significantly the number of calculations required and because the residual σ_{xy} stress [38] acts on the plane perpendicular to the dislocation and thus does not create a driving force on the dislocations, we simply apply the pure ϵ_{xz} strain. As with the diagonal stress components, although the residual in-plane σ_{xy} stress does not drive the dislocations, it can affect the Peierls stress by modifying the core structure. Unlike the diagonal stress components, the in-plane stress does significantly affect the Peierls stress in bcc metals [24, 44]. This effect, however, will be small so long as the residual σ_{xy} stress is small compared to the driving σ_{xz} stress. The ratio σ_{xy}/σ_{xz}, is equal to C''/C' where C' is the elastic constant appearing in Equation (5.4) and C'' is another combination of elastic constants. In pure bulk cubic materials these constants have the form [38]

$$\begin{aligned} C' &= \frac{1}{3}(C_{11} + C_{44} - C_{12}) \\ C'' &= -\frac{\sqrt{2}}{6}(2C_{44} + C_{12} - C_{11}), \end{aligned}$$

where the C_{ij} are the standard elastic constants for cubic materials.

As evidence of the correlation between the ratio of these constants and the errors in the Peierls stress, we note that in our previous study [81] with same empirical potential as in Section 5.2, the ratio C''/C' varied from approximately 1/5 in the smallest cell studied to less than 1/10 for all other cells while the error in extracting the Peierls stress went from 18% to less than 2%, respectively. For the potential used in that study, the value of C''/C' computed from bulk elastic constants is 1/90. As the bulk value of C''/C' within density functional theory is less than 1/100 [42], we expect the errors in our *ab initio* value of the Peierls stress to be even somewhat smaller. Lending further support to this view is the result of Duesbery and Vitek [26] demonstrating that the effect of σ_{xy} stresses on core structure is much less for the non-degenerate core structure which we have in our density functional calculations than for the degenerate core structures in our inter-atomic potential calculations.

5.3.2 Demonstration

To demonstrate the efficacy of the above procedure, we now proceed to extract the (110)-plane Peierls stress for vanadium and tantalum from calculations in small periodic cells. To allow comparison with the Peierls stress of isolated dislocations, we employ empirical potentials for this demonstration. For vanadium we use the Finnis-Sinclair [29] potential with modifications made Ackland and Thetford [4], and for tantalum we use the same potential as in Section 5.2 but with a slight adjustment of parameters to produce a non-degenerate core structure. The bulk ratios for C''/C' for vanadium and tantalum within these models are 1/10 and 1/6.5, respectively, much larger than the density functional theory value.

To determine the reference value for the Peierls stress, we employed cylindrical boundary conditions with large amounts of material, increasing the radius of the cylinders until the boundary forces were small [82] and the Peierls stress approached an asymptotic value, where we define the Peierls stress as the critical stress for the dislocation core to first move to a new triad of neighboring columns of atoms. To extract the Peierls stress from within periodic boundary conditions, we follow precisely the procedure which Section 5.3.1 outlines.

Figure 5-4 shows the resulting energy versus stain curve for vanadium within a periodic cell of size 42Å× 20Å. At a strain ≈ 0.054, the curve exhibits a discontinuity signaling the critical strain for moving the dislocation. The curvature of the fit determines the elastic constant C' through Equation (5.4). Finally, combining this value of C' with the observed critical stress through Equation (5.5) yields the Peierls stress. We repeated this procedure for tantalum as well.

Table 5.2 summarizes our results for both vanadium and tantalum. The table shows that the errors are relatively small, much smaller than the general discrepancy between empirical potentials and the experimental extrapolations. It is also noteworthy that the potentials employed in this demonstration exhibit C''/C' ratios over an order of magnitude larger than density functional theory. From these and previ-

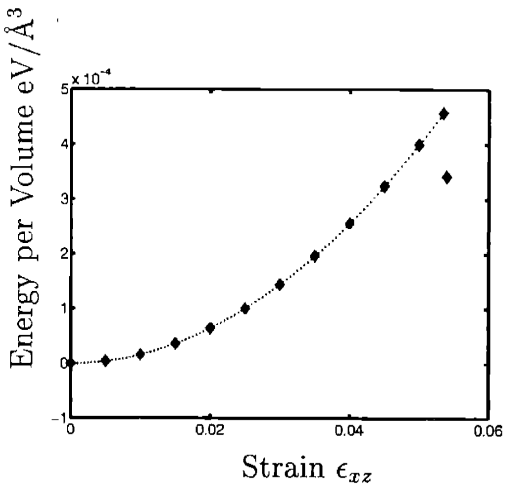

Figure 5-4: Energy versus strain of vanadium in a quadrupolar cell of size 42Å× 20Å. Diamonds denote the energy calculated at various strains. The line is a quadratic fit up to the Peierls stress.

	23Å× 11.5Å	42Å× 20Å
Ta	25%	10%
V	26%	11%

Table 5.2: Magnitude of percentage error in calculating the Peierls stress in periodic supercells of two different sizes from empirical potentials for vanadium and tantalum.

ous results [81], we conservatively estimate that the error in the Peierls stress in the density functional calculations below should be no greater than ≈ 20%.

5.4 Density functional results and discussion

5.4.1 Computational Details

All of our first principles electronic structure calculations employ the plane-wave density-functional pseudopotential approach [71] within the local density approximation [19, 72]. We employ pseudopotential of the Kleinman-Bylander form [50] with *s*, *p* and *d* non-local channels which has been used successfully in previous works [106, 42] and a plane wave basis with cut off of 40 Rydberg. As justified above, we employ a super-cell containing a quadrupolar array of dislocations with lattice vectors $\vec{a}_1 = 5a[1,\bar{1},0]$, $\vec{a}_2 = 3a[1,1,\bar{2}]$, and $\vec{a}_3 = a[1,1,1]/2$, where $a = 3.25$ Åis the lattice constant of the cubic unit cell. To carry out the integrations over the Brillouin we use a non-zero electronic temperature of $k_B T = 0.1$ eV to facilitate integration over the Fermi surface and sample the zone at eight special k-points $k_1 = k_2 = 0$, $k_3 \in \pm\{\frac{1}{16}, \frac{3}{16}, \frac{5}{16}, \frac{7}{16}\}$. These choices give energy differences reliably to within 0.1 eV/atom. Finally, to determine the electronic structure, we minimize using the analytically continued functional approach [6], expressed within the DFT++ [40] formalism.

5.4.2 Energy landscapes

[2]

To demonstrate the discrepancies that occurs between the predictions of empirical potentials and first principles electronic structure studies, we compare the energy landscape for a dislocation moving along a reaction coordinate from the easy core configuration to the hard core configuration [100, 111] for both molybdenum and tantalum as determined within MGPT [110] and as calculated *ab initio*. Within MGPT, we have carried out the calculation for molybdenum ourselves and we used the hard-easy core energy difference reported in the literature [65] for tantalum. Within density functional theory, we have calculated the energy at a number of points along the reaction pathway for tantalum, and for molybdenum we report the difference between the easy core and hard core configurations as found in Reference [42]. We also note that, for molybdenum, within density functional theory, the hard core configuration was not stable and therefore the stable structure found within MGPT was used as the reference state.

Figure 5-5 shows the results. Most noticeably, the atomistic landscapes are three times stiffer than the *ab initio* landscapes. This raises the question whether the approximate factor of three overestimate of theoretical calculations over the extrapolation of the experimental Peierls stresses to zero-temperature is due to defects in

---

[2] The calculations in this section were done by Sohrab Ismail-Beigi from the Department of Physics, University of California at Berkeley.

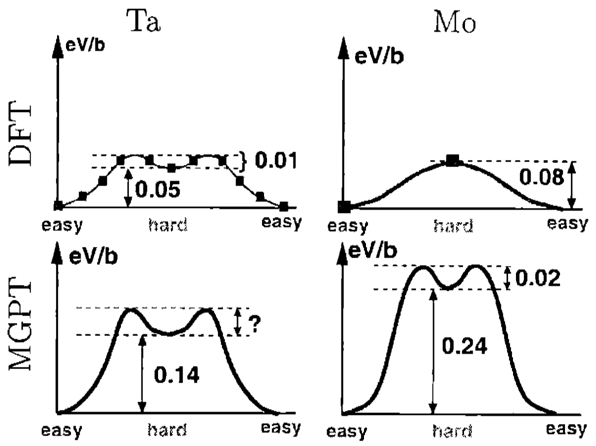

Figure 5-5: Energy landscape along a reaction coordinate when going from the easy core to the hard core configurations in tantalum and molybdenum: density functional theory (squares in upper panels), MGPT (curves in lower panels). *Ab initio* results for molybdenum are from Reference [42], and the MGPT tantalum results are from Reference [65].

the inter-atomic potentials or to failures in the connection between the experiments and the theoretical calculations.

5.4.3 Verification of cell size

To compute the Peierls stress, we shall employ a cell of dimensions 11.5Å× 23Å. To verify that long-range electronic structure effects in metals do not interfere with results in such a cell, we compare the core structure reported previously [42] for this cell with a new calculation using a larger cell. Figure 5-6 shows the result for the core structure in cell of size 21Å× 40Å. Such a cell has size $\vec{r_1} = (9/2)a[1,\bar{1},0]$, $\vec{r_2} = 5a[1,1,\bar{2}]$, and $\vec{r_3} = a[1,1,1]/2$. The lattice vectors are $a_1 = r_1 - r_2/2 + r_3/2$, $a_2 = r_1 + r_2/2 + r_3/2$ and $a_3 = r_3$. The k-point sampling is the same as above.

We note that the core structure is very similar to previous results [42] which used a smaller cell equal in size to that we shall employ for our calculation of the Peierls stress. We therefore do not expect the long-range nature of electronic effects in metallic systems to greatly effect the value which shall extract for the Peierls stress from the smaller periodic cell. We also note that the empirical potential results for

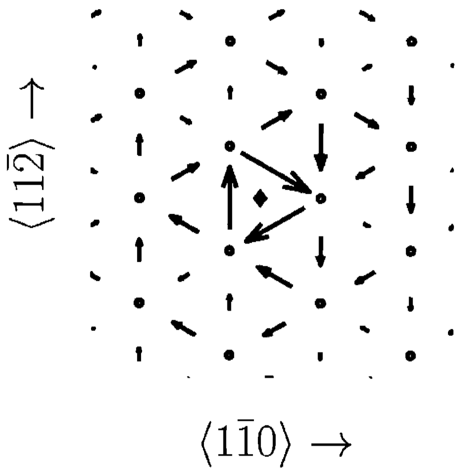

Figure 5-6: Easy core structure for tantalum calculated within density functional theory. This cell of size 21Å× 40 Ågives very similar results to the cell of size 11.5Å× 23Å, used in Reference [42]. The diamond in the figure represents the center of the dislocation.

tantalum (Section 5.3) had a very large cutoff of 9Åand accurate results were obtained in the smallest cells in those calculations. These facts lend confidence in the reliability of our density-functional theory predictions below.

5.4.4 Results for the Peierls Stress

Figure 5-7 shows the present status of our density functional theory results for energy as a function of strain following the procedure of Section 5.3.1. We regard each data point as fully relaxed when the magnitude of the residual force on each atom is less than 0.005 eV/Å. In interpreting this data, it is important to note that only the data for strains less than 0.045 have reached this criterion. We present all of the data points, however, as bounds on the value for the Peierls stress can still be obtained.

From Figure 5-7 it is apparent that, at a strain of 0.060 the Peierls stress has been exceeded, whereas at a strain of 0.045 the energy curve lies on the elastic solution. At present, it remains unclear whether the energy for a strain of 0.050 will place it above or below the Peierls stress. From the curvature of the data in the elastic region and these critical strains, we bound the Peierls stress to be between 1.3 GPa and

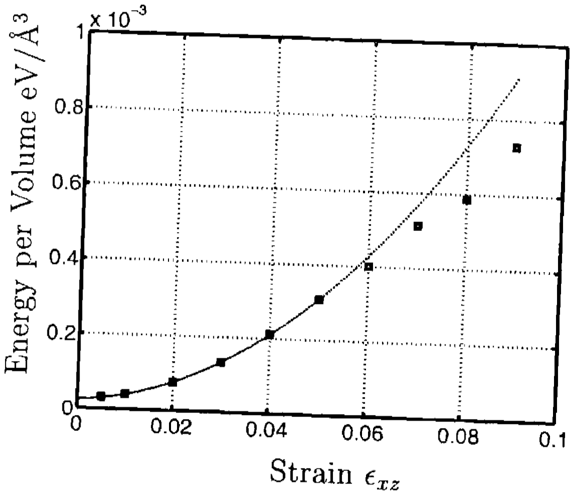

Figure 5-7: Energy versus strain for tantalum in a quadrupolar cell of size 11.5Å × 23Å, calculated within density functional theory. Squares denote the calculate energy at various strains. The line is a quadratic fit to the first six data points. The points with strain above 0.045 have not been fully converged. The graph indicates that the points with strain above 0.05 (stress = 1.7GPa) will be at a stress above the Peierls stress.

2.0 GPa, where for these values we quote the full magnitude of the applied stress and not the resolved shear stress, as do some authors. These results are consistent with the previous density functional result of 1.9 GPa obtained using Greens function boundary conditions [108].

Figures 5-8 and 5-9 show differential displacement maps [100] of the dislocation configuration at stresses of 1.3 GPa and 3.0 GPa, respectively, where the diamonds represent the location of the center of the dislocation before the application of stain. Note that the ions have been fully relaxed in Figure 5-8, but not in Figure 5-9. Figure 5-8 shows the relaxed dislocation core to remain in the position of its unstressed state, whereas Figure 5-9 shows that at a stress of 3.0 GPa, the dislocation moves into the split core configuration, in which over half of the core has moved to a new triad, along a [110] plane. Further relaxation should result in a configuration in which the core has moved onto the next triad of columns of atoms.

Intriguingly, despite the fact that the *ab initio* energy landscape is *less* corrugated than that of the interatomic potential by a factor of nearly three (Figure 5-5), the

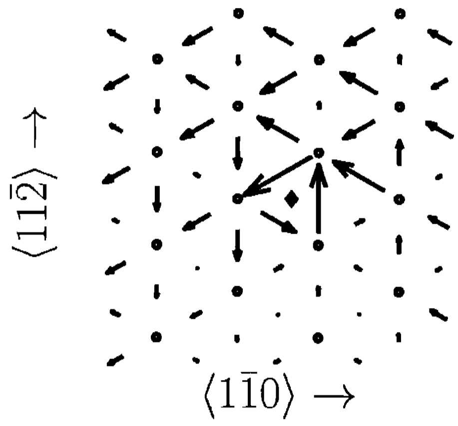

Figure 5-8: Differential displacement map at a stress of 1.3 GPa. The cell has converged to within the tolerance defined in the text. The diamond in the figure is the location of the center of the dislocation, under no stress. The center of the dislocation, at this applied stress, has not moved.

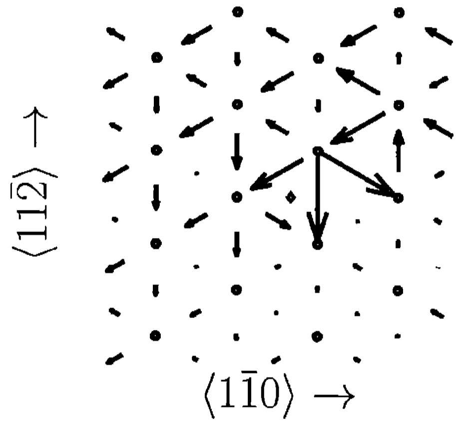

Figure 5-9: Differential displacement map at a stress of 3.0 GPa. The cell has *not* converged to within the tolerance defined in the text. This figure shows a split core, where a majority of the dislocation has moved to a new triad along a [110] direction.

above *ab initio* result for the Peierls stress is a factor of two *larger* than the empirical potential result (Table 5.1). Moreover, our result is a factor of six *larger* than extrapolations of experimental data to zero-temperature [94], a discrepancy much larger than any effects from the use of either our relatively small quadrupolar cell or the local density approximation to density-functional theory. Certainly, as Section 5.2 shows, some of this discrepancy can be due to the extrapolation of experimental data to zero temperature. However, errors in the zero-temperature extrapolation may not likely does not account for all of the discrepancy as the underestimation in Figure 5-2 is only $\approx 10-20\%$. One must therefore consider the possibility of other factors such as the effects of kinks, defects, surfaces, strain-rate dependencies and screening from the presence of other dislocations.

5.5 Conclusion

This work explores various aspects of the the Peierls stress for the $\langle 111 \rangle$ screw dislocation in bcc tantalum. The first non-zero temperature results for the Peierls stress in this system shows both a strong orientation and temperature dependent response, consistent with experimental results. These data also demonstrate that common extrapolations of experimental data tend to underestimate the zero-temperature limit.

We have also presented the first density functional theory calculation for the Peierls stress within boundary conditions, the approach best suited to metallic systems. The value we find for the Peierls stress is substantially larger than both the experimental extrapolations and current empirical potential results. This difference is much larger than errors which could normally be attributed to the use of a relatively small unit cell or the local density approximation to density-functional theory. The error is also significantly larger than the underestimation we have seen in the the extrapolation of nonzero-temperature data to zero temperature, thus supporting the notion that mechanisms other than the simple Peierls resistance may play an important role in controlling the process of low temperature slip.

Appendix A

Application to Kleinman-Bylander pseudopotentials

This appendix reviews briefly the application of our approach to norm-conserving pseudopotentials of the Kleinman-Bylander form, where the approach essentially becomes a softening procedure without transferability biases. The softening comes at the cost of generating a generalized eigenvalue problem, similar in spirit to the ultrasoft pseudopotential (USSP) [98] and projector augmented wave (PAW) [13] methods. However, unlike the USSP and PAW approaches, where the softening takes place referenced to a spherical atomic environment, in our approach the softening occurs in the full crystalline environment and thereby includes nonlocal interactions from multiple scattering events from different atoms in the crystal but at minimal extra computational cost.

Here, we develop the approach to work with standard separable non-local potentials of the form

$$H_{nl}(\vec{G},\vec{G}') = \sum_{at,pr} |V_{at,pr}(\vec{G})\rangle f_{pr} \langle V_{at,pr}(\vec{G}')|, \tag{A.1}$$

where the sum is over all atoms in the cell and all projectors on a given atom. For such potentials it proves much more computationally efficient to use the forms similar to Equations (2.26), (2.27) and (2.28) for the overlap matrix $\mathcal{O}$, $\mathbf{C}^Q$ and H^{eff}, respectively. The overlap matrix then takes the form

$$\begin{aligned}\mathcal{O} &= 1 + \\ &\left(H_{nl}^{PQ} + H_{loc}^{cr-at,PQ}\right) \frac{1}{H_o^{QQ} H_o^{QQ}} \left(H_{nl}^{QP} + H_{loc}^{cr-at,QP}\right),\end{aligned} \tag{A.2}$$

where H_{loc}^{cr-at} is the local term for the "free-atom" crystal, a crystal whose charge density is a direct superposition of the charge densities from isolated atoms. This term includes the local part of the ionic potential, the Hartree term and the exchange-correlation term. Ignoring the identity, expansion of Equation (A.2) results in four terms, which we refer to as nonlocal-nonlocal, nonlocal-local, local-nonlocal and local-local, respectively. The local-local term is exactly the same as that of the Coulomb potential and therefore should be treated as in the manuscript. The advantage of employing a fixed, rather than self-consistent, overlap matrix is that each of the remaining terms contract contract onto the P-space only. We now consider each of these in turn.

The $\vec{p}, \vec{p}'$ component of the nonlocal-nonlocal term is

$$\mathcal{O}_{nl,nl}(\vec{p}, \vec{p}') = \sum_{\substack{\mathrm{at,pr} \\ \mathrm{at',pr'}}} |V_{at,pr}(\vec{p})\rangle f_{pr} A^{(2)}_{\substack{\mathrm{at,pr} \\ \mathrm{at',pr'}}} f_{pr'} \langle V_{at',pr'}(\vec{p}')|, \tag{A.3}$$

where

$$A^{(2)}_{\substack{\mathrm{at,pr} \\ \mathrm{at',pr'}}} = \sum_{\vec{q}} \langle V_{at,pr}(\vec{q})| \left(\frac{1}{\frac{1}{2}\vec{q}^2}\right)^2 |V_{at',pr'}(\vec{q})\rangle. \tag{A.4}$$

This term quantifies how the high-momentum states components couple to the ions, including not only couplings to individual atoms but also to pairs of atoms through $A^{(2)}_{\substack{\mathrm{at,pr} \\ \mathrm{at',pr'}}}$, thereby including environmental effects directly into the potential and enhancing transferability. In terms of implementation, this term requires almost no additional memory as the only additional storage is for $A^{(2)}$ and scales as $N_b \times N_b$, where N_b is the number of bands. The computational demands are quite light as $A^{(2)}$ requires an amount of computing comparable to a single orthonormalization of the electronic bands and only need be compute once at the very beginning of the calculation.

The local-nonlocal and nonlocal-local terms are just hermitian conjugates of each other. The $\vec{p},\vec{p}'$ component of the nonlocal-local term has the form

$$\mathcal{O}_{nl,loc}(\vec{p},\vec{p}') = \sum_{at,pr} |V_{at,pr}(\vec{p})\rangle f_{pr} \langle F^{(2)}_{at,pr}(\vec{p}')|, \tag{A.5}$$

where

$$\langle F^{(2)}_{at,pr}(\vec{p}')| = \langle V_{at,pr}(\vec{q})| \left(\frac{1}{\frac{1}{2}\vec{q}^2}\right)^2 H^{cr-at}_{loc}(\vec{q}-\vec{p}'). \tag{A.6}$$

$F^{(2)}$ can also be simply calculated in the beginning of the calculation through Fourier transforms of $\langle V_{at,pr}(\vec{q})| \left(\frac{1}{\frac{1}{2}\vec{q}^2}\right)^2 |$.

The effective Hamiltonian H^{eff} can also be contracted onto the P-space. H^{eff} has the form

$$H^{eff} = -\left(H^{PQ}_{loc} + H^{PQ}_{nl}\right) \frac{1}{H^{QQ}_o} \left(H^{cr-at,QP}_{loc} + H^{cr-at,QP}_{nl}\right).$$

The nonlocal term on the left-hand side can be contracted onto $H^{cr-at,QP}$ in a similar fashion as was done to $\mathcal{O}$, giving two terms:

$$H_{nl,nl}(\vec{p},\vec{p}') = \sum_{\substack{\text{at,pr}\\ \text{at',pr'}}} |V_{at,pr}(\vec{p})\rangle f_{pr} A^{(1)}_{\substack{\text{at,pr}\\ \text{at',pr'}}} f_{pr'} \langle V_{at',pr'}(\vec{p}')|, \tag{A.7}$$

where

$$A^{(1)}_{\substack{\text{at,pr}\\ \text{at',pr'}}} = \sum_{\vec{q}} \langle V_{at,pr}(\vec{q})| \left(\frac{1}{\frac{1}{2}\vec{q}^2}\right) |V_{at',pr'}(\vec{q})\rangle, \tag{A.8}$$

and

$$H_{nl,loc}(\vec{p},\vec{p}') = \sum_{at,pr} |V_{at,pr}(\vec{p})\rangle f_{pr} \langle F^{(1)}_{at,pr}(\vec{p}')|, \tag{A.9}$$

where

$$\langle F^{(1)}_{at,pr}(\vec{p}')| = \langle V_{at,pr}(\vec{q})| \left(\frac{1}{\frac{1}{2}\vec{q}^2}\right) H^{cr-at}_{loc}(\vec{q}-\vec{p}'). \tag{A.10}$$

This will reduce almost all matrix multiplications onto the P-space. The only remaining Q-space multiplication would be in $H_{loc,nl}$ A final simplification that can be made is to take

$$H^{eff} = -H^{cr-at,PQ}\frac{1}{H_o^{QQ}}H^{cr-at,QP},$$

and thereby make the full effective Hamiltonian contractible onto the P-space.

Appendix B

Use of continuous symmetries to produce local moduli

This appendix outlines the use of rotational and translation symmetries of the force constant matrix to reformulate the ill-defined atomic moduli in Eq. (3.9) into the well-defined form in Eq. (3.11).

From continuous translational symmetry, all force-constant matrices obey

$$\sum_{\beta,\vec{R}} \Phi_{\alpha,\beta}(\vec{R}) \cdot \vec{c}_\beta \;=\; 0, \tag{B.1}$$

for any vector $\vec{c}_\beta = \vec{c}$ that is the constant vector for all atoms in the unit cell. Moreover, the $SO(3)$ rotational symmetries imply

$$\sum_{\beta,\vec{R}} \Phi_{\alpha q,\beta s}(\vec{R}) r_{\beta t} = \sum_{\beta,\vec{R}} \Phi_{\alpha q,\beta t}(\vec{R}) r_{\beta s}, \tag{B.2}$$

where the q, s, t correspond to one of the x, y, z Cartesian coordinates, $\Phi_{\alpha q,\beta s}(\vec{R})$ is the q, s component of $\Phi_{\alpha,\beta}(\vec{R})$ and $r_{\beta s}$ corresponds to the s component of the position vector $\vec{r}_\beta$.

The ill-defined atomic moduli, Eqs. (3.8)-(3.9), contain divergent terms which are in one of the following two forms:

$$\sum_{\alpha,\beta\vec{R}} \sigma_s r_{\alpha s} \Phi_{\alpha s,\beta t}(\vec{R}) u^{rl}_{\beta t}, \tag{B.3}$$

or

$$\sum_{\alpha,\beta\vec{R}} \sigma_s r_{\alpha s} \Phi_{\alpha s,\beta t}(\vec{R}) r_{\beta t} \sigma_t. \tag{B.4}$$

All of these terms scale linearly along the surface of the wire and give rise to the linear scaling of the surface moduli with system size evident in Figure 3-2a.

From Eq. (B.1), one can set Eq. (B.3) equal to

$$\sum_{\alpha,\beta\vec{R}} \sigma_s (r_{\alpha s} - r_{\beta s}) \Phi_{\alpha s,\beta t}(\vec{R}) u^{rl}_{\beta t}. \tag{B.5}$$

Using both Eqs. (B.1) and (B.2), one can set Eq. (B.4) equal to

$$\begin{aligned} -\sum_{\alpha,\beta\vec{R}} \quad \sigma_s \Big[& (r_{\alpha s} - r_{\beta s}) \Phi_{\alpha s,\beta t}(\vec{R}) (r_{\alpha t} - r_{\beta t}) \\ & -\tfrac{1}{4}(r_{\alpha s} - r_{\beta s}) \Phi_{\alpha t,\beta t}(\vec{R}) (r_{\alpha s} - r_{\beta s}) \\ & -\tfrac{1}{4}(r_{\alpha t} - r_{\beta t}) \Phi_{\alpha s,\beta s}(\vec{R}) (r_{\alpha t} - r_{\beta t}) \quad \Big] \sigma_t. \end{aligned} \tag{B.6}$$

The above terms now only depend on relative distances over a range controlled by the decay of the force-constant matrix and therefore no longer scale linearly with the size of the system. Combining the above transformations with the separation of the extensive motion from the intensive motion in the first-order polarization vector, Eq. (3.10), then results in the well defined form Eq. (3.11).

Appendix C

Failure of straightforward approches to predict flexion

It is now demonstrated that although the moduli defined in Eq. (3.9) indeed sum to give the correct overall extensional response, their unphysical scaling properties lead to invalid physical predictions when used in other contexts and, therefore, that they are ill-defined. In particular, simple scaling arguments are used to prove that these ill-defined moduli give a nonnegligible error in predicting the flexural rigidity in the continuum limit.

Consider a circular wire whose radius R is sufficiently large such that continuum theory applies. From Figure 3-2a it is seen that the surface moduli defined by Eq. (3.9) scale linearly with R. Because of this, and in order to arrive at an analytic result for the error in predicting the flexural rigidity, it can assume, to a good approximation, that all surface moduli e_s are proportional to their radial distance r from the center of the wire,

$$e_s = \bar{e}_s r.$$

Here, $\bar{e}_s$ is the same for all surface atoms. Next, R_i is defined as the inner radius such that all atoms at position $r < R_i$ are in the bulk and all atoms with positions $r > R_i$ are on the surface. Finally, $\Delta R \equiv R - R_i$.

Because of the facts that the surface moduli scale linearly with the system and that the sum of all atomic moduli must equal the extensional rigidity, the moduli in the bulk region of the wire, derived from Eq. (3.9), e_b' cannot equal the average value of the bulk material e_b. (Figure 3-2a also evidences this behavior.) The two above facts imply that the following equality must hold,

$$\int_{R_i}^{R} e_s r\, dr + \int_0^{R_i} e_b' r\, dr = \int_0^R e_b r\, dr,$$

or to leading order in ΔR,

$$\bar{e}_s \Delta R + e_b'/2 = e_b(1/2 + \Delta R/R_i). \tag{C.1}$$

In the continuum limit, the traditional continuum relation Eq. (3.15) holds, and therefore the fractional error in predicting the flexural rigidity from the ill-defined atomic moduli Eq. (3.9) is equal to

$$\delta F_{ill-at} = \frac{\int_0^{2\pi} d\theta \left(\int_{R_i}^{R} dr\, x^2 e_s r + \int_0^{R_i} dr\, x^2 e_b' r \right)}{\int_0^{2\pi} d\theta \int_0^R dr\, x^2 e_b r} - 1$$

or to leading order in ΔR,

$$\delta F_{ill-at} = \frac{\bar{e}_s \Delta R + e_b'/4 - e_b' \Delta R/R_i}{e_b/4} - 1. \tag{C.2}$$

Using Eq. (C.1) to solve for $\bar{e}_s \Delta R$, Eq. (C.2) becomes

$$\delta F_{ill-at} = 1 - \frac{e_b'}{e_b} + \frac{4(e_b - e_b')}{e_b} \Delta R/R.$$

Therefore, in the continuum limit, the ill-defined moduli do not approach the correct result and thus give a prediction which is even worse than that of traditional continuum theory.

Bibliography

[1] In D. Emin, T. Aselage, C.L. Beckel, I.A. Howard, and C. Wood, editors, *Boron-Rick Solids, AIP Conference Proceedings 140*, Albuquerque, New Mexico, 1986. American Institute of Physics.

[2] In H. Dreysse, editor, *Electronic Structure and Physical Properties of Solids, The Uses of the LMTO Method*, Lectures of a Workshop Held at Mont Saint Odile, France, October 2-5, 1998, 2000. Springer-Verlag.

[3] For a recent review see. *Rev. High Pressure Sci. Technol.*, 7, 1998.

[4] G.J. Ackland and R. Thetford. *Phil. Mag. A*, 56:15, 1987.

[5] I. Alber, J. L. Bassani, M. Khamtha, V. Vitek., and G. J. Wang. *Philisophical Transactions, Royal Society of London, A*, 399:555, 1992.

[6] T. A. Arias and J. D. Joannopoulos. *Physical Review Letters*, 69:3330, 1992.

[7] T.A. Arias. *Rev. Mod. Phys.*, 71:267, 1999.

[8] T.A. Arias and J.D. Joannopoulos. *Phys. Rev. Lett.*, 73:680, 1994.

[9] T.A. Arias, M.C. Payne, and J.D. Joannopoulos. *Phys. Rev. Lett.*, 69:1077, 1992.

[10] T.W. Barbee III and M.L. Cohen. *Phys. Rev. B*, 44:11563, 1991.

[11] L. Bellaiche and K. Kunc. *Phys. Rev. B*, 55:5006, 1997.

[12] J. R. K. Bigger and *et. al.* *Phys. Rev. Lett.*, 69:2224, 1992.

[13] P.E. Blochl. *Phys. Rev. B*, 50:17953, 1994.

[14] Max Born and Kun Huang. *Dynamical Theory of Crystal Lattices.* Oxford University Press, 1954.

[15] J. O. Broughton, C. A. Meli, P. Vashishta, and R. K. Kalia. *Physical Review B*, 56:611, 1997.

[16] V. V. Bulatov, O. Richmond, and M. V. Glasov. *Acta Materialia*, 47:3507, 1999.

[17] R. Car and M. Parrinello. *Phys. Rev. Lett.*, 55:2471, 1985.

[18] D. W. Carr and H. G. Craighead. *Journal of Vacuum Science and Technology B*, 15:2760, 1997.

[19] D.M. Ceperley and B.J. Alder. *Phys. Rev. Lett.*, 45:566, 1980.

[20] A. N. Cleland and M. L. Roukes. *Applied Physics Letters*, 69:2653, 1996.

[21] A.M. Cuitino, L. Stainier, and M. Ortiz. *J. Mech. Phys. Sol.*, 2002.

[22] A.M. Cuitino, L. Stainier, G. Wang, A. Strachan, T. Cagin, W.A. Goddard III, and M. Ortiz. *J. Comp-Aid Mat. Design*, (in press).

[23] J. Donohue. *The Strucutres of the Elements*, page 48. Wiley, New York, 1974.

[24] M.S. Duesbery. *Proc. R. Soc. Lond. A*, 54:145, 1984.

[25] M.S. Duesbery. *Dislocations 1984*, page 131, (CNRS, Paris, 1984).

[26] M.S. Duesbery and V. Vitek. *Acta Mater.*, 46:1481, 1998.

[27] M.I. Eremets, V.V. Struzhkin, H.-k. Mao, and R.J. Hemley. *Science*, 293:272, 2001.

[28] H. Feshbach. *Ann. Phys. N.Y.*, 19:287, 1962.

[29] M.W. Finnis and J.E. Sinclair. *Phil. Mag. A*, 50:45, 1984.

[30] F.E. Fortov and *et. al. JETP Lett.*, 70:628, 1999.

[31] S. Goedecker, M. Teter, and J. Hutter. *Phys. Rev. B*, 54:1703, 1996.

[32] I. Grinberg, N.J. Ramer, and A.M. Rappe. *Phys. Rev. B*, 63:201102(R), 2001.

[33] D.R. Hamann, M. Schluter, and C. Chiang. *Phys. Rev. Lett.*, 43:1494, 1979.

[34] M. Hanfland, K. Syassen, N.E. Christensen, and D.L. Novikov. *Nature*, 408:174, 2000.

[35] A. K. Head. *Phys. Stat. Sol.*, 6:461, 1964.

[36] E. Hernández, C. Goze, P. Bernier, and A. Rubio. *Physical Review Letters*, 80:4502, 1998.

[37] P.B Hirsch. Fifth int. conf. on cryst., 1960.

[38] J. P. Hirth and J. Lothe. *Theory of Dislocations.* John Wiley and Sons, 2 edition, 1982.

[39] W. G. Hoover. *Phys. Rev. A*, 31:1695, 1985.

[40] S. Ismail-Beigi and T.A. Arias. *Comput. Phys. Comm.*, 128:1, 2000.

[41] Sohrab Ismail-Beigi and T. A. Arias. *Phys. Rev. Lett.*, 82:2127, 1999.

[42] Sohrab Ismail-Beigi and T. A. Arias. *Phys. Rev. Lett.*, 84:1499, 2000.

[43] Sohrab Ismail-Beigi and Tomäs Arias. *Physical Review B*, 57:11923, 1998.

[44] K. Ito and V. Vitek. *Phil. Mag. A*, 81:1387, 2001.

[45] Ihm. J., A. Zunger, and M.L. Cohen. *J. Phys. C*, 12:4409, 1979.

[46] *et al* J. P. Salvetat. *Physical Review Letters*, 944:82, 1999.

[47] C. S. Jayanthi, M. Tang, S. Y. Wu, J. A. Cocks, and S. Yip. *Physical Review Letters*, 79:4601, 1997.

[48] B.G. Johnson, P.M.W. Gill, and J.A. Pople. *J. Chem. Phys.*, 98:5612, 1993.

[49] K. Kimura, S. Takeuchi, and K. Masuda-Jindo. *Phil. Mag. A*, 60:667, 1988.

[50] L. Kleinman and D.M. Bylander. *Phys. Rev. Lett.*, 48:1425, 1982.

[51] U.F. Kocks, A.S. Argon, and M.F. Ashby. Thermodynamics and kinetics of slip. In B. Chalmers, J.W. Christian, and T.B. Massalshi, editors, *Volume 19 of Progress in Materials Science*. Pergamon Press, 1975.

[52] M. Kohyama. *Journal of Physics: Condensed Matter*, 3:2193, 1994.

[53] N. Lehto and S. Oberg. *Phys. Rev. Lett.*, 80:5568, 1998.

[54] I. Lindgren and J. Morrison. *Atomic Many-Body Theory.* Springer-Verlag, Berlin, 1982.

[55] S.G. Louie, S. Froyen, and M.L. Cohen. *Phys. Rev. B*, 26:1738, 1982.

[56] P.-O. Lowdin. *J. Chem. Phys.*, 19:1396, 1951.

[57] Jian Ping Lu. *Physical Review Letters*, 79:1297, 1997.

[58] C. Mailhiot, J.B. Grant, and A.K. McMahan. *Phys. Rev. B*, 42:9033, 1990.

[59] A. G. Marinopoulos, V. Vitek, and J. L. Bassani. *Physica Status Solidi A*, 166:453, 1998.

[60] Ronald E. Miller and Vijay B. Shenoy. *Nanotechnology*, 11:139, 2000.

[61] T. E. Mitchell, R. A. Foxall, and P. B. Hirsch. *Phil. Mag.*, 8:1895, 1963.

[62] K. K. Mon. *Physical Review B*, 50:16718, 1994.

[63] K. K. Mon. *Journal of Applied Physics*, 80:2739, 1996.

[64] H.J. Monkhorst and J.D. Pack. *Phys. Rev. B*, 13:5188, 1976.

[65] J. A. Moriarty, W. Xu, P. Soderlind, J. Belak, L. H. Yang, and J. Zhu. *J. Engng. Mater. Technol.*, 121:120, 1999.

[66] V. Natoli, R.M. Martin, and D.M. Ceperley. *Phys. Rev. Lett.*, 70:1952, 1993.

[67] J.B. Neaton and N.W. Ashcroft. *Nature*, 400:141, 1999.

[68] J.B. Neaton and N.W. Ashcroft. *Phys. Rev. Lett.*, 86:2830, 2001.

[69] N. Osakabe, K. Harada, M. I. Lutwyche, H. Kasai, and A. Tonomura. *Applied Physics Letters*, 70:940, 1997.

[70] M. Parinello and A. Rahman. *J. Appl. Phys.*, 52:7182, 1981.

[71] M.C. Payne, M.P. Teter, D.C. Allen, T.A. Arias, and J.D. Joannopoulos. *Rev. Mod. Phys.*, 64:1045, 1992.

[72] J.P. Perdew and A. Zunger. *Phys. Rev. B*, 23:5048, 1981.

[73] Rob Phillips. *Crystals, Defects and Microstructures: Modeling Across Scales.* Cambridge University Press, 2001.

[74] W. Pickett. *Comput. Phys. Rep.*, 9:115, 1989.

[75] S. Rao, C. Hernandez, J. Simmons, T. Parthasarathy, and C. Woodward. *Philosophical Magazine A*, 77:231, 1998.

[76] S. Rao and C. Woodward. *Phil. Mag. A*, 81:1317, 2001.

[77] D. H. Robertson, D. W. Brenner, and J. W. Mintmire. *Physical Review B*, 45:12592, 1992.

[78] Marklund S. *Phys. Status Solidi B*, 85:673, 1978.

[79] S. Sawada. *Vacuum*, 41:612, 1990.

[80] E. Schmid. *Proc. Int. Congr. Appl. Mech. Delft*, page 342, 1942.

[81] D.S. Segall, T.A. Arias, A. Strachan, and W.A. Goddard III. *J. Comp-Aid Mat. Design*, (in press).

[82] V. J. Shenoy and R. Phillips. *Philosophical Magazine A*, 76:367, 1997.

[83] Y. Shibutani, V. Vitek, and J. L. Bassani. *Int. J. Mech. Sci.*, 40:129, 1998.

[84] W. Sigle. *Phil. Mag. A*, 79:1009, 1999.

[85] J.E. Sinclair. *J. Appl. Phys.*, 42:647, 1971.

[86] D.J. Singh. *Planewaves, Pseudopotentials and the LAPW Method.* Kluwer Academic, Norwell, MA., 1994.

[87] H. E. Stanley. *Rev. of Mod. Phys.*, 71S:358, 1999.

[88] F. A. Stillinger and T. A. Weber. *Physical Review B*, 31:5262, 1985.

[89] A. Strachan, T. Cagin, O. Gulseren, S. Mukherjee, R. E. Cohen, and W. A. Goddard III. *Phys. Rev. B*, (submitted).

[90] A. N. Stroh. *Phil. Mag.*, 3:625, 1958.

[91] V.V. Struzhkin, R.J. Hemley, and H.K. Mao. *Bull. Am. Phys. Soc.*, 44:1489, 1999.

[92] H. Suzuki. *Dislocation Dynamics*, page 679. New York: McGraw-Hill, 1968.

[93] S. Takeuchi. Core structure and glide behavior of a screw dislocation in the bcc lattice. In J. K. Lee, editor, *Interatomic Potentials and Crystalline Defects*, page 201, Warrendale, Pennsylvania: Metallurical Society of AIME, 1980.

[94] T. Tang, L. P. Kubin, and G. R. Canova. *Acta Mater.*, 46:3221, 1998.

[95] M. Teter. *Phys. Rev. B*, 48:5031, 1993.

[96] M.P. Teter, M.C. Payne, and D.C. Allan. *Phys. Rev. B*, 40:12255, 1989.

[97] M. M. J. Treacy, T. W. Ebbesen, and J. M. Gibson. *Nature*, 381:678, 1996.

[98] D. Vanderbilt. *Phys. Rev. B*, 41:7892, 1990.

[99] D. Vanderbilt and J.D. Joannopoulos. *Phys. Rev. B*, 27:6296, 1983.

[100] V. Vitek. *Cryst. Lattice Defects (and references therein)*, 5:1, 1974.

[101] Y.K. Vohra, K.E. Brister, S. Desgreniers, A. Ruoff, K.J. Chang, and M.L. Cohen. *Phys. Rev. Lett.*, 56:1944, 1986.

[102] G. Wang, A. Strachan, T. Cagin, and W.A. GoddardIII. *Mater. Sci. and Engng. A*, 309:133, 2001.

[103] J. Wang, T. A. Arias, and J. D. Joannopoulos. *Physical Review B*, 47:10497, 1993.

[104] W. Wasserbach. *Phil. Mag. A*, 53:335, 1986.

[105] E. W. Wong, P. E. Sheehan, and C. M. Lieber. *Science*, 277:1971, 1997.

[106] C. Woodward, S. Kajihara, and L.H. Yang. *Phys. Rev. B*, 57:13459, 1998.

[107] C. Woodward and S. Rao. *Phil. Mag. A*, 81:1305, 2001.

[108] C. Woodward and S. Rao. *Phys. Rev. Lett.*, 88:216402, 2002.

[109] R.W.G. Wyckoff. *Crystal Structures, 2nd ed., Vol I*, pages 22–23. Interscience Publishers, New York.

[110] W. Xu and J. A. Moriarty. *Phys. Rev. B*, 54:6941, 1996.

[111] W. Xu and J. A. Moriarty. *Computational Material Science*, 9:348, 1998.

[112] B. I. Yakobson, C. J. Brabec, and J. Bernholc. *Physical Review Letters*, 76:2511, 1996.

[113] L. H. Yang, P. Soderlind, and J. A. Moriarty. *Phil. Mag. A*, 81:1355, 2001.

[114] M.T. Yin and M.L. Cohen. *Phys. Rev. B*, 26:3259, 1982.